UCLouvain

École polytechnique de Louvain

Design of a harmonic radar for Asian hornet tracking

Author: **Hugo Damme**
Supervisor: **Dimitri Lederer**
Readers: **Jérome Louveaux, Théo Denis, David Bol**
Academic year 2025–2026
Master [120] in Electrical Engineering

Acknowledgements

I would like to express my gratitude to Professor Lederer for its support, understanding and kindness that were invaluable during this whole thesis.

I am thankful to Professor Craeye for its expertise in antennas. I would also like to recognize Pascal Simon who assisted me with the vector network analyzer, the signal generator and the signal analyzer.

Finally, A special thanks to Fréderic Druppel who provided the prototype of harmonic tag and to Laetitia Niyonzima who provided the simulation files of the Hat antenna.

Contents

Chapter 1

Introduction

1.1 Context

The presence of the yellow-legged Asian hornet (Vespa velutina nigrithorax) in Europe was first reported in 2004 in the south of France. Since then, it has spread throughout multiple European countries, namely Belgium, Spain, Portugal, Italy and Germany [25].

An invasive alien specie (IAS) can have dramatic consequences on human communities and on the invaded region ecosystem. As an example, the Asian hornet invasion has an impact on well-being (risk of stings, fear, etc.), honey related industries and pollination dependent industries.

Multiple studies have estimated the yearly cost of these impact using models. The global cost was estimated at: 2.8M€ for the honey industry[27] (in the best case), 12M€ in control and surveillance (in France)[2] and 10M€ due to the reduction in pollination[8] (in Spain, Italy and Portugal).

Additionally, researcher have predicted the evolution of the suitability for the Asian hornet of the Europe due to climate change. They show that the European climate will become even more suitable for the Asian hornet [3, 9]. This outlines that the Asian will not stay contained in the already conquered territories (West Europe) and should propagate throughout Europe.

The vespa velutina nigrithorax has been added to the list of invasive alien species (IAS) in 2016 (EU Reg. 1141/2016). Since then, EU members must adopt surveillance plan and control strategies for the Asian hornet according to the regulation on IAS (EU Reg. 1143/2014).

One example of surveillance network is the notification system (NOTSYS) of the European Alien Species Information Network (EASIN) When an IAS is spotted, one can send an notification to the information network to repertoriate the spread of the species. This system is illustrated for the vespa velutina nigrithorax during the year 2024 in 1.1.

There exist multiple ways of controlling the Asian hornet. This includes traps, baits and nest destruction. In this work, we will focus on nest destruction.

One can search for hornet nest using different methods. It can be as simple as visually looking for nest. Unfortunately, this method is also very inefficient as hornet nest are usually hidden behind foliage or walls. Furthermore, Asian hornets foraging range can be of several kilometers. The search radius is then very large.

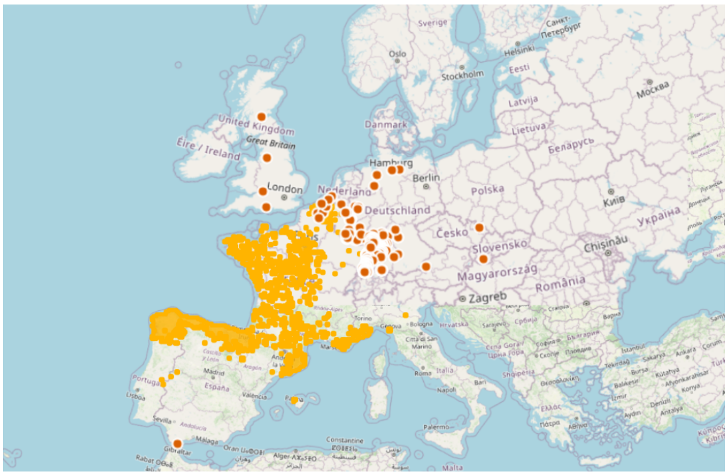

Figure 1.1: Map representing the spread of the vespa velutina nigrithorax in Europa in 2024. Yellow dots represent reference data and red dots represent sighting alerts passed through NOTSYS in 2024[7].

The idea of Asian hornet tracking aims to reduce the search area by following the hornet directly to its nest thanks to its homing instinct. The method used to achieve tracking of small insects are: visual tags, radio-telemetry or using an harmonic RADAR.

We will focus on the harmonic RADAR technology for its low tag cost and tag weight and the possibility to continue tracking even if the target goes behind a thin layer of leaves. Its main downside is its low range. An harmonic RADAR is similar to a classical RADAR in that it obtain inversion about the target using a signal that was reflected on it. The difference is that a tag is placed on the target to modify the frequency of the signal. The harmonic RADAR then receive a signal that is an harmonic of the emitted signal (usually the second). The received signal can then be easily separated from the emitted signal and its reflection on non-target object (using an high pass filter). This harmonic conversion is usually performed using a non-linear device such has a diode as seen in figure 1.2. Unfortunately, we also see that the power at the second harmonics is low as the total power is spread into many harmonic components which create an additional signal attenuation. This attenuation lead to a smaller detection range.

Currently, hornet tracking is done using a static RADAR or handheld antenna (e.g. [19]). In the case of an harmonic RADAR, these techniques suffers greatly from the limited range. Therefore, we consider the use of an harmonic RADAR mounted on a UAV to be able to follow the target and keep it inside the range. This allows to perform the tracking even if the RADAR range is small.

In this work, we aim at designing a first harmonic RADAR prototype (similar to [19, 31]) to explore the use of UAV for hornet tracking. It must have a low weight such that it can be carried by lower class drones to have more freedom with respect to the legislation. The range might be low but should still allow for basic tests (e.g. flying around a static target while detecting its position). We also develop the equations of the system for future use.

We first compare the harmonic RADAR technology with other tracking technologies to better situate this technology. We also how certain technology can be used conjointly

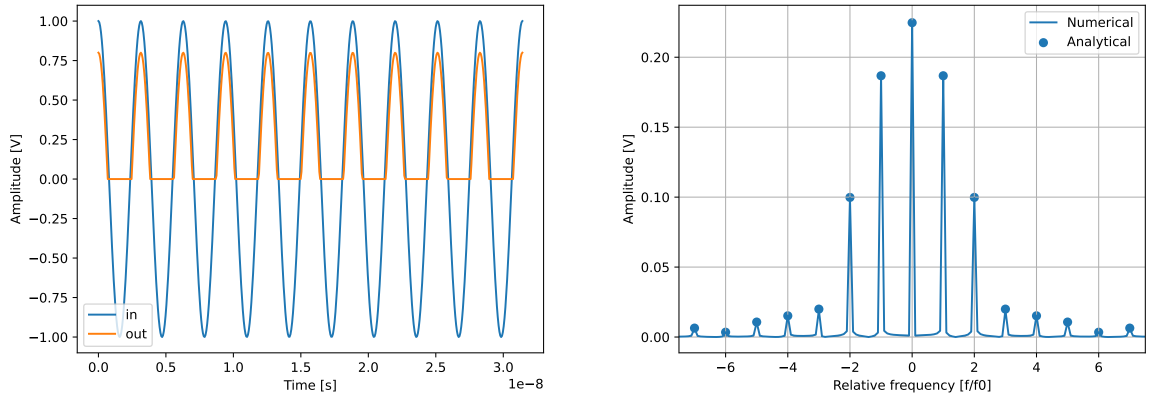

(a) Sinusoidal signal of unit amplitude cropped by a diode with a forward voltage of 0.3

(b) Amplitude of the output signal in the frequency domain

Figure 1.2

with an harmonic RADAR.

Secondly, we discuss about the practical aspect of the application. We explicit the tracking strategy, present some limiting characteristics of Asian hornet and regulations. We also choose how the drone is positioned with the target during tracking as it has consequences on the system design.

Thirdly, we write the link budget and obtain the theoretical range of the system. The FMCW RADAR equations are also developed. From them, we obtain the parameters estimator and a value for the minimum SNR required at the receiver to use in the link budget.

Then, the different parts of the system (RF circuits and antenna) are designed and prototypes are built.

Finally, the prototype main characteristics are measured to determine its performance and maximum range. Additionally, non-idealities are presented and their effects on the system are discussed.

Chapter 2

Comparison with other embedded alternatives

There are many possible ways to prevent the invasion of the yellow-legged Asian hornet and stop its damage. They range from defensive approach such as protecting the hives with nets to offensive approach such as tracking and destroying the nests. These diverse solutions were explored and compared in a previous work [35].

In this work, we will limit ourselves on tracking systems that can and have been mounted on UAVs. There are a lot of devices and systems that can potentially help find and detect the nest of Asian hornets. The most intuitive and direct one is visual tracking as UAVs are often equipped with a camera to allow out-of-sight driving of the drone. More complex techniques consist of tagging the hornet with a active or passive emitter and tracking it using dedicated equipment.

These additional equipment can be considered as payloads and impact the flight capabilities of the UAV. Some constraints and limitations of these equipment can therefore be listed:

- **Low weight**: The total weight of the equipment must be lower than the maximum payload weight of the drone. Additionally, the flight duration is directly proportional to the total weight of the UAV. Furthermore, the higher the weight, the higher the exerted downward trust. We can then assume that the minimum distance between the UAV and the target to prevent the flight behavior to be perturbed is increased. The weight of the embedded equipment must thus be minimized.

- **Limited power consumption**: similarly, the more power is consumed by the payload, the shorter is the maximum flight duration.

- **Limited footprint and good balance**[1]: bulky payloads and imbalances can greatly reduce the maneuverability of the UAV. This maneuverability is important in a context of tracking a fast moving hornet.

Examples of devices that meet these constraints are low-range radars, radio-telemetry, optical equipment, infrared cameras, etc.. In the following sections, we will presents these in more details and compare them with the harmonic radar.

[1]Counterweights can be added but must be taken into account to not exceed the weight limit

2.1 Optical and camera tracking

For a long time, insects were tracked visually with binocular and eyes only. With the advance of technology and, more precisely, cameras, new possibilities are unlocked beyond the limited field of view (FOV) of a human.

The integration of such a technique with UAV is very easy as professional UAV always have an embedded camera as a mean of piloting the drone even when it is beyond line of sight (not that direct line of sight must be maintained for drone in the open category see section 3.1.3). There are thus, a priori, no additional cost for this technique and many commercial products are available. The cost is minimized for a very simple optical tracking.

Unfortunately, in our application, the target is of very small size. As real time tracking with a UAV require a large FOV to avoid obstacles, an hornet can hardly be distinguished from the background on the screen. In the litterature, researchers have successfully tracked and identified multiple untagged bees species and hornets in a controlled and static environment[10]. The aim of such research was to detect the presence of hornets in the proximity of an apiary.

Furthermore, in our application, the background is always changing and unpredictable, which could greatly reduce the effectiveness of such a tracking method.

This led people to make the hornets more visible using piece of paper or retro-reflective tags[30]. A more advanced optical tracking techniques uses luminescent tags emitting a wavelength that is filtered by the atmosphere (i.e. a low amount of signals at this frequency are present in the background) and tracks it using an additional camera equipped with a filter that rejects all other frequencies[32].

The downside of this is that physical obstacle and background parasitic reflections can lead to a target loss. Furthermore, if the pilot is distracted for a split second, it could easily lose the target if it is not clearly displayed on the visual interface.

Using identification techniques, we could track the target even when it is not very visible on the screen. This would require running code or AI models to monitor the visual feed and highlight the target and therefore add a delay in the detection chain. As we are in a real-time application, this delay could be dramatic if too long.

2.2 Traditional RADARs

A RAdio Detection And Ranging system is a device that emits a pulse or wave at radiofrequency to extract some characteristic about a target. This principle is illustrated in figure 2.1.

The extracted characteristic are usually the speed, the range and the direction of the target. First, the Doppler effect is used to extract the speed of the target from the change in frequency undergone by the signal. Secondly, the range is estimated quite differently depending on the type of RADAR. They can be divided in two main categories[2]: the pulsed or Continuous Wave (CW). A pulsed RADAR uses the delay the emitted and

[2]At this level, the harmonic RADAR is not a category of RADAR. Indeed, harmonic refers to the difference in emitted and receive frequency. A harmonic radar can use either the pulsed or CW method.

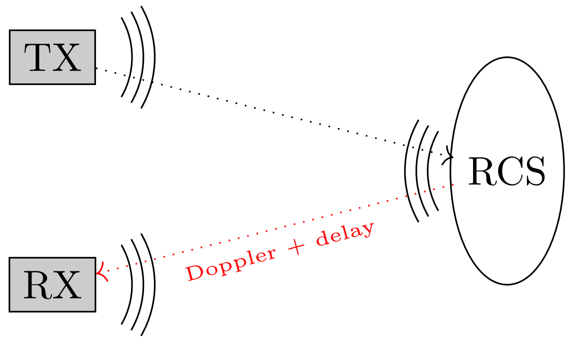

Figure 2.1: Basic operating principle of a radar

received pulse to determine the distance. A CW RADAR uses modulation techniques and difference in emitted and received wave to determine the distance.

Finally, some RADAR also estimates the angles of the direction. This is done by varying the direction of the main lobe of the antenna and taking the angle of the maximum received signal. It can be implemented in 1D or 2D (azimuthal and/or elevation) depending on the need of the application.

These devices have various limitations due to their operating principle. Indeed, all elements in the field of view of the RADAR can potentially reflect the signal. The power reflected by the target must then be compared to the one reflected by the background. This power depends on multiple characteristic of the target such as physical area, material, angle etc..

We can take a look at a figure of merit that summarize all these properties, the RADAR cross section (RCS). It is defined as the equivalent cross section area of a perfectly reflecting sphere that would produce the same signal strength at the radar.

In the case of insect tracking, the target is of very small dimensions. We can assume that it has a very low RCS even more so compared to large buildings and metallic objects. This means that the incident power and reflected by the target is quite small. The system must then be very sensitive to allow the signal to be detected from a long range.

Many processing techniques allows to remove the background impact on the signal (e.g. Moving Target Identification). However, as the background generate a very large signal, it can overload the very sensitive receiver.

This makes it impossible to use RADAR for small insects tracking.

2.3 Thermal camera

The nest of some species of hornets is maintained at a constant temperature between 28° and 30°C[18]. We can thus assume a temperature difference with its environment.

People have studied the viability of thermal imaging in the search of Asian hornet nest[18]. They took picture of vespa velutina nigrithorax at multiple distance, angle and hour of the day. Then they estimated the visibility of the nest.

They observed that the time of the day where the nest are more visible before sunrise or in the evening. Furthermore, the presence of a tree canopy greatly reduce the detectability

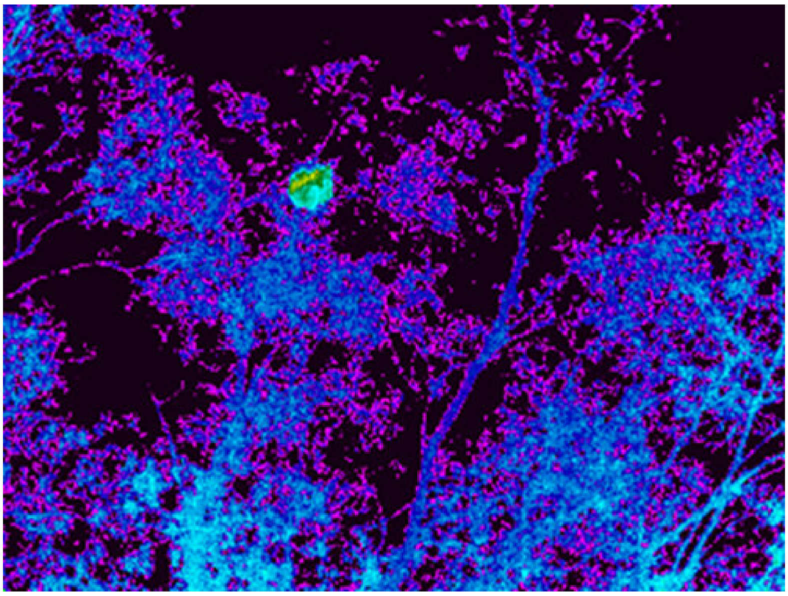

Figure 2.2: Image of an hornet nest taken with an thermal camera[18]. It is localized high in a tree and behind the canopy but is still clearly visible.

of the nests. However, when no dense obstacle are in front of the nest, some were visible up to 30m.

Due to their small size and weight, this type of camera can easily be mounted on an UAV. This could potentially help in finding nest located high up in the trees (10m to 30m high). This could allow to overfly trees and vegetation to detect nest that are hidden behind tree canopies and are hidden from optical cameras. The effectiveness of this solution greatly depends on the location of the nest. Indeed, if the nest is hidden deep in the tree canopy, it will become hardly visible. In this case, thermal camera are better used from the ground.

The drawback of this method is that the search has to be done in the whole area of interest (i.e. a circle around the apiary of radius equal to the foraging range of the Asian hornet). As the foraging range of the yellow-legged Asian hornet can be of several kilometers (up to 2.3 km)[17], the search area can be very large.

Therefore, this technique is best suited to pinpoint the exact location of the nest when the area of interest has been reduced and shoud be used in conjonction with other tracking techniques.

2.4 Radio telemetry

Radio telemetry is a technique using small radio transmitter tag attached to the target. The tag will then emit a signal which will be localized using RSSI (received signal strength indication). The localization consist of finding the direction of maximum received signal strength and deducting the distance to the target using a path loss approximation.

Radio-telemetry has been widely used to track a large variety of animals. It is a very mature technology that has proven its effectiveness in wildlife tracking.

This technique has a lot of advantages. The initial investment (cost of the receiver and embedded equipment) is relatively low. The range of detection is also very large (in kilometers). Additionally, multiple targets can be uniquely differentiated using an identification code emitted by each tag.

However, due to the active nature of the tag, its weight is dramatically increased as it must carry a battery. Furthermore, each tag has a limited lifespan and a short shelf life while being costly and usually single-use. This lead to a large cost over time compared to the other techniques despite the low initial cost [33].

Researchers are developing more lightweight (30mg) radio-telemetry tags by using smaller battery and energy harvesting techniques[33]. This outlines the possible application of radio telemetry for small insects and could still be improved to compensate its shortcoming.

This technology has already been commercialized in the context of Asian hornet tracking.

One such example is LOCNEST by Intuite [11]. This project offers radio-telemetry tag to track Asian hornets using hand-held antennas. The system specifications are: a range of 3 to 4 km, a tag autonomy of 3h, tag weight of 0.12 g.

Figure 2.3: LOCNEST radio-telemetry tag glued to the back of an Asian hornet. The weight of the tag is 0.12 mg and its autonomy is 3h.

This system is composed of a transmitter kit and a receiver kit. The receiver kit contains a tag (55€) and a rechargeable battery (8€). The transmitter kit (262€) contains the antenna and the SDR kit.

We see that the price of the tag is quite significant (one fifth of the receiver kit). Even though it is reusable, in the case of an unsuccessful retrieval, this cost must be paid again which can lead to non-negligible expense.

Still, this solution seems to be accessible for people, such as beekeeper or farmers, that wants to get read of Asian hornets in the vicinity of their workplace.

2.5 Summary

Many different technologies can be used to tracks small insects such as Asian hornets. They all have their strength and inconvenient and could be used conjointly to increase the success rate of nest finding (e.g. Thermal imagery can be used to pinpoint the nest once a small area is delimited by radio telemetry).

The current technologies used for tracking Asian hornet include harmonic radar (e.g. Life STOPVESPA project in Italy) or radio-telemetry (LOCNEST in France). In these two examples, the tracking is done from the ground using a static RADAR or a handheld antenna.

In this work, we will explore the possibility of using these technology in an embedded system on a unmanned aerial vehicle (UAV). We focus on the harmonic RADAR technology as an UAV can compensate for its biggest weakness: its small range.

Chapter 3

Tracking context and global design choice

In this section, we will discuss about the context of Asian hornet tracking to better understand what are the requirement of the system. We will first talk about the basic tracking strategy and some information about the practical tracking of hornets. Then, we will

3.1 Overview

In this section, we will explain the basic of the methodology and what we have to take into account when tracking the yellow-legged Asian hornet. This is important to justify design choices and predict limitations. see the different global position the drone can take and deduce how the system must be designed for a chosen position.

3.1.1 Basic idea of strategy

The basic idea of the methodology is as following. A bait station is placed near the place were the sighting of the Asian hornet was reported. A hornet is captured and tagged. It is then released so that it can hopefully go back to its nest. Finally, an UAV equipped with the harmonic radar follows the hornet up to its nest.

Special care has to be taken for situation where the last part (UAV tracking) was interrupted due to having lost the target. This can correspond to multiple situations: The target has left the range of detection of the radar; The target got behind an obstacle that prevent its detection; The nest was reached but is hidden behind a wall, foliage or underground.

In this cases, we have multiple options to resume the tracking. First, the pilot can decide to begin a global search in the vicinity of the last known position of the target and try to find it back supposing that it did not left the operational range of the RADAR. Secondly, if the nest was supposedly reached, a thorough visual search can be done at the cost of completely losing the target. The last resort is to begin the whole tracking again either by tagging a new hornet or by setting up a new bait station near the end of the track.

This idea should be refined by experiments to take into account practical aspects of the tracking. More complex ideas could also be explored such as tagging multiple hornets for resilience. In this case, it may be necessary to distinguish between hornets which is not inherent for harmonic radars (as opposed with radio telemetry). Processing techniques such as Kalmann filters can also help with target differentiation even if tag signals are not distinguishable between one another.

Nevertheless, it gives an idea of the basic requirements needed to fulfill an Asian hornet tracking.

3.1.2 Yellow-legged Asian hornet flight characteristics

In this subsection, we will gives some numerical characteristics of the flight of the Asian hornet. It is important to have data about the target to be able to track it efficiently.

One very important characteristic is the maximum payload a hornet can carry without impeding its flight capability.

In [15], they determined the maximum payload by successively increasing the payload weight from 0mg to 350 mg They found found that above 250 mg, the majority of hornets could not fly properly.

This characteristic directly impact the system. For an harmonic radar, it inherently limit the minimum carrier frequency. Indeed, the weight of the tag can be assumed to be linear to its length which depends directly on the frequency.

Other important characteristics include the speed, flight duration, flight distance, etc. These directly impact the choice of drone and must therefore be explicited. These are summarized in table 3.1.

Other flight characteristics that are of interest are, for example, the total and average resting time. Unfortunately, we did not find any data about these in the literature.

Flight speed (nest to apiary)	**Flight speed** (apiary to nest)	**Foraging range**
$6.66 \pm 2.31[\frac{m}{s}]$	$4.06 \pm 1.34[\frac{m}{s}]$	$395 \pm 208[m]$

Table 3.1: Different flight characteristic of the yellow-legged Asian hornet obtained through tracking in [17]

3.1.3 Tracking environment and regulations

Another important aspect to take into account while tracking using an aerial vehicle is the environment of the search area. It concerns all the obstacles and topology as well as all the regulations in place.

The terrain, wherein the search area can be, is very diverse in nature. Indeed, the nest of v. velutina nigrithorax can be located in urban as well as rural areas depending on its development state[15]. The consequence is that the system must be adapted for all these terrain.

In a rural area, the UAV must navigate between trees and vegetation. The tag signal could also be attenuated by foliage.

In an urban area, reflections caused by metallic object could be mistaken as target. For an ideal harmonic radar, these reflections of fundamental signal are discarded by the receiving chain. However, in a real circuit, as some amount of signal at the harmonic frequency can still be emitted by the transmitter, it could impact the system. Another problem with urban area is the proximity with people. Indeed, depending on the class of drone, a minimal horizontal distance from people must be maintained

We will now take a quick look at the law and regulation about UAV in operation. The most basic limitation is that flying over restricted or private area is forbidden.

For the more specific rules, drones are divided in multiple categories by the European union Aviation Safety Agency (EASA): open, specific and certified. In this work, we will only take a look at the open category where the operations classified as low risk fall in. The open category has multiple basic rules. First, direct line of sight with the UAV must be maintained during the complete duration of the operation. Secondly, the distance from the ground of the drone may not exceed 120 m at any point of the operation. Thirdly, the UAV can not be flown above a large group of people. It must also not carry dangerous goods nor drop it during operation. The main advantage of this category is no authorization are required before operation nor declaration from the UAV operator.

This category is further divided in 3 subcategory: A1,A2,A3. The main discriminator between these subcategory is the takeoff weight of the drone. The A1 subcategory has a takeoff weight limit of 500g. The limit for the A2 and A3 subcategory are 4 kg and 25 kg respectively.

The main differences between these subcategory is the minimum horizontal distance with people (30m for A2 and 1:1 rule with height for A3) and the need for a pilot registration (required for A2 and A3).

If these restriction are too limiting (e.g the line of sight requirement) the system operation, we must look into a higher category such as the specific category.

3.2 Drone position

In this section we will compare two drone position with respect with the target during tracking: above the target and behind the target. We will see that these two possibilities are quite different from a system point of view.

3.2.1 Above the target

This configuration is typically used in avalanche rescue missions. This application is characterized by non-moving target buried into meters of snow. The "from above" configuration allows to quickly scan a large area while minimizing the slope gradient impact and allowing the RF wave to deeply penetrate the snow using a low frequency signal.

In this case, the radar primarily serves as a presence detection equipment. It is used to know if there is someone (or more precisely a tag) trapped under the snow. It could also measure the distance between the radar and the target to estimates under how many meters of snow it is buried.

We will now study more precisely the characteristics of this configuration in the context of our application.

As said before, typical RADAR usually measure distance and speed. However, in this case, these are not of interest for our application. Indeed, an efficient tracking require to know or estimate the direction and movement of the target. Here we want to track the movement with respect to the ground.

Unfortunately, as shown on figure 3.1, the distance and speed are measured radially from the RADAR. In this configuration, this means that these are mostly vertical. Their usefulness is then greatly reduced. Therefore, the tracking must be based on other quantities. To obtain the values of interest, i.e. the cartesian coordinates, we can first estimates the radius and the 2 angles of the spherical system. We would thus need 2D angle determination as well as the range measurement. We then obtain the spherical coordinates of the target and can deduce the cartesian coordinates.

Another limitation is that the drone must fly at a sufficient height from the target. As seen in the section hereinabove, the maximum height of the UAV from the ground is 120m. It must then be taken into account when designing the system in this position.

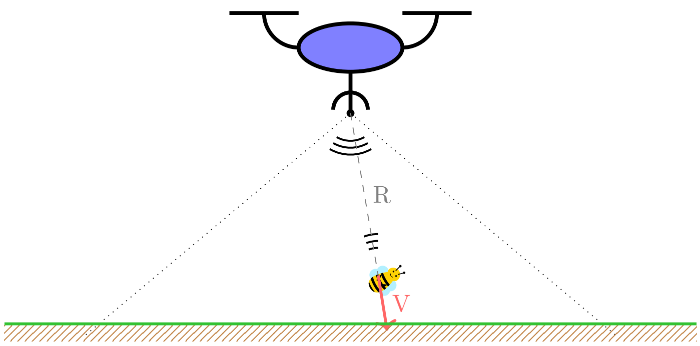

Figure 3.1: Diagram presenting the tracking from above. R is the distance between the RADAR and the target and V is the radial speed of the target (referencing to the RADAR)

3.2.2 Behind the target

The other drone position is behind the target. In this configuration, the radial distance and speed are mostly horizontal with respect to the ground (see figure 3.2). They are then directly usable for tracking.

Furthermore, the angle tracking is quite straightforward. Indeed a simple 1D scanning is sufficient to be able to follow the target. Additionally, with the high mobility of the drone, one can imagine a system where the drone simply rotate around the vertical axis to steer the direction of the main lobe of the RADAR.

Nevertheless, slope of the terrain can hinder the RADAR operation. Indeed, if the width of the main lobe is insufficient in the elevation plane, the target can quickly leave the RADAR detection range by gaining altitude.

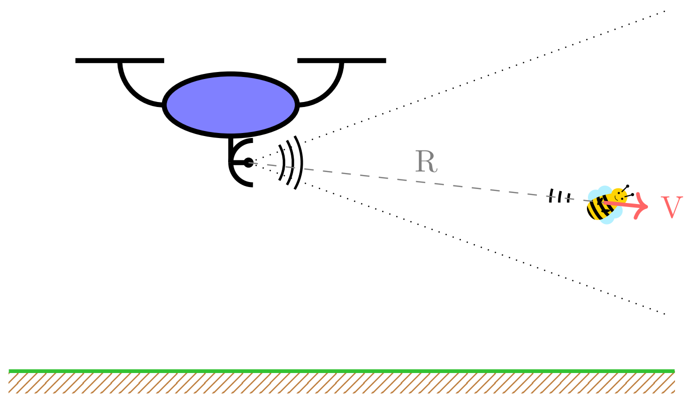

Figure 3.2: Diagram presenting the tracking from behind. R is the distance between the RADAR and the target and V is the radial speed of the target (referencing to the RADAR)

3.3 Conclusion

In this chapter, we have talked about the multiple limitations and requirement of the system. These includes the limit on tag weight (<0.25 g), the diversity of operation environment (rural and urban), the applicable law for UAV and the drone position.

In this work, we will select the "From behind" configuration due to the simple angle tracking and limited height from the ground. Therefore, the tag and antenna will have a vertical operation such that the polarization factor is independent from the direction of flight of the target.

Furthermore, we will assume that the RADAR and the target stays in the same horizontal plane during tracking for the design of the antenna. The only plane of interest is then the azimuthal plane.

Chapter 4

Theoretical development of the harmonic RADAR and link budget equations

4.1 Link budget and maximum range

In this section, we will develop an expression for the link budget of the RADAR. From this, we will express the theoretical maximum range of the system depending on design parameter.

4.1.1 Link budget

As a remainder, the RADAR sends a signal at the fundamental frequency. It is then received by the tag that will double its frequency and reemit the signal. We can modelize this system using two path losses and a conversion efficiency.

In the following subsection, we will use the following naming convention: With X being TX or RX, a quantity A_X refers to the RADAR side and, similarly, a quantity $\bar{A}_X$ refers to the tag side. λ_f,λ_h refers to the wavelength at the fundamental and harmonic frequency and d is the distance to the target.

Using Friis transmission equation, we obtain the expression of the two received power:

$$\begin{cases} \bar{P}_{RX} = P_{TX} G_{TX} \bar{G}_{RX} \left(\dfrac{\lambda_f}{4\pi d} \right)^2 \\ P_{RX} = \bar{P}_{TX} \bar{G}_{TX} G_{RX} \left(\dfrac{\lambda_h}{4\pi d} \right)^2 \end{cases} \tag{4.1}$$

To obtain the dependance of the received power P_{RX} on the emitted power P_{TX} and the target distance, we need to get an expression for the power reemitted by the tag.

We can suppose that this power entirely depends on the power received by the tag. Using a Taylor series expansion, we can write:

$$\bar{P}_{TX}(\bar{P}_{RX}) = \sum_{n=0}^{+\infty} a_n \frac{\bar{P}_{RX}^n}{n!} = a_0 + a_1 \bar{P}_{RX} + a_2 \frac{\bar{P}_{RX}^2}{2} + \cdots \tag{4.2}$$

The tag is a passive device. Therefore, when no power is received by the tag, no power is reemitted (i.e. $\bar{P}_{TX}(\bar{P}_{RX} = 0) = 0$). This lead to $a_0 = 0$. We can write:

$$\bar{P}_{TX}(\bar{P}_{RX}) = (a_1 + a_2\frac{\bar{P}_{RX}}{2} + \cdots)\bar{P}_{RX} = (\sum_{n=1}^{+\infty} a_n \frac{\bar{P}_{RX}^{n-1}}{n!})\bar{P}_{RX} \tag{4.3}$$

$$= \eta'(\bar{P}_{RX})\bar{P}_{RX} \tag{4.4}$$

By combining equations 4.1 and 4.4, we obtain:

$$P_{RX} = P_{TX}\, G_{TX}G_{RX}\, \bar{G}_{TX}\bar{G}_{RX}\eta'(\bar{P}_{RX}) \left(\frac{\lambda_f \lambda_h}{(4\pi d)^2}\right)^2 \tag{4.5}$$

Using the fact that $\lambda_f = 2\lambda_h$ and by defining:

$$\begin{cases} G = G_{TX}G_{RX} \\ \eta(\bar{P}_{RX}) = \bar{G}_{TX}\bar{G}_{RX}\eta'(\bar{P}_{RX}) \end{cases} \tag{4.6}$$

We can rewrite eq. 4.5 as:

$$P_{RX} = P_{TX}\, G\, \eta(\bar{P}_{RX})\frac{\lambda_h^4}{64(\pi d)^4} \tag{4.7}$$

This expression does not take the mismatch of the system into account. Nevertheless, in this application, we can have impedance mismatch as well as polarization mismatch. This can be easily admitted as the polarization of the tag depends on its relative position and its impedance matching depends on the incident power level[1].

We can rewrite the transmission equations (eq. 4.1) as:

$$\begin{cases} \bar{P}_{RX} = P_{TX}G_{TX}\bar{G}_{RX}\left(\frac{\lambda_f}{4\pi d}\right)^2 (1 - |\Gamma_{TX}|^2)(1 - |\bar{\Gamma}_{RX}|^2)|\hat{e}_{TX} \cdot \bar{\hat{e}}_{RX}|^2 \\ P_{RX} = \bar{P}_{TX}\bar{G}_{TX}G_{RX}\left(\frac{\lambda_h}{4\pi d}\right)^2 (1 - |\Gamma_{RX}|^2)(1 - |\bar{\Gamma}_{TX}|^2)|\bar{\hat{e}}_{TX} \cdot \hat{e}_{RX}|^2 \end{cases} \tag{4.8}$$

We can easily suppose $\hat{e}_{TX} = \hat{e}_{RX} = \hat{e}$ and $\bar{\hat{e}}_{TX} = \bar{\hat{e}}_{RX} = \bar{\hat{e}}$. Furthermore, we can assimilate the impedance mismatch of each antenna and its gain. We name $G'_X = G_X(1 - |\Gamma_X|^2)$ the realized gain of the antenna. We obtain:

$$\begin{cases} G = G_{TX}(1 - |\Gamma_{TX}|^2)G_{RX}(1 - |\Gamma_{RX}|^2) = G'_{TX}G'_{RX} \\ \eta(\bar{P}_{RX}) = \bar{G}'_{TX}\bar{G}'_{RX}\eta'(\bar{P}_{RX}) \end{cases} \tag{4.9}$$

We obtain the final expressions that will be used in the rest of this work:

$$\begin{cases} P_{RX} = P_{TX}\, G\, \eta(\bar{P}_{RX}) \left(\frac{\lambda_h}{2\sqrt{2}\pi d}\right)^4 |\hat{e} \cdot \bar{\hat{e}}|^4 \\ \bar{P}_{RX} = P_{TX}G'_{TX}\bar{G}'_{RX}\left(\frac{\lambda_f}{4\pi d}\right)^2 |\hat{e} \cdot \bar{\hat{e}}|^2 \end{cases} \tag{4.10}$$

[1] In all generality, the input impedance of a diode depends on the large signal amplitude applied on its port and therefore the applied signal power

4.1.2 Polarization factor

In this section, we will aim at estimating the polarization factor. This is important as it depends on the orientation of the target and the different antennas composing the system. We will define a referential for both the RADAR and the target. The third component of these referential coincide with the direction of the linear antenna attached to the UAV or hornet. These two referential are obtained by rotations of the inertial referential.

First, the target and UAV rotates around the vertical (3rd) axis. Then, due to the movements of both the hornet and UAV, both antenna tilt forward and backward accordingly to the flight direction. Lastly, due to similar reason, the antennas can have a left and right tilt. The last two rotation can also be due to tilt present from a slight misplacement of the tag on the hornet or of the antennas on the UAV. Mathematically, we get:

$$\begin{cases} \hat{e} = \hat{x}_3 \\ \bar{\hat{e}} = \hat{y}_3 \end{cases} \qquad \text{with} \begin{cases} [X] = R_{\psi}^{(3)} R_{\theta}^{(1)} R_{\phi}^{(2)} \, [I] \\ [Y] = R_{\gamma}^{(3)} R_{\beta}^{(1)} R_{\alpha}^{(2)} \, [I] \end{cases} \tag{4.11}$$

As a first order, we can suppose that the antennas of both the tag and RADAR are placed perfectly vertically during the whole tracking. We consider all the flight orientation of the target (Rotation around the third axis). This is equivalent to setting all the rotation angles except α to zero. We obtain:

$$\hat{e} = \bar{\hat{e}} = I_3 \Rightarrow |\hat{e} \cdot \bar{\hat{e}}| = 1 \tag{4.12}$$

In this case, the polarization factor is always unitary which outline the advantage of the vertical polarization

Unfortunately, in practice, the two antennas are never perfectly vertical. As explained before, the placement precision as well as the hornet thorax movement can change the orientation of the tag antenna.

Similarly, the drone can also tilt frontally and laterally depending on its movement and the designer can choose to place the antenna at an angle to orient the direction of the maximum. The general expression is given when all angles are non-zero. To lighten the expression, we will abbreviate the sinus and cosine function as "s" and "c" respectively

$$\begin{cases} \hat{e} = (s\phi s\theta c\psi - c\phi s\psi) I_1 - (s\phi s\psi + c\phi s\theta c\psi) I_2 + c\theta c\psi I_3 \\ \bar{\hat{e}} = (s\alpha s\beta c\gamma - c\alpha s\gamma) I_1 - (s\alpha s\gamma + c\alpha s\beta c\gamma) I_2 + c\beta c\gamma I_3 \end{cases} \tag{4.13}$$

$$\Rightarrow |\hat{e} \cdot \bar{\hat{e}}| = c(\phi - \alpha)(s\psi s\gamma + s\theta s\beta c\psi c\gamma) + s(\phi - \alpha)(s\beta s\psi c\gamma - s\theta c\psi s\gamma) + c\theta c\beta c\psi c\gamma \tag{4.14}$$

We see that the effect of the orientation of flight is relative between the two objects (i.e. the expression is only dependent on $\phi - \alpha$). Therefore, we can take the orientation of the UAV as the reference ($\phi = 0$). To further simplify the expression, we can neglect the two tilt angles of the UAV ($\theta = \psi = 0$). The expression reduce to:

$$|\hat{e} \cdot \bar{\hat{e}}| = c\beta c\gamma \tag{4.15}$$

Once again, we see that the polarization factor do not depend on the orientation of flight of the target. Effectively, it depends only on the orientation in which the tag was installed and the tilt of the hornet during flight. Neglecting the latter, we can size the tolerance on the attach method by choosing the maximum attenuation due to polarization mismatch.

For the case where we orient the direction of the main beam by tilting frontally the UAV antenna, we can not neglect this angle ($\theta \neq 0$). In this case, the polarization factor becomes:

$$|\hat{e} \cdot \bar{\hat{e}}| = c\alpha s\theta s\beta c\gamma + s\alpha s\theta s\gamma + c\theta c\beta \tag{4.16}$$

4.1.3 Conversion efficiency

The conversion efficiency of the tag is an important quantity to estimate in order to completely characterize the system. At this end, we can make measurements and extract the conversion efficiency. From eq. 4.10, we have:

$$\eta(\bar{P}_{RX}) = \frac{P_{RX}}{P_{TX}G} \left(\frac{2\sqrt{2}\pi d}{\lambda_h |\hat{e} \cdot \bar{\hat{e}}|} \right)^4 \tag{4.17}$$

We can measure the received power at a fixed distance depending on the emitted power. Additionally, we can position the tag and the RADAR antenna such that there is no polarization mismatch. The only remaining unknown is then the gain of the RADAR antennas. This gain can be easily determined using standard antenna characterization measurements.

Nevertheless, by doing this, we are only controlling P_{TX} and not $\bar{P}_{RX}$. To obtain the maximum range, we need to know the conversion efficiency depending on the target distance. Using eq. 4.10, we can write:

$$\begin{align}
\bar{P}_{RX} &= P_{TX} G'_{TX} \bar{G}'_{RX} \left(\frac{\lambda_f}{4\pi d} \right)^2 |\hat{e} \cdot \bar{\hat{e}}|^2 \tag{4.18} \\
&= P_{TX} G'_{TX} \bar{G}'_{RX} \left(\frac{\lambda_f}{4\pi} \right)^2 d^{-2} \tag{4.19} \\
& \tag{4.20}
\end{align}$$

We want to convert measurements taken with a variable P_{TX} with a fixed d to measurements with a fixed P_{TX} and a variable d. To develop this mathematically, we name $P_{TX,0}$ and d_0, the fixed emitted power and fixed distance respectively.

$$\begin{align}
P_{TX} G'_{TX} \bar{G}'_{RX} \left(\frac{\lambda_f}{4\pi} \right)^2 d_0^{-2} &= P_{TX,0} G'_{TX} \bar{G}'_{RX} \left(\frac{\lambda_f}{4\pi} \right)^2 d^{-2} \tag{4.21} \\
\Leftrightarrow P_{TX} d_0^{-2} &= P_{TX,0} d^{-2} \tag{4.22} \\
\Leftrightarrow d &= \sqrt{\frac{P_{TX,0}}{P_{TX}}} d_0 \tag{4.23}
\end{align}$$

We can summarize this methodology as follow:

1. We measure P_{RX} for a range of P_{TX} for a tag at a fixed and known distance using known transmitting and receiving antenna couple.
2. We divide each P_{RX} value by the corresponding P_{TX} and multiply by a known correction factor given by eq. 4.17.
3. We convert the P_{TX} axis to a distance axis using eq. 4.23.

Even though, we do not know the value of $\bar{P}_{RX}$ for each measurements because $\bar{G'}_{RX}$ is unknown [2]. We see that we can obtain the conversion efficiency of the tag depending of the distance.

4.1.4 Maximum range

The receiver and range/speed estimation requires a minimum signal to noise ratio. Then, knowing the noise power of the receiver and using eq. 4.10, we get a minimum received power.

$$P_{RX,min} = lin(P_{noise} + SNR_{min}) < P_{RX} = P_{TX} G \eta(d) \left(\frac{\lambda_h}{2\sqrt{2}\pi d} |\hat{e} \cdot \bar{\hat{e}}| \right)^4 \tag{4.24}$$

$$\Leftrightarrow \frac{d}{\sqrt[4]{\eta(d)}} < \sqrt[4]{\frac{P_{TX}}{P_{RX,min}} G} \, \frac{\lambda_h}{2\sqrt{2}\pi} |\hat{e} \cdot \bar{\hat{e}}| = K \tag{4.25}$$

$$\Leftrightarrow d < K \sqrt[4]{\eta(d)} \tag{4.26}$$

The distance region where the system is working can be visualized by plotting an unitary slope curve representing the d function and the fourth root of the conversion efficiency scaled by the factor given in the previous expression. All the valid distance will then be where the right hand side term is greater than the left hand side term.

Nevertheless, care must be taken for short distances as the link budget model described hereinabove is only valid for far field. From the well known Fraunhofer distance, we can determine a theoretical limit. In this application, as we are working with two frequencies, we effectively have two distance limits. We name D, the largest dimension of the antenna.

$$\begin{cases} d_{F,f} = \dfrac{2D^2}{\lambda_f} \\ d_{F,h} = \dfrac{2D^2}{\lambda_h} = 2d_{F,f} \end{cases} \tag{4.27}$$

$$\Rightarrow d >> \max\{d_{F,f}, d_{F,h}\} = d_{F,h} \tag{4.28}$$

This is valid only if the Fraunhofer distance is far greater than D or λ. To further analyze this limit and its possible consequences on the application and model, we need to know the largest dimension of the antenna. Therefore, the quantitative description of the model distance limit will only be available after the antenna has been designed.

[2] As a remainder, $\bar{G'}_{RX}$ is composed of the impedance mismatch and gain term. The latter can be estimated using standard values for monopoles. Nevertheless, the impedance mismatch depends on the frequency as well as the large signal biasing of the diode.

4.2 Analytical development of the FMCW equations

4.2.1 General expression of the different signals

In this work, the RADAR will emit a FM signal. It will be composed of N_p pulses of duration T_p and periodicity T. The general form of this type of signal is given by:

$$s(t) = \mathbb{R}\left\{\sum_{m=0}^{N_p-1} A_s exp(j\phi(t-mT))w_{T_p}(t-mT)\right\} = \mathbb{R}\{s_a(t)\} \tag{4.29}$$

with $w_T(t)$ the rectangular window function given by:

$$w_T(t) = \begin{cases} 1 & \text{if } 0 \le t < T \\ 0 & \text{else} \end{cases} \tag{4.30}$$

Suppose the transponder is placed at a distance. By travelling from the RADAR to the tag, the signal will be subject to a delay τ_d' and the channel noise. The configuration of the complete system is given in figure 4.1.

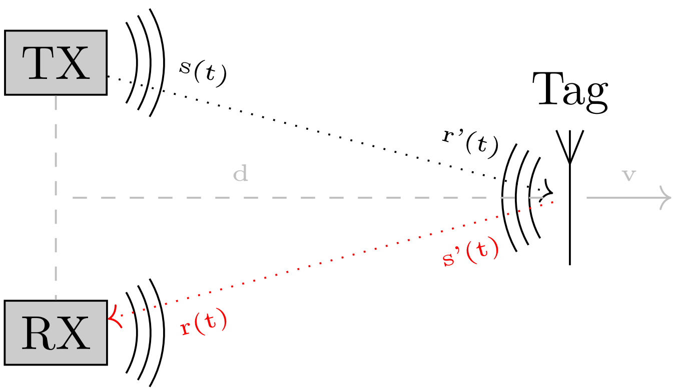

Figure 4.1: Configuration of the harmonic RADAR system and tag and naming convention of the signals. The RADAR is considered as monostatic for the distance and speed definition

We consider an additive white gaussian noise (AWGN). The total round-trip delay will be named τ_d and the AWGN component, $n_1(t)$. The signal received by the tag can be expressed as:

$$r_a'(t) = A_r' \sum_{m=0}^{N_p-1} \exp(j\phi(t-mT-\tau_d'))w_{T_p}(t-mT) + n_1(t) \tag{4.31}$$

The transponder doubles the frequency of this signal and reemits it back to the RADAR. Due to this conversion, the noise component becomes $\tilde{n}_1(t)$. The signal during the first chirp (for $0 \le t < T_p$) becomes:

$$s_a'(t) = A_s' \exp\left(j\int_0^{t-\tau_d'} 2\pi(2f(\tau))d\tau\right) + \tilde{n}_1(t) = A_S' \exp(2j\phi(t-\tau_d')) + \tilde{n}_1(t) \tag{4.32}$$

The signal received by the RADAR is then once again subject to the path delay and noise. We finally obtain:

$$r_a(t) = A_r \sum_{m=0}^{N_p-1} \exp(2j\phi(t - mT - \tau_d))w_{T_p}(t - mT) + \tilde{n}_1(t) + n_2(t) \tag{4.33}$$

4.2.2 FM modulation and delay model

The FM modulation used can be chosen by the designer. The classical choice is the linear frequency ramp modulation and will be used in the next developments. Its representation in the frequency-time domain is shown in figure 4.2a.

We can also show the frequency of the received and emitted signals. We see in figure 4.2b that the frequency of the received signal correspond to the frequency of the received signal for a classical linear ramp FMCW RADAR with twice the base frequency and bandwidth. Therefore, we expect to obtain similar results and methods for both an harmonic and classical RADAR in term of range/speed estimation and signal processing.

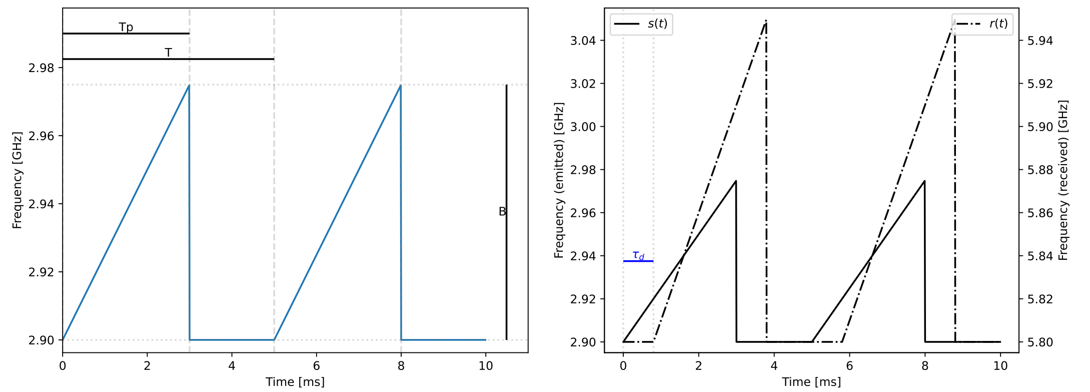

(a) Frequency of the signal composed of multiple successive chirps

(b) Frequency of the emitted and received signals with the base frequency placed on the same level. The left and right y-axes correspond to the emitted and received signal respectively.

Figure 4.2: Representation of the RADAR signal in the frequency-time domain

We define f_0, the carrier frequency; B, the bandwidth of the ramp and T_P, the duration of the pulse. The phase of the FM signal is given by:

$$\phi(t) = \int_0^t 2\pi f(\tau)d\tau = \int_0^t 2\pi(f_0 + \frac{B}{T_p}t)d\tau \tag{4.34}$$

$$= 2\pi(f_0 t + \frac{B}{2T_p}t^2) \tag{4.35}$$

As said in the previous section, the phase of the received signal is subject to a delay. This delay depends on the relative distance $R(t)$ between the RADAR and the tag. In this work, this distance will be modelized as $R(t) = d + vt$ with d, v the initial distance and speed of the target respectively. The delay is then obtained as:

$$\tau_d = 2\frac{d + vt}{c} = \alpha + \beta t \tag{4.36}$$

The phase of the received signal during a chirp is then given by:

$$\frac{\phi(t-\tau_d)}{2\pi} = f_0(t(1-\beta)-\alpha) + \frac{B}{2T_p}(t(1-\beta)-\alpha)^2 \tag{4.37}$$

$$= \left[\frac{B}{2T_p}\alpha^2 - f_0\alpha\right] + \left[f_0(1-\beta) - \frac{B}{T_p}\alpha(1-\beta)\right]t + \left[\frac{B}{2T_p}(1-\beta)^2\right]t^2 \tag{4.38}$$

$$= a_0 + a_1 t + a_2 t^2 \tag{4.39}$$

From eq. 4.33 the received signal during a chirp is then a second order polynomial phase signal (PPS) tainted by noise which is expressed as:

$$r_a(t) = A_r \exp(2j(a_0 + a_1 t + a_2 t^2)) + \tilde{n}_1(t) + n_2(t) \tag{4.40}$$

Due to the carrier frequency, the received signal is at high frequency. Therefore, we need to sample the signal rapidly which consumes a lot of power and computing power.

We can take the signal back in the baseband (low frequency) by mixing it with a frequency doubled version of the emitted signal. The mixed signal is given by:

$$y_a(t) = r_a^*(t)s_a(t) = A_y exp(j(2\phi(t) - 2\phi(t-\tau_d))) \tag{4.41}$$

$$= A_y exp(j\Phi(t)) \tag{4.42}$$

with

$$\frac{\Phi(t)}{2\pi} = \left[f_0\alpha - \frac{B}{2T_p}\alpha^2\right] + \left[f_0\beta + \frac{B}{T_p}\alpha(1-\beta)\right]t + \left[\frac{B}{2T_p}(1-\beta)\beta\right]t^2 \tag{4.43}$$

The parameters of the PPS becomes:

$$\begin{bmatrix} a_0 \\ a_1 \\ a_2 \end{bmatrix} = \frac{1}{2T_p}\begin{bmatrix} 2T_p f_0\alpha - B\alpha^2 \\ 2T_p f_0\beta + 2B\alpha(1-\beta) \\ B(1-\beta)\beta \end{bmatrix} \tag{4.44}$$

We can simplify the expressions by neglecting the quadratic terms of α and β. This can be supposed because $\alpha = 2d/v$ and $\beta = 2v/c$ are small in the context of our application.

$$\begin{bmatrix} a_0 \\ a_1 \\ a_2 \end{bmatrix} \approx \frac{1}{2T_p}\begin{bmatrix} 2T_p f_0\alpha \\ 2T_p f_0\beta + 2B\alpha \\ B\beta \end{bmatrix} \tag{4.45}$$

4.2.3 Parameter estimation

The general problem we want to solve is as follow, given the noisy measurements of the multicomponent polynomial phase signal $s[n]$ with $n = 0, 1, \cdots, N-1$, we want to estimate the phase parameters $\alpha_{0,0}, \alpha_{0,1}, \cdots, \alpha_{0,M}, \cdots, \alpha_{K-1,M}$ of each components. The signal is given by:

$$s[n] = s(nTs) = \sum_{k=0}^{K-1} A_k exp\left(j\sum_{m=0}^{M}\alpha_{k,m}(nTs)^m\right) + w(nTs) \tag{4.46}$$

We consider $w[n] = w(nTs)$, an additive white gaussian noise. We can define $\mathbf{a}_k = [\alpha_{k,0}, \cdots, \alpha_{k,M}]^T$ and $\mathbf{a} = [\alpha_0, \cdots, \alpha_{K-1}]^T$, the vectors containing the phase parameters of the different components.

In this work, we consider a single-component signal ($K = 1$) and a second order phase polynomial ($M = 2$). These two supposition can be justified by the context of the application. Indeed, we aim at only tracking a single target and the parasitic reflections from the background should be negligible thanks to the harmonic RADAR scheme. The received signal can then be approximated by a single component LFM signal.

Concerning the polynomial order, it depends on the target movement model. As said before, we will suppose that a first order model is sufficient to track hornets. This lead to a second order polynomial phase for the received and mixed signal.

Figures of merits for an estimator

There exist a lot of estimators and signal processing techniques that aim at solving this estimation problem. They can be grouped in different categories depending on what they are based on: phase unwrapping, maximum likelihood, discrete polynomial-phase transform (DPT), time-frequency domain, time-frequency rate domain, etc.

All these options could be used to estimate the distance and speed of the target. Nevertheless, they all have their trade-offs. Therefore, we must compare them using figure of merit to quickly assess their pros and cons.

The Cramer-Rao lower bound gives a limit on the variance for a unbiased estimator. An estimator that reach is limit can be considered as fully efficient. In general, estimators reach this limit above a certain value of SNR. Below this value, the RMSE decrease abruptly. This lead to the definition of a SNR threshold or a minimum SNR needed such that the estimator gives reliable results.

Phase unwrapping estimator

A simple idea for the parameter estimation of the phase of a complex exponential is to apply an arctangent. We obtain a phase estimation for each sample instant and by doing a quadratic regression, we get an estimation of the parameters of the second-order phase.

Unfortunately, the arctangent function can extract the phase of a complex without ambiguity if the phase is constrained between $-\pi/2$ and $\pi/2$.

To overcome this, we can apply transforms that will constrain the phase of the signal in this span. In [6], they applied a difference operator ($y[n] = s[n]s^*[n-1]$) to differentiate the phase of the signal. By applying it to time, the phase of the signal becomes $\frac{d^2}{dt^2}(a_0 + a_1 t + a_2 t^2) = 2a_2$ which can be constrained in $]-\pi/2, \pi/2[$ for $a_2 \in]-\pi/4, \pi/4[$.

Then by applying the arctangent and integrating (inverse of the difference operator), we recover the phase of the signal and we can perform a regression to obtain the parameters. We call this estimator DK in reference of the two author of [6].

This estimator is simple and can be computed in $\mathcal{O}(n)$. Nevertheless, it is subject to big shortcomings such as a high SNR threshold due to errors introduced by the difference operator.

Maximum Likelihood estimator

The maximum likelihood estimator (MLE) is the classical solution to the problem of estimating the parameters. In our problem (see eq. 4.46), this estimator can be expressed as[4]:

$$\hat{a_1}, \hat{a_2} = \underset{a_1,a_2}{arg\,max} \left| \sum_{n=0}^{N-1} s(nTs)\, exp\left(-j \sum_{m=1}^{2} \alpha_m (nTs)^m\right)\right|^2 \tag{4.47}$$

$$\hat{a_0} = phase\left(\sum_{n=0}^{N-1} s(nTs)\, exp\left(-j \sum_{m=1}^{2} \hat{\alpha}_m (nTs)^m\right)\right) \tag{4.48}$$

This estimation requires a 2D grid search in the frequency and frequency rate domain. It is computationally extensive and therefore impractical in real life application. Even more so that ours require real time computations to actively follow the target.

Many element of literature present research that aim to reduce this computational burden using, for example, better search algorithm [1] or Monte Carlo importance sampling [28].

In the specific case of a FMCW RADAR, we can reduce this problem to a 2D-FFT computation and a 2D-grid search. This can be seen by developing the signal expression for a series of chirp.

We consider that the breaks between pulses as been removed from the mixed signal and define the sampled signal as:

$$y[n + mNs] = y(nT_s + mT_p) \tag{4.49}$$

with T_s, the sampling period; $Ns = \lfloor \frac{T_p}{T_s} \rfloor$, the number of sample in a chirp.

We will see that the fact that the chirp signal is periodic while the delay is not (i.e for the mth chirp, we have $s(t - mT)$ but $\tau_d(t)$ and not $\tau_d(t - mT)$) will allow the expression to reduce to a 2D-FFT.

Using eq. 4.41 and considering multiple pulses as given in 4.33, we obtain:

$$\Phi(t - mT) = \phi(t - mT) - \phi(t - mT - (\alpha + \beta t)) \tag{4.50}$$

$$= f_0(\alpha + \beta t) + \frac{B}{2T_p}((\alpha + \beta t)^2 - 2(\alpha + \beta t)(t - mT)) \tag{4.51}$$

$$\approx f_0(\alpha + \beta t) - \frac{B}{T_p}(\alpha(t - mT) + \beta t(t - mT)) \tag{4.52}$$

$$\approx f_0(\alpha + \beta t) - \frac{B}{T_p}\alpha(t - mT) \tag{4.53}$$

Where we neglected the term in $(\alpha + \beta t)^2$ as it correspond to quadratic terms of α,β. The last approximation was obtained by supposing $\beta t < \beta N_p T_p << \alpha$ or $\frac{d}{v} >> N_p T_p$.

We now obtain the phase of the sampled signal as:

$$\phi[n+mN_s] = f_0(\alpha+\beta(nT_s+mT_p)) - \frac{B}{T_p}\alpha(nT_s+mT_p-mT_p) \tag{4.54}$$

$$= f_0\alpha + f_0\beta\, mT_p + (f_0\beta - \frac{B}{T_p}\alpha)nT_s \tag{4.55}$$

$$= f_0\alpha + f_0\beta\, mT_p - \frac{B}{T_p}\alpha\, nT_s \tag{4.56}$$

To justify the last approximation, we consider the case that α and β are of a similar order, $f_0 \propto$ GHz, $B \propto$ MHz and $T_p \propto \mu s$. We have $\frac{B}{T_p}\alpha >> f_0\beta \Leftrightarrow \frac{d}{v} >> \frac{f_0 T_p}{B} \propto 1e-3$ which can easily be verified.

We observe that the phase of the signal depends on α and β which are proportional only to n,m respectively. There is also the presence of a initial phase given by $f_0\alpha$. As the information is redundant with the term in nTs, we will skip its estimation. The estimation problems becomes:

$$\hat{\alpha},\hat{\beta} = \underset{\alpha,\beta}{arg\,max}\left|\sum_{m=0}^{N_p-1}\sum_{n=0}^{N_s-1} y[n+mN_s]exp(-j4\pi(\frac{B}{T_p}\alpha nT_s + f_0\beta mT_p))\right|^2 \tag{4.57}$$

$$= \underset{\alpha,\beta}{arg\,max}\left|\sum_{m=0}^{N_p-1} exp(-j4\pi\beta f_0\, mT_p)\sum_{n=0}^{N_s-1} y[n+mN_s]exp(-j4\pi\frac{B}{T_p}\,\alpha nT_s)\right|^2 \tag{4.58}$$

$$= \underset{\alpha,\beta}{arg\,max}\left|\sum_{m=0}^{N_p-1} exp(-j2\pi F_\beta n)\sum_{n=0}^{N_s-1} y[n+mN_s]exp(-j2\pi F_\alpha n)\right|^2 \tag{4.59}$$

with $F_\alpha = 2\frac{B}{T_p}T_s\alpha = 4\frac{BT_s}{cT_p}d$ and $f_\beta = 2f_0T_c\beta = \frac{4f_0T_p}{c}v$.

The last expression reduce to the application of a 2D-DFT on the sampled signal that was mixed with a frequency doubled image of the emitted signal. This 2D-DFT operation can be efficiently computed using the FFT algorithm.

The estimated distance and speed of the target becomes:

$$\begin{cases} \hat{d} = \dfrac{cN_s}{4B}\hat{F}_{alpha} \\ \hat{v} = \dfrac{c}{4f_0T_p}\hat{F}_{beta} \end{cases} \tag{4.60}$$

Limits of the estimator We can define some limits on the estimator using the fact that it reduce to the application of 2 FFT. Indeed, depending on the length of the FFT or periodicity of the normalized frequencies, the estimation have a limited resolution and range.

We can obtain the resolution of the estimator using the definition of the normalized frequencies F_α, F_β. The resolution is the minimum distance between target needed to be able to differentiate them.

From the resolution of the normalized frequencies $\Delta F_\alpha = 1/N_s$ and $\Delta F_\beta = 1/N_c$, we have:

$$\begin{cases} \Delta d = \dfrac{c}{4B}\dfrac{T_p}{T_s}F_\alpha = \dfrac{c}{4B}N_s\dfrac{1}{N_s} = \dfrac{c}{4B} \\ \Delta v = \dfrac{c}{4f_0 N_p T_p} \end{cases} \tag{4.61}$$

The ambiguity on the estimation can be expressed by noticing that the normalized frequency have a period of 1 and is therefore limited in the range $[-1/2, 1/2]$. This constrain the range of possible estimation as following:

$$\begin{cases} |\hat{d}| \leq \dfrac{cN_s}{8B} \Rightarrow \hat{d} \leq \dfrac{cN_s}{4B} \\ |\hat{v}| \leq \dfrac{c}{8f_0 T_p} \end{cases} \tag{4.62}$$

In the case of the distance, has it is defined as positive only, we can "reuse" the negative normalized frequencies and double the positive range ($F_\alpha \in [0, 1]$).

Zoom ML estimator

As seen before, the ML estimator in the case of successive chirps can be approximated as a 2D-FFT. Therefore the estimator exhibits similar properties with the FFT operator such as zero-padding and decimation.

By adding zeroes at the end of the signal, we can interpolate the results of the estimator and therefore increase its accuracy. Note that we do not add any information to the signal. This means that the resolution of the RADAR remains unchanged.

Additionally, if we apply a low pass filter and decimate the signal (downsampling), we can limit the highest frequency of the FFT spectrum.

From these two properties, we can try to reduce the execution time of the FFT. We will first do a coarse search to have a first estimation of the range and speed of the target. Then, we will create an estimated signal and mix it such that the remaining phase is centered around zero. Explicitly we estimate $\hat{d}_c$, $\hat{v}_c$, using eq. 4.56, we obtain the phase of the mixed signal as:

$$\phi_{mixed}[n + mN_s] = f_0(\alpha - \hat{\alpha}) + f_0(\beta - \hat{\beta})\, mT_p - \frac{B}{T_p}(\alpha - \hat{\alpha})\, nT_s \tag{4.63}$$

The signal now has parameters centered around zero. Notice that for the fine estimation, the "distance" can be negative. The equations and estimator are then slightly different. We will suppose that the maximum deviation of the error is of one half of a bin. Considering N_d and N_v, the number of sample used to make the coarse estimation in the time and chirp domain respectively, the maximum error is obtained by replacing N_s by N_d or N_v in eq. 4.61 and dividing by 2:

$$\begin{cases} \epsilon_d = \dfrac{cN_s}{8BN_d} \\ \epsilon_v = \dfrac{c}{8f_0T_pN_v} \end{cases} \tag{4.64}$$

Now, we can downsample and estimate a second time using more points. We want to limit the range of frequencies to the maximum error. By downsampling by a factor K_d and K_v, we limit the normalized frequency F_α and F_β to $[-\frac{1}{2K_d}, \frac{1}{2K_d}]$ and $[-\frac{1}{2K_v}, \frac{1}{2K_v}]$ respectively. We obtain the limits of the possible range for the fine estimation d_f and v_f:

$$\begin{cases} |\hat{d}_f| \leq \dfrac{cN_s}{8BK_d} = \dfrac{cN_s}{8BN_d} \\ |\hat{v}_f| \leq \dfrac{c}{8f_0T_pK_v} = \dfrac{c}{8f_0T_pN_v} \end{cases} \Rightarrow \begin{cases} K_d = N_d \\ K_v = N_v \end{cases} \tag{4.65}$$

We can finally obtain the range estimation by adding $\hat{d}_c$ and $\hat{d}_f$. Similarly, the speed estimation is obtained by adding $\hat{v}_c$ and $\hat{v}_f$.

The complexity of this estimator, with N'_d and N'_v the lengths for the fine 2D-FFT, is $\mathcal{O}(N_dN_vlog(N_dN_v) + N'_dN'_vlog(N'_dN'_v))$.

To compare it with the complexity of the standard MLE, we have to do some suppositions for the values of the lengths of the coarse and fine estimators. We will name M_d and M_s, the time domain and chirp domain FFT lengths respectively. We can compare the case where the two estimators have the same accuracy (ϵ_d and ϵ_v).

$$\begin{cases} \epsilon_d = \dfrac{cN_s}{8BM_d} \\ \epsilon_v = \dfrac{cN_s}{8BM_v} \end{cases} \text{and} \begin{cases} \epsilon_d = \dfrac{cN_s}{8BN_dN'_d} \\ \epsilon_v = \dfrac{cN_s}{8BN_vN'_v} \end{cases} \tag{4.66}$$

We obtain that the accuracy is equivalent when $M_d = N_dN'_d$ and $M_v = N_vN'_v$. We do the ratio between the two complexity. Considering $N'_dN'_v = N_dN_v$, we get:

$$C = \frac{N_dN_vlog(N_dN_v) + N'_dN'_vlog(N'_dN'_v)}{M_dM_vlog(M_dM_v)} \tag{4.67}$$

$$= \frac{2N_dN_vlog(N_dN_v)}{N_d^2N_v^2\,2log(N_dN_v)} = \frac{1}{N_dN_v} \tag{4.68}$$

We see that in this case, the complexity of the standard MLE is quadratically greater than the complexity of the Zoom MLE estimator.

In the literature, some low complexity FMCW estimator are based on the same 2 step (coarse-fine) method [14, 26]. The main goal of this procedure is to apply a high resolution or accuracy algorithm that have a high complexity (MUSIC and Chirp Z-transform respectively) on a subspace that was determined by the coarse estimation. In a real tracking the coarse estimation of the range and speed could be done using a bayes filter such as Kalman or Particle filter.

4.3 Simulation

Using equations 4.33 and 4.35, we can generate samples of the received FMCW signal[3]. Then, we can add complex noise, mix it and estimates the distance and speed using different methods. Finally, we can compute figure of merits and compare the different types of estimators.

To use the signal, we first need to remove samples between the chirps that only contain noise. We will simply use the delimitation of the emitted signal and considering the time shift induced by the delay as negligible.

Indeed, in general, this delay (τ_d) is smaller than the sampling period as we are considering a small operation range due to the harmonic radar high path loss (see link budget hereinbelow).

4.3.1 Sweep on distance

In this subsection, we will focus on the estimators performance depending on the distance parameter. We generate noiseless signals for all the radial distance points. Then, each estimator is applied on the signals and a distance estimation is obtained. The results are shown in figure 4.3.

We observe that the error of the DK estimator is quite constant for every values of distance. This is because of the analytical nature of the phase unwrapping method. The see that this estimator lead to a very low error (-90dB of error) for a noiseless signal. However, in practice, this estimator performances will be strongly reduced due to its sensitivity to noise.

For the other estimators, we observe a periodicity. We see that for without oversampling (blue traces), the maximum correspond at the values were the distance is a multiple of the resolution. When looking at the estimated values, we clearly sees the discretization steps.

With oversampling, the periodicity is increased and error reduced thanks to interpolation and the mean error is smaller. We can see that the estimated values better follow the reference curve. We see that for an oversampling factor of 4, the maximum are reached for multiple of 0.25 which is expected. For an oversampling factor of 16, the mean error is even lower (lead to a greater value as we are looking at the inverse of the absolute error).

Finally, we can take a look at the mean execution time in the table in figure 4.3. We see that the DK estimator has a high execution time. It may be caused by its unoptimized operations such as complex multiplication.

Additionally, we see that the ML estimator is faster than the ZoomML algorithm. This can be caused by the intermediary dechirping operation (see eq. 4.63). Nevertheless, for higher interpolation values, the ZoomML estimator scales at a much lower rate.

4.3.2 SNR threshold and execution time

We will now take a look at the RMSE of the estimators for different values of SNR.

A signal is generated for a target at a random distance and speed that are not multiple of the resolution. A complex noise is added to the samples of the signal with a variance

[3]Note that $\tau_d = \frac{d+vt}{c}$ depends on t and not $t - mT$ and thus change between chirps.

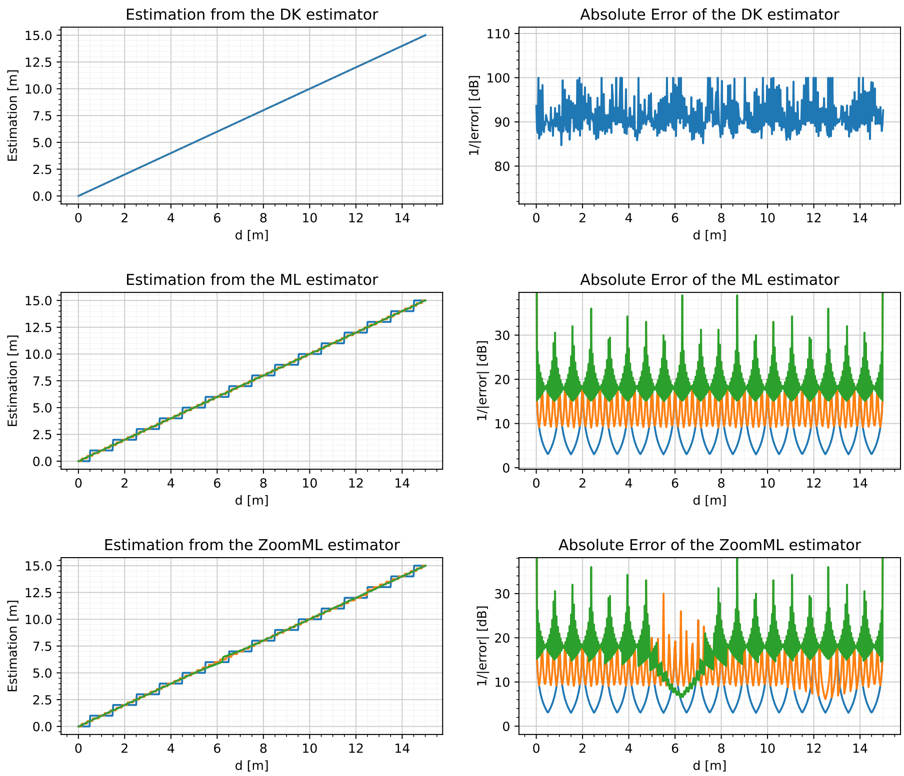

	DK	ML			ZoomML		
		1	4	16	1	4	16
Execution time [ms]	38.6	0.5	8.5	107.5	6.3	6.1	7.0
Mean 1/|error| [dB]	91.43	7.67	13.67	19.66	7.67	13.43	18.13
Std 1/|error| [dB]	3.74	7.18	6.87	6.57	7.18	6.97	7.31

Figure 4.3: Estimation for multiple values of distance for a static target. The signal has an infinite SNR (Noiseless). The harmonic RADAR parameters are chosen such that the resolution δd is 1m for the ML estimator. The values of the hyperparameters that are changed between estimators (oversampling of 1, 4 and 16) of the same type are indicated in the table below.

that depends on the current SNR and the signal amplitude. Then it is evaluated by the estimator and a value for the radial distance and radial speed is obtained. The error between this estimated value is then computed. This process is repeated 200 times for each SNR value. Finally, the errors of all these simulations is summarize using the root mean square error (RMSE).

The results are shown in figure 4.4. We observe that all estimators experience an abrupt reduction in performance below a SNR value. These values are summarized in figure 4.1.

We see that the DK estimator is the first one to fail at 19 dB. It is then unusable for SNR values that are below this points. This is an expected behavior as one of the assumption is that the SNR is high (see [6]).

The ZoomML estimators are the second to fail. This can be because we supposed that the maximum error resulting from the coarse estimation is one half of the resolution (As in the noiseless case). In the presence of noise, the maximum error can exceed this limit which results in incorrect measurements.

Finally, the ML estimator has very good performances even at very low SNR.

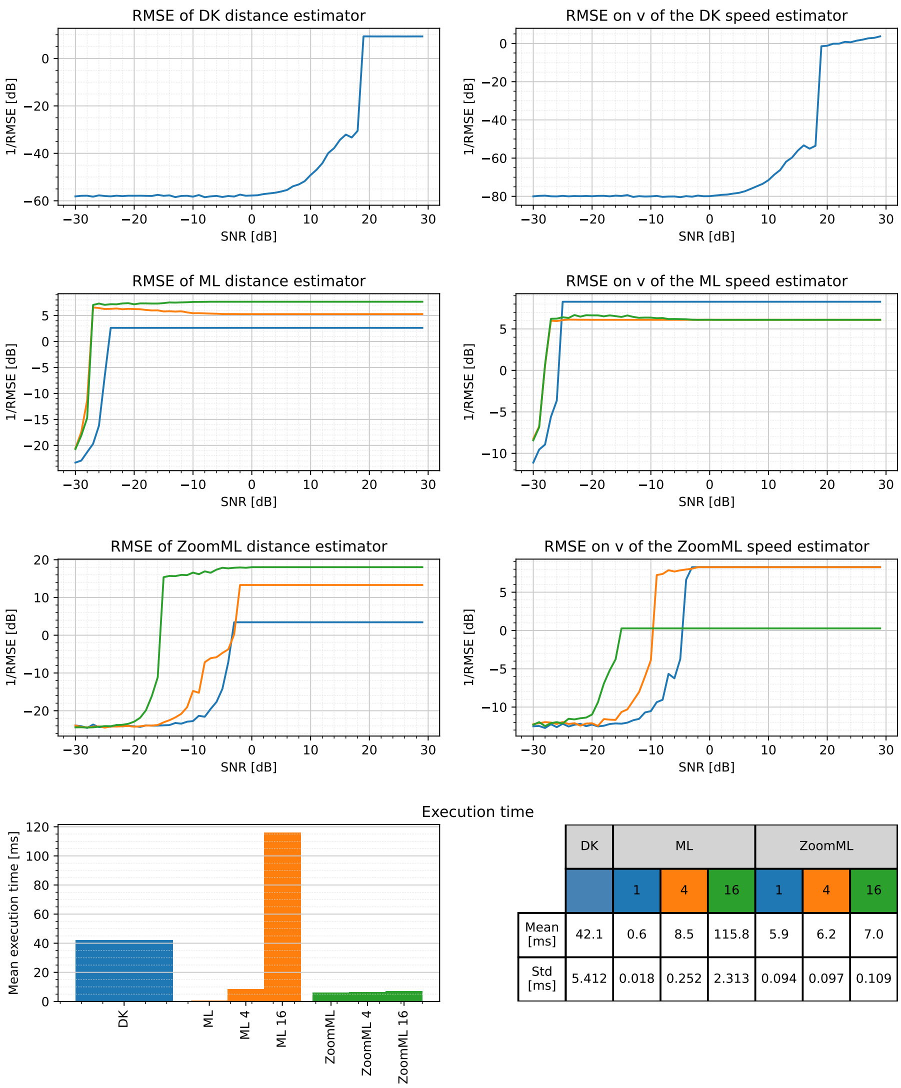

	DK	ML			ZoomML		
		1	4	16	1	4	16
Mean [ms]	42.1	0.6	8.5	115.8	5.9	6.2	7.0
Std [ms]	5.412	0.018	0.252	2.313	0.094	0.097	0.109

Figure 4.4: Results of the simulation of the effect of SNR on the estimator performances. The base signal correspond to a target with a distance of 12.45324 m and a speed of 6.4628 m/s. These values were chosen randomly such that they were not multiple of the resolution of the ML estimators.

Estimator	SNR threshold [dB]
DK	19
ML	-24
ML 4	-27
ML 16	-27
ZML	-3
ZML 4	-2
ZML 16	-5

Table 4.1: SNR threshold of the different estimators. It correspond to the SNR from which the RMSE falls arbruptly.

Note that, in these simulations, we have considered that the signal is a perfect single tone complex exponential. However, in practice, non-idealities affects the signal in the form of harmonics or phase noise. These can affect the estimators performances and modify the observed results.

Finally, we take a look at the execution time once again to have a larger number of sample. We see that the general tendencies are similar.

The DK estimator is the slowest and the ML and ZML estimators increase with the oversampling factor. This increase of execution time is far more important for the ML estimator than the ZML estimator.

Chapter 5

Design of the RF circuit

In this chapter, we will design the complete RF chain of the RADAR. It will be composed of two parts: the transmitter (TX) and the receiver (RX).

The TX will be fed an input FMCW signal and will amplify it before sending it to the emitting antenna (in fundamental band). Its saturated power should be as high as possible as it correspond to the P_{TX} term in equation 4.10.

The RX is fed the signal coming from the receiving antenna (designed for the harmonic band). It then mix it with the emitted signal. The resulting signal is at a lower rate, which allows to sample it at a lower rate. The receiver chain must amplify the received signal such that it falls inside the allowable range of the ADC.

In the first section, we will discuss about the different package in which the circuit can be build. We will compare three options: Connectorized module, printed circuit board and Quantic X-Microwave (XMW) design platform. Then we will build the system architecture. Finally, we will selects the components.

5.1 Package options

Multiple options and components package are available. In this work, we will consider the following possibilities: Connectorized module, PCB and Quantic X-Microwave design platform.

In the following subsections, we will precise the pros and cons of each possibility and select the one we will use. The criteria we will focus on are the weight, the compactness and prototyping capabilities.

5.1.1 RF connectorized module

The most used package in prototyping of RF circuit are the connectorized modules.

Connectorized version of RF components are widely available on the market. A circuit build with connectorized module can be seen as a graph of independent microwave circuit encased in metal boxes and connected to each other through connectors such as SMA connectors.

A circuit can be easily implemented using these modules. Indeed, we can simply connects the different blocks directly or using coaxial cables.

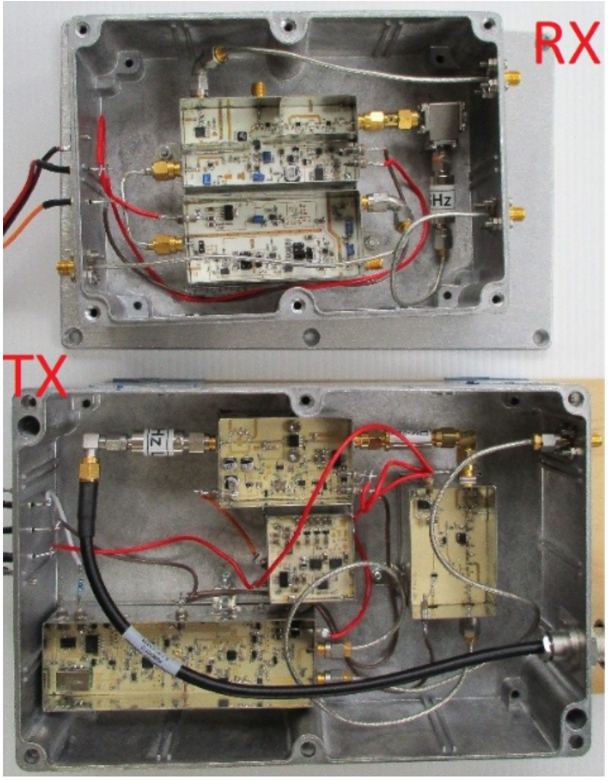

Figure 5.1: Example of an RF circuit built using connectorized modules. It is an harmonic radar prototype in the S band (TX:2.9GHz; RX:5.8GHz) from [31].

Pros and cons

The main advantage in using this type of package for prototyping is that the circuit can easily be modified. Indeed, no permanent connections are made. For example, if we want to change a component such as an amplifier, we can simply disconnect its inputs and outputs and swap it with the new amplifier.

However, due to the metal casings, cables and the need for an external structure[1], the total weight of the prototype is quite high. Additionally, the maximum density of components is quite low compared to other solutions (see figure 5.1).

To summarize, the connectorized module is well suited for the early prototyping phase to allow for tinkering. It has a low component density and a high weight.

5.1.2 PCB, SMD components and printed lines

Most RF components are available in SMD package. We can use these components to build a complete RF circuit on a printed circuit board. We can then connects these component as well as design the bias/matching circuits using printed lines such as microstrip line (ML) or conductor coplanar waveguides (CPW).

It is a very versatile and compact solution as the designer has full control over all the aspect of the design.

[1]The module must be mechanically fixed, usually with a wooden plank, to avoid stress on the cables or to facilitate the transport of the prototype.

Pros and cons

The main advantages in using this form factor is its high component density and low weight. It also minimizes the insertion loss of the interconnects due to their small length.

Nevertheless, these advantage comes with some inconvenient. To begin, the design is very demanding as everything must be taken into account. For example, the digital part of the circuit is usually done on the same board. Therefore, special care must be taken to prevents the parasitics coming from the large spectral content of the digital circuit from affecting the highly sensitive analog and RF part. Then, the design is hardly modifiable once it is built. To be able to swap a simple part such as an amplifier, the SMD package must have the same footprint and the matching/biasing circuits must be compatible. These two conditions (more specifically the second) can be very hard to fulfill.

To summarize, PCB and SMD components plays a central role in RF circuit design. It is best suited for final design thanks to its high density. The design of such a circuit can be hard and time consuming but lead to results that are most suitable for a system carried by an UAV (small size and weight).

5.1.3 Quantic X-Microwave

Quantic X-Microwave is a company that is focused on high performance RF and microwave circuit for highly demanding industries[34]. They offer a new approach of RF circuit design thanks to their modular design platform. This allows for a shorter, easier and lower cost prototyping phase.

Indeed, it can be placed in the midpoint between the two other form factor. It can be described as RF modules designed in conductor-backed coplanar waveguide (CPWG) on PCBs and connected using ground-signal-ground jumper instead of coaxial connectors.

Design platform

This platform consists of a board, component modules and some other auxiliar elements such as a voltage regulators and control. The board is build from a conducting material that serves as a common ground plane. The modules are placed on top of it and pressed down such that the exposed ground plane of the PCB is connected to the board.

These different modules are implemented around SMD components on a printed circuit board using CPWG technology. They are connected to each other using small pieces of polymer with 3 printed traces for the ground-signa-ground conductors of the CPWG (i.e. the GSG jumper).

Fixtures are also proposed to convert the signal in a CPWG to coaxial waveguide. These are called XM-probe and are precision piece that will press the conductor of the coax onto the printed signal trace and its metallic body onto both adjacent printed ground plane.

Finally, the bias and control is connected by attaching these circuits to the bottom of the metal plate. Signal is then connected to the upper side using spring pins going through the screw holes.

Quantic X-Microwave also offers metallic walls and roof to completely encased the components in metal. This improve the sturdiness of the prototype and protects it from electromagnetic interferences. It then becomes comparable with a circuit implemented connectorized modules.

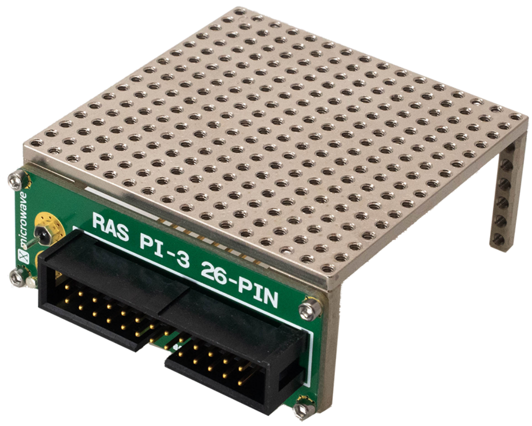

(a) Quantic X-microwave board

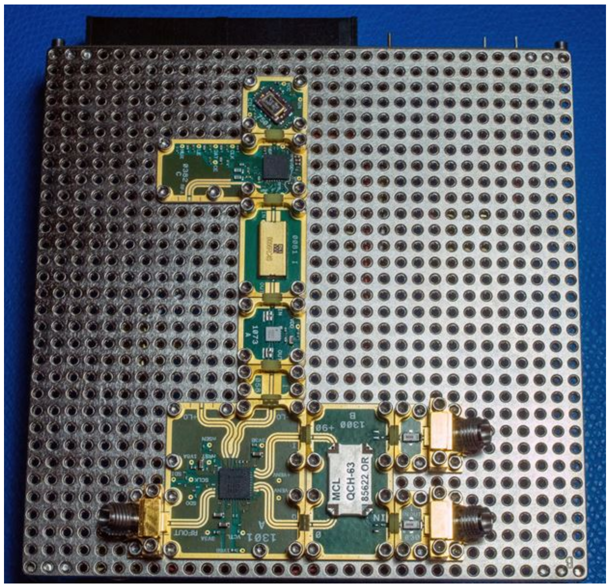

(b) Component placed on the plate (reference design kit)

Pros and cons

This form factor combines the two others in term of pros and cons. It is compact, lightweight and can easily be modified thanks to its modular design.

It is also a good approximation to a circuit built on PCB as the intermodules connections are quite similar to an uninterrupted CPWG trace. It can then be designed while neglecting the losses between modules unlike the connectorized modules that have connectors and cables with non-negligible losses between each other.

However, it is also worse compared to the other two in certain aspects. For examples, placing the GSG jumper, verifying the placement using an optic and tightening all the screws takes far longer than the simple operation offered by coaxial connecters. Because of the metal board and different additional elements, it is also heavier than a SMD circuit and the library of available components is limited.

In summary, this design platform offers a new modular way to design RF circuit. The prototype is closer to PCB implementation of the circuit than connectorized modules while being easily convertible to a more robust prototype for on-field experiments using metal casings. It also falls behind the other two when it comes to their specific strengths (plug and play for connectorized modules and compactness of PCB circuits).

5.1.4 Conclusion

These three options all have different use cases. Connectorized module are well suited for quick assembly of a RF circuit for a first proof-of-concept prototype or measurement setup where optimal performance (connectors causes additional insertion losses) or compactness is not a requirement.

PCB lead to very compact and finished products. However, it is not compatible with an iterative design.

The Quantic X-microwave platform is at the midpoint between the two other solutions. It offers a way to design RF PCB in a modular way which allows for a simpler and quicker iterative process.

Nevertheless, these three form factor does not have to be used separately. For example, one can split its circuit into multiple parts and build them using independent PCB. These parts can then be connected using the XMW platform or coaxial connectors and cable.

Similarly, a chain of connectorized blocks can be fused onto a single PCB to be more compact.

In this work, we choose to work with the Quantic X-microwave platform instead of connectorized modules. This choice is made to try the design platform as well as explore a solution that is lighter closer to a single PCB.

Indeed, as an example, the prototype presented in [31] built with connectorized modules (see figure 5.1) is quite heavy (3 kg). From the picture, we see that it consist in multiple PCBs connected using coaxial cables and encased in a big metal box. This metal case is the main contributor to the prototype weight. However, this box cannot be made significantly smaller due to the space needed for the cables[2]. By reducing the amount of PCBs (fusing them together), we reduces the amount of cables and the size of the protective metal casing, drastically reducing the weight. However, this fusion cannot be done simply by putting them together as proximity effects such as thermal conduction from the power amplifier or digital corruption from the sampling chain are added. Having a prototype that is closer to a single PCB while staying modular is desirable.

5.2 Component selection

In this section, we will choose the different components that will compose the radar circuit. We will divide this discussion into two parts: the transmitter and receiver. For the complete design process, we will suppose that the insertion losses of the GSG jumpers and fixtures are negligible.

5.2.1 Transmitter

In this work, we will focus on the amplification chain and signal generation will be ignored.

The transmitter takes an input FMCW signal and has two output: the transmitted signal and LO signal. To provide the highest available power, we begin by choosing a power amplifier that has a high OP1dB[3]. We end up choosing the A5T5 block from Quantic XMW. This module is based on the ADL5324 from Analog Devices. It is a 400 MHz to 4 GHz power amplifier with an OP1dB of 28 dBm (around 0.5W) and a gain of around 13 dB around 2.9 GHz. Its input power must then be around 15 dBm to reach the saturated output power of the amplifier.

Additionally, the ADL5324 also implements a dynamic biasing. Its bias voltage can be changed dynamically from 5V to 3.3V to reduce the power consumption at the cost of P1dB and IP3[4]. This capabilities can be useful to better control the power which is important for embedded circuits.

[2]All coaxial cables can only be bend in a certain amount without being damaged. The relative figure of merit is the bending radius.

[3]Output power at the one dB compression point

[4]Intermodulation products of the 3rd order

To split the input signal into the LO and TX branches, we use a simple 3 dB power divider (A1K6) as the available couplers have only limited ratios. As the power is the same at the two output ports of the power divider, we have an available power of 15 dBm (due to the power amplifier compression). Furthermore, as the LO branch must perform frequency conversion, high losses are to be expected. The mixer we will choose in the next section needs a LO power of 4 dBm to operate in optimal condition. Then, to obtain a LO signal that as this power level, we need a frequency doubler that has around 11 dB of conversion loss (CL). We end up choosing the A129 frequency doubler that has a CL of 12 dB and a maximum input power of 17 dBm. The expected LO power is then 3 dBm instead of 4 and the mixer will operate in suboptimal conditions. A better result could be achieved by designing a power divider that has the perfect ratio to have the optimal LO power.

Then, we add a preamplification stage as the current input power needed is 18.5 dBm which is high compared to signal generators output power. We select the A114 amplifier that has a gain of 17 dB at 2.9GHz and that operate 2.9 dB lower than compression (OP1dB of 20.9) to reduce the non-linearities of the LO and TX signal. The input power of the transmitter is then 1.5 dB instead of 18.5.

Finally, we add a low pass filter (LPF) between the power amplifier (A5T5) and TX port to reduce the leakage of harmonic power from the transmitter. Indeed, as we are designing a harmonic RADAR, the receiver is sensitive to power at the second harmonic of the transmitted signal. This power must come from the tag placed on the target. Therefore, if the transmitter emits power at the second harmonic, it can reduce the global performance of the radar. A low pass filter with a cutoff frequency between the fundamental and harmonic frequencies, we can attenuate the latter. The chosen filter is a A1B2 with a cutoff frequency of 3600 MHz and a 40 dB attenuation around 6GHz.

The complete transmitter circuit is given in figure 5.2.

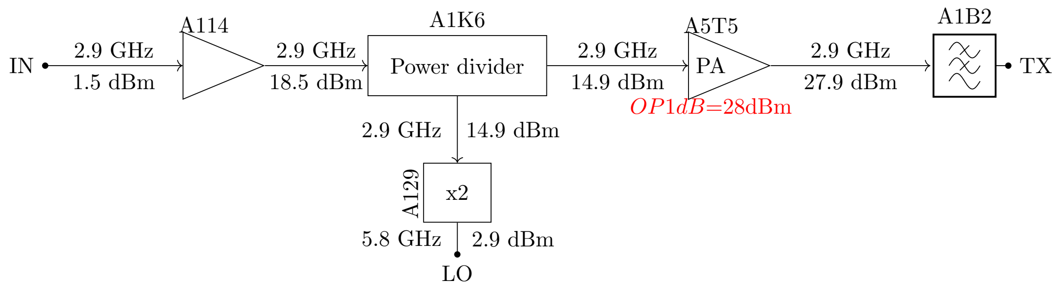

Figure 5.2: Design of the transmitter. The different power level and frequencies are shown.

5.2.2 Receiver

The receiver central component of the receiver is the mixer. It takes the LO signal and the RF signal and produce a signal that has a frequency corresponding to the sum and difference of the two input signals. As said during the component selection for the transmitter, we choose the C9E5 mixer that has an optimal LO power of 4 dBm. Its conversion loss for an optimal LO power is 6.5 dB.

The second purpose of the receiver is to amplify the signal to a power level that is acceptable by the ADC. The main characteristics of a receiver are its gain and noise figure (NF). To minimize the noise figure of the whole chain, one should put a high gain and low noise block at the beginning of the chain.

Indeed, the gain of a block reduces the contribution of the NF of all subsequent blocks. This is the purpose of an LNA. It is then one of the most sensitive component of the receiver chain. Unfortunately, a mistake was made when selecting the LNA and the gain was incorrectly read from the datasheet. Indeed, the gain of the selected LNA (A2N4) has a gain of 6.68 dB which is relatively low for an LNA. A far better choice would have been the D515 for example as it has a gain of 26.5 dB and a noise figure of 0.9 dB. This alternative will be studied in a later section of this work.

The receiver also contains other amplifiers. As they are further down the chain, their effects and characteristics are less important. If the LNA gain is high enough, we can add as many amplifiers as we want without degrading significantly the receiver performances in term of noise figure. What sets the limit in term of amplification is the maximum input power of the different devices (compression point of the amplifiers and maximum input power of the mixer and ADC).

In this work, we will select a single additional amplifier that as a wide band such that it can be placed in both IF and RF side of the mixer. This amplifier can then be used in both part of the RX or as an pre-amplifier for measurements thanks to the modularity of the design platform. We select the D2B4, a 0-8000 MHz amplifier that as a constant gain of 14 dB on the 0-6000 MHz band.

The final components of the receiver are the filters. There are two filters in the receiver. A LPF is put at the end of the IF chain to prevent aliasing due to sampling.

The second is a BPF that is placed at the start of the RF chain. It has two purposes, first it prevents out of band noise from falling back into the baseband due to mixing. Its second purpose, that is specific to a harmonic radar, is to attenuate the fundamental signal coming from the TX through the receiving antenna. Indeed, a considerable amount of TX signal can leak to the receiver. If this power becomes large enough it can saturate the LNA or other RX amplifiers. This is why we can not put this filter after the LNA to reduce the NF of the filter caused by its insertion loss.

The receiver circuit is shown in figure 5.3.

5.2.3 Modification of the power amplifier (A5T5/ADL5324)

The ADL5324 (IC of the A5T5) can be tuned to a specific frequency range (between 400MHz and 4GHz) by changing the lumped components of its matching circuits. However, the A5T5 is not initially matched at 2.9 GHz.

When received, the amplifier is tuned for 2.14GHz. We must change the values of the matching components. Unfortunately, the substrate used for the XMW circuit is not the same as the ADL5324 evaluation board and the datasheet does not provide values for the band of interest of this work. Therefore, we have to simulate the device and its matching circuits to be able to tune it without having to solder/desolder the components multiple time.

A first simulation was done based on the deembed S-parameters provided by Analog

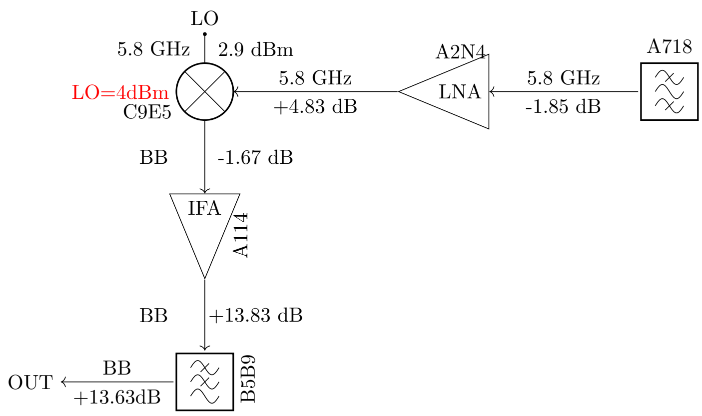

Figure 5.3: Design of the receiver. The different power level and frequencies are shown.

Device. The substrate and CPWG parameters were set using information given by Quantic XMW and from the CAD model of the A5T5 respectively. These parameters are given in table 5.1.

Symbol	Description	Value
h	Height of the substrate	0.203 [mm]
w	Width of the central conductor	0.43 [mm]
s	Spacing between the central conductor and the ground planes	0.28 [mm]
ϵ_r	Relative permittivity of the substrate	3.55 [-]
t	Thickness of the conductor	30 [μm]
tanδ	Delta tangent of the substrate losses	2.7e-3[-]
ρ	Resistivity of the conductors	24.4 [$n\Omega/m$]

Table 5.1: Parameters of the coplanar waveguide with ground (CPWG) used by Quantic X-microwave for the A5T5.

The matching circuit consist of a shunt and a series capacitances (see C1,C3 and C2,C7 in figure 5.4). The tuning of the matching circuit was done only on the shunt capacitances as the series cap. have close values compared to the one used in the datasheet for the configuration in the closest frequency band (2630MHz). The values of the series capacitances were assumed to be 2.4 pF and 20 pF for C3 and C7 respectively. The simulation was done using Advanced Design System (ADS) and the circuit model used is shown in figure 5.5

The resulting S-parameters are given in figure 5.6. First, we see that the initial configuration is indeed matched at 2140 MHz. Secondly, we see that the new matching leads to very bad results. From the reflection coefficients (S11, S22), we see that the S22 is especially badly matched around 3GHz (S22 is near 0dB). This matching is inconclusive and must be retuned.

To be certain of the matching capacitors values, we change the series capacitor with new capacitors that have a known value (2.4 pF and 20 pF for C3 and C7 respectively). We will also measures the S-parameters of the A5T5 without shunt capacitors to obtain a better simulation model. We left the series capacitors to protect the VNA as they act as

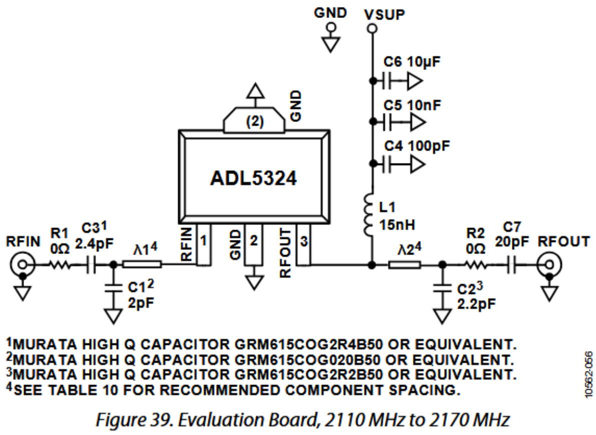

Figure 5.4: Diagram representing the ADL5324 and its bias and matching circuits.

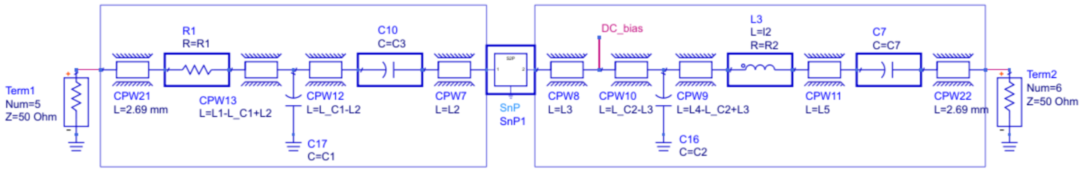

Figure 5.5: ADS model of the ADL5324 and its matching circuits. The thick blue square indicates the component that have a fixed position due to the trace layout (gap in the transmission line to place the series components).

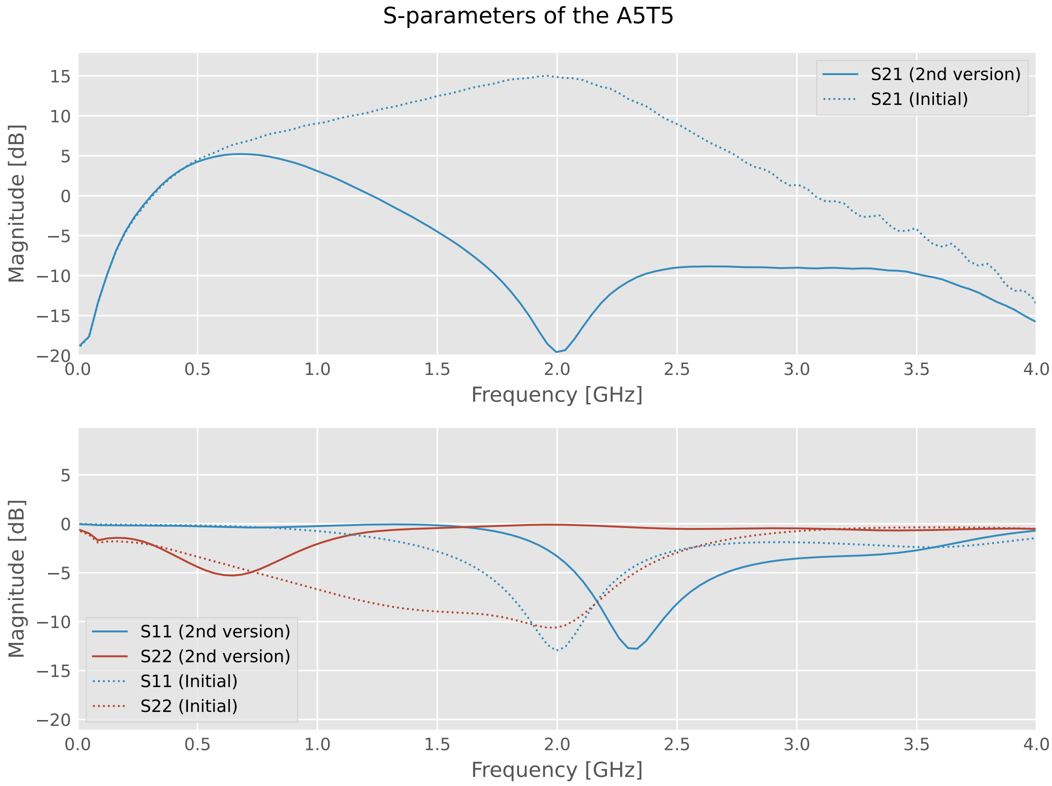

Figure 5.6: S-parameters of the A5T5 in its initial configuration and 2nd version after the first redesign of the matching circuits in ADS.

DC block.

To obtain the S-parameters of the bare ADL5324, we mathematically remove the CPWG lines between the measurement ports and the DUT ports. We also remove the effects of the series capacitors (C1 and C7). The S-parameters we obtained are shown in figure 5.7. We see that the measured S-parameters correspond to quite well with the one with the one provided by the manufacturer. Still, we replace the S-parameters used in the simulation by the one we measure as they should better describe our ADL5324 and there is no inaccuracies due to device to device variations.

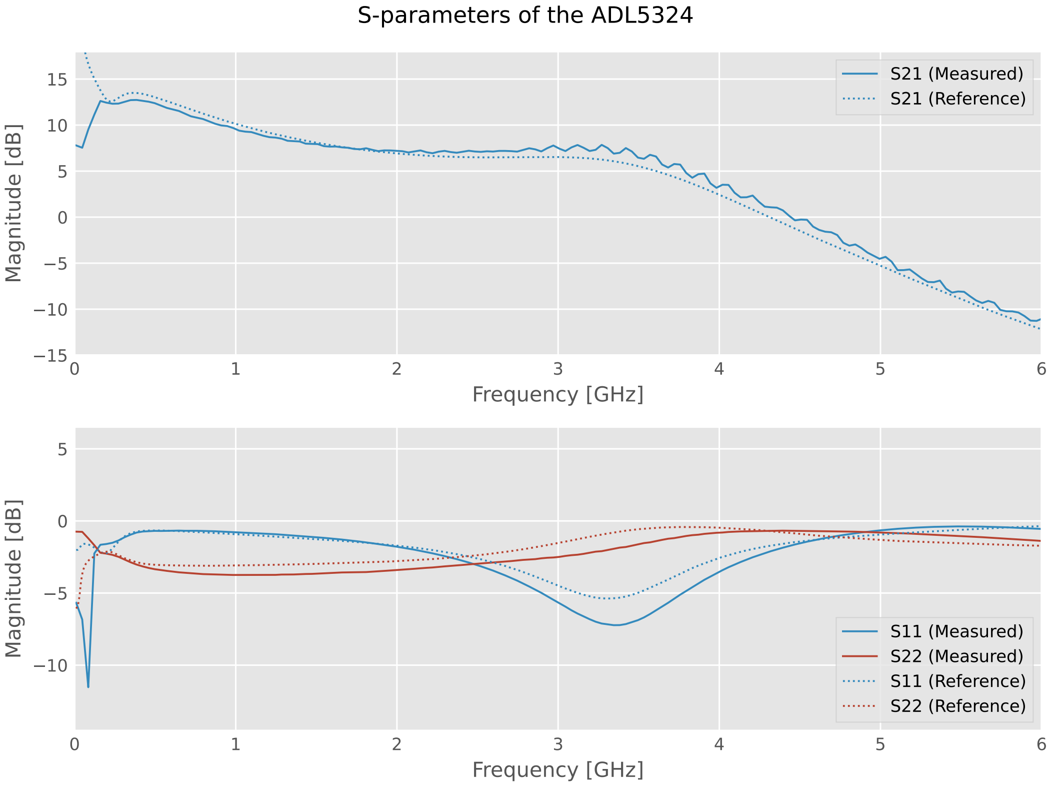

Figure 5.7: Deembedded S-parameters of the A5T5. They correspond to the S-parameters of the ADL5324 at its ports. The parameters given by Analog Device (Reference) are compared to the one measured.

A new tuning is performed in simulation. In order to prevent having to resolder the capacitors multiple time, we first test the matching by measuring the reflection coefficients at each port while pressing down the new capacitors at their desired location. As the results were similar to the simulation, the capacitors were soldered in their new location.

The results are given in figure 5.8. We see that the gain of the A5T5 at 2.9 GHz is about 13 dB. The matching at port 2 is in resonance at the desired bandwidth leading to a reflection coefficient below -10 dB over the bandwidth. Unfortunately, we see that, at port 1, the resonance occurs at a higher frequency than expected.

The input impedance of one port of an amplifier depends on the load presented at the other port. This means that a simple S-parameters which describe a linear behavior is not sufficient. This can be the cause of the observed difference in matching at the port 1. If we want to improve the matching, we can do a new measurement with only the port 2 shunt capacitor. Then the new model should lead to a better matching. Nevertheless, as the gain is good is the band of interest, we will stop modifying the circuit.

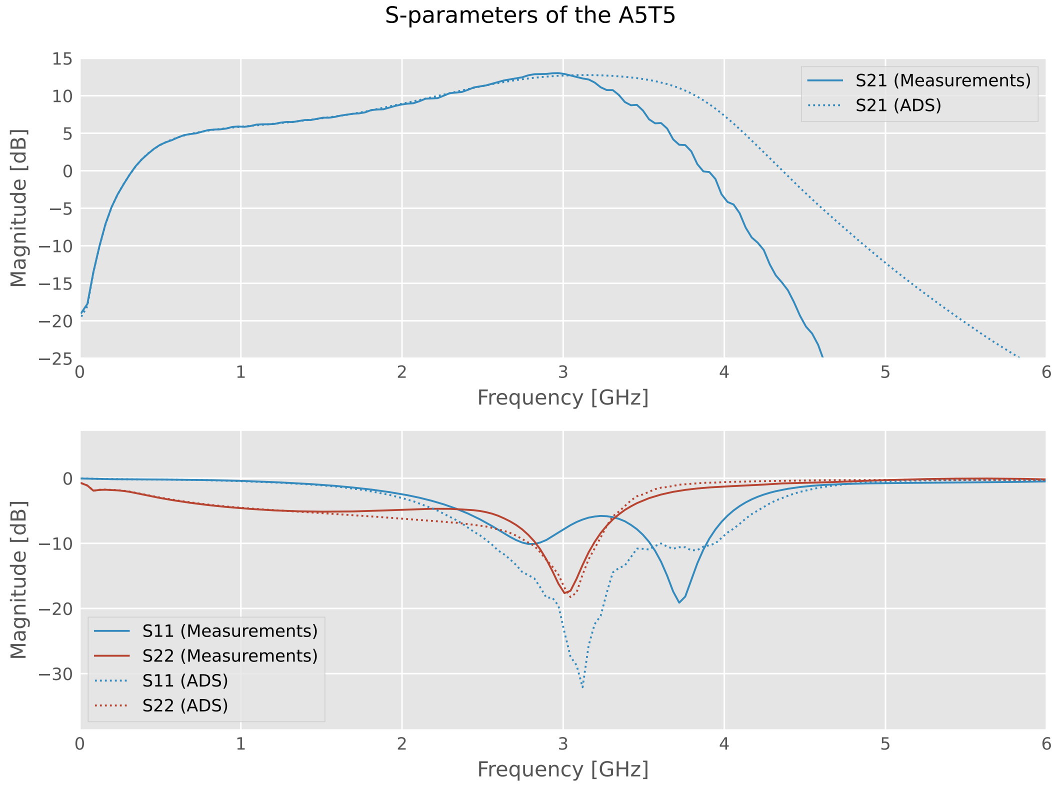

Figure 5.8: S-parameters of the A5T5 in its final configuration (tuned for 2.9 GHz).

5.2.4 Complete circuit

The complete RADAR circuit is given in figure 5.9

The IN port correspond to the FMCW input signal. The OUT port correspond to the resulting mixed signal that must be sampled.

The TX and RX port correspond to the TX and RX antenna respectively.

At this stage, we already have multiple ideas for improvements.

First, as said before, the LNA was poorly chosen. Using a better LNA will immediately improve greatly the performances of the receiver.

Then, the current design supposes that the antennas are matched. As it is hardly the case, matching circuits must be added the TX, RX ports and the antennas.

Finally, more amplifiers can be added to the RX chain. and the LO power can be increased to reach the optimal 4dBm value.

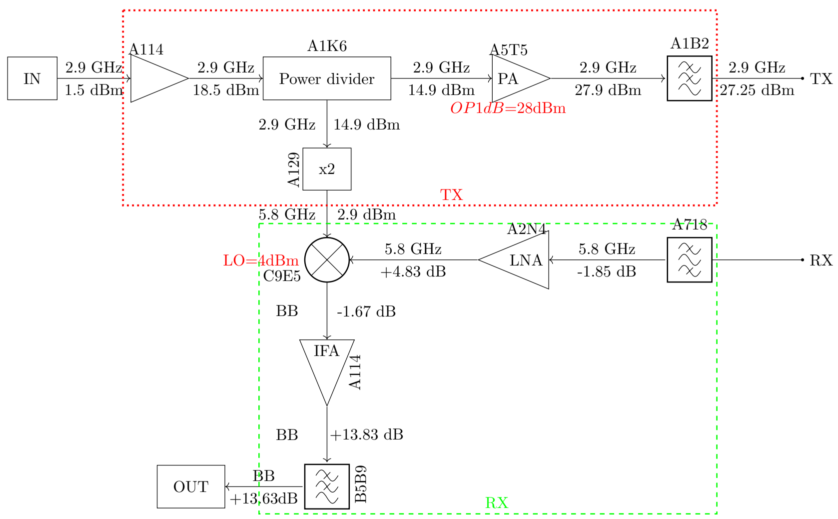

Figure 5.9: Complete design of the RADAR. The name of the XMW block are given for all the components. The expected power (TX) or gain (RX) is shown at each step.

Chapter 6

Choice and design of the antenna

As said in section ??, in this work, we will focus on the azimuthal angle detection to simplify the architecture. This has a direct repercussion on the antenna design.

As the radar is directly mounted on an UAV, we can freely rotate its referential around the vertical axis. The angle detection could then be implemented solely using the mobility of the vehicle.

However, this means that the UAV must do a large amount of maneuvers to be able to scan a large angle range. This can complexify how the UAV is driven as it must then keep the target in the main beam of the RADAR as well as following the target while avoiding obstacles. Therefore, we will perform angle scanning with the RADAR to reduce this burden.

Nevertheless, we can still use the mobility of the UAV for the small angle scanning. The RADAR will then coarsely determine the target direction and the UAV will perform small adjustments. This approach can be justified by the fact that, because of the short range, a general direction is sufficient to follow the target.

In the following section, we will explore the concept of switched antenna array.

6.1 Principle of switched antenna array

A switched antenna array is composed of multiple antenna elements that are connected to the RF circuit through RF switches. These switches change the shape of the radiation pattern by controlling which elements are powered. Two examples of such arrays are given in [12] and [16].

The most basic idea with switched antenna array is to associate each directions of scanning to a single element. By selecting the powered element, the direction of the main lobe is chosen. Thus, we can achieve a a large scanning range using a simple architecture composed of a small number of antenna element.

An example of an antenna array with 8 directions for a scanning range of 360° is shown in figure 6.1. Each element is a monopole with two ground planes. These elements have a main beam in the direction of the monopole from the vertical axis at the center of the structure.

As the different radiation patterns overlap, the complete 360° range is scanned. The resolution is then $360°/8 = 45°$ which is quite a poor resolution. In our case, as the small

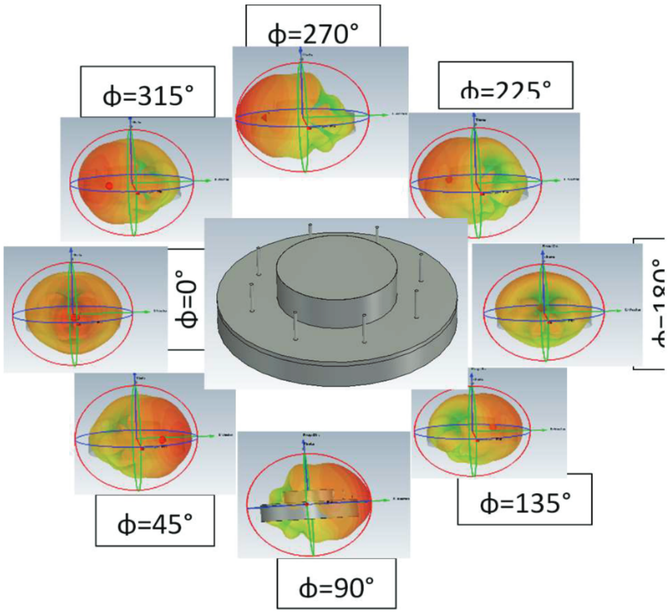

Figure 6.1: Switched antenna array described in [16]

angle scanning can be performed by the UAV, we can suppose that this poor resolution is not impacting the functionality of the system.

6.1.1 Increasing the angular resolution using true delay lines

If a higher resolution is required, one could increase it while keeping the same switched antenna array.

As described in [12], we can increase the number of scanning direction in a very simple and cheap manner using only some true delay lines and additional RF switches. However, to be able to implement this, the radiation pattern of successive elements must have a significant overlap (e.g. see fig 6.2a). This overlap allows for a significant interference between the two antenna such that the radiation pattern is modified.

6.2 Design of the cake antenna

In this work, we need two antennas: the fundamental and harmonic antenna. These two antennas work around 2.9 GHz and 5.8 GHz respectively.

We will base the design of our antennas on the hat antenna described in [16]. This choice was motivated by the simplicity of its fabrication and the possibility of stacking the two antennas. The obtained geometry resembles a cake with candles (see fig 6.3) and we will thus call this antenna, the cake antenna.

6.2.1 Results of simulation in CST studio

The antenna was simulated using CST studio. We begin with the model of the hat antenna scaled for the fundamental frequency. Then, a second scaled version of the hat antenna is placed on top of it.

From these simulations, we can optimize the dimensions of the antenna to maximize the gain. The optimization strategy is the following, first we performs sweeps of the

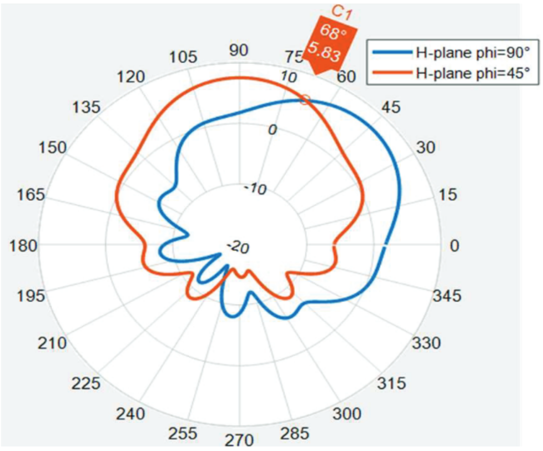

(a) Overlap of consecutive elements of the hat antenna [16]

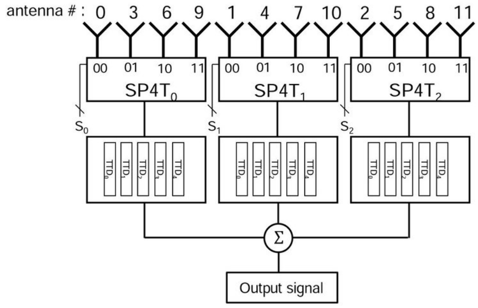

(b) Architecture of the beamforming in [12]. The 3 transmitting antennas are selected by the three SP4T. The phase shifting is performed using true delay lines (TTD) and SP5T switches not shown on the diagram.

Figure 6.2

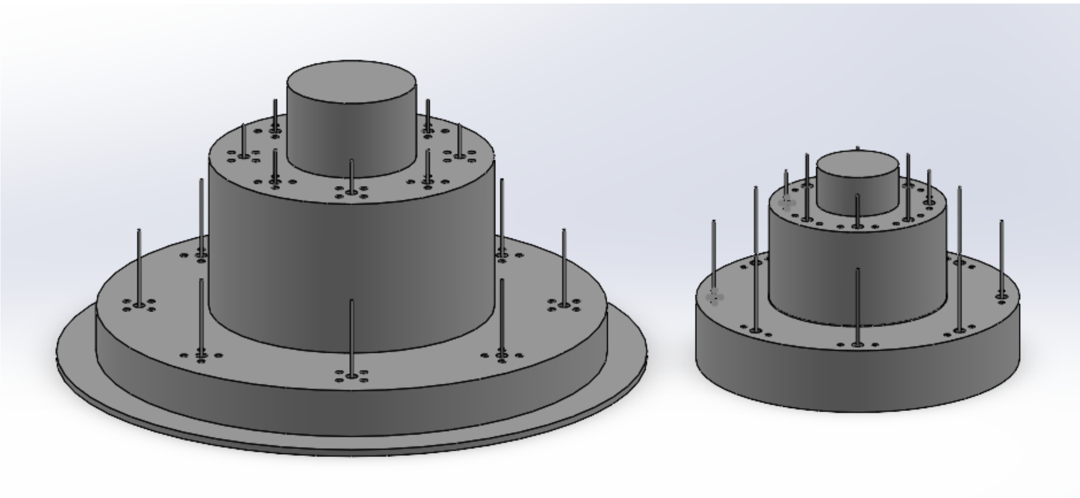

Figure 6.3: Antenna obtained by superposing two hat antennas with a scaling factor of 2: The cake antenna. The two model are shown. On the left: Initial cake antenna; On the right: Smaller cake antenna that was manufactured and tested.

different parameters. The results of these sweeps is shown in appendix A. Then, we select a point that maximizes the sum of the two gains (the factor G of equation 4.7).

Finally, we perform local optimization to find the local maxima of the global antenna gain G. The radiation pattern after optimization in the azimuthal plane is shown in figure 6.4.

However, the large dimension of the antenna makes it hard to manufacture on a normal lathe. Therefore, we modify the model and limit the largest radius. After a second optimization, we obtain the following radiation pattern (see figure 6.5). We see that the directivity is reduced of 2 dB and 2.5 dB for the fundamental and harmonic antenna respectively. Nevertheless, its smaller dimension makes it much easier to manufacture.

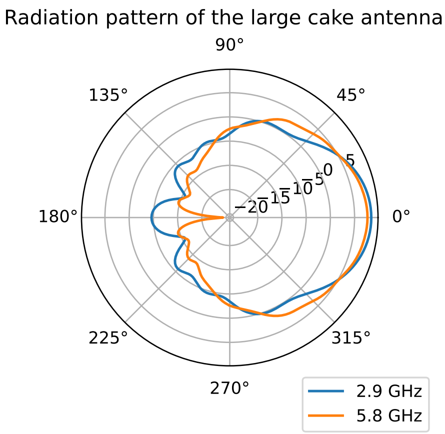

	Directivity [dB]
2.9 GHz	8.45
5.8 GHz	7.67

Figure 6.4: Directivity of the large cake antennas. The fundamental antenna is simulated at 2.9 GHz and the harmonic antenna at 5.8 GHz.

The realized gain was also given in figure 6.5. It correspond to the gain of the antenna considering impedance mismatch. We observe a large gain reduction for the fundamental antenna and a smaller one for the harmonic antenna. This is because the matching of the harmonic antenna is better. We see that if we want to obtain the best performances (as close as the directivity as possible), a matching circuit is required for at least the fundamental antenna.

6.2.2 Impedance at the disconnected elements

A critical design choice is the RF switches. RF switches can be divided into two group the reflective and absorptive switches. These groups differs by the impedance of the switch when in the OFF state: an open/short and a match for the reflective and absorptive switch respectively.

This choice is important because the radiation pattern changes depending on the switch type. From simulations, the highest gain is obtained for an open impedance at the unused SMA port compared to a matched impedance.

This means that the coupling between the different monopoles is contributing to the global gain.

6.3 Antenna prototype

In this section, we will present the prototype of the cake antenna.

The ground plane is first manufactured using a lathe. All the holes are then drilled and some are tapped to allow the monopoles to be screwed on the ground plane.

Then, the monopoles are build using straight panel mount SMA connectors and ϕ1mm copper wire. The copper wire is cut at the correct length, the insulation layer is removed using sandpaper and the wire is placed in the connector receptacle. The resulting monopoles are shown in figure 6.6a.

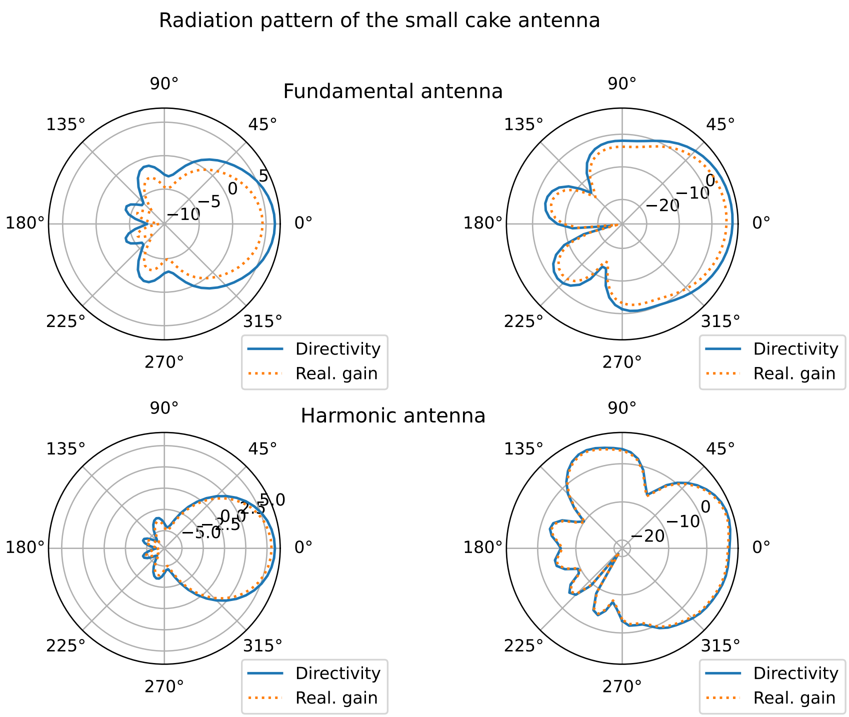

	Directivity [dB]	Real. gain [dB]
2.9 GHz	6.32	4.48
5.8 GHz	5.93	5.53

Figure 6.5: Radiation pattern in term of directivity and realized gain of the cake antenna. It is shown for the azimuthal and elevation planes.

Finally the prototype is assembled by screwing the monopoles from the bottom of the ground plane.

We have chosen to only use 6 monopoles (3 for each antenna) instead of 16 to simplify the manufacture. A minimum number of 3 monopoles instead of 1 was chosen at each frequency such that some coupling effects remains. The measurements of the prototype will be compared with a new simulation that has only 6 monopoles.

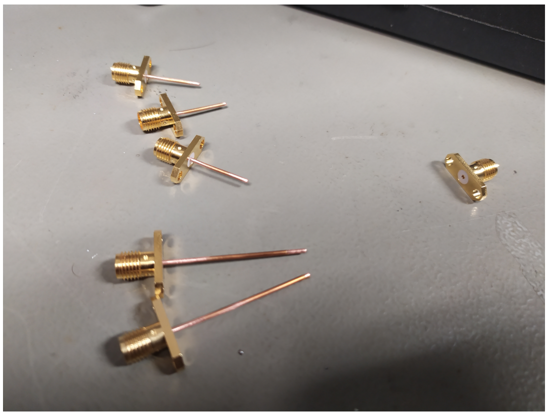

(a) Monopoles of the protoype built from a SMA connector (shown on the right) and a $\phi 1$ mm copper wire. The length of the exposed copper wire is a quarter wavelength at the frequency of interest plus 4mm (thickness of the aluminum).

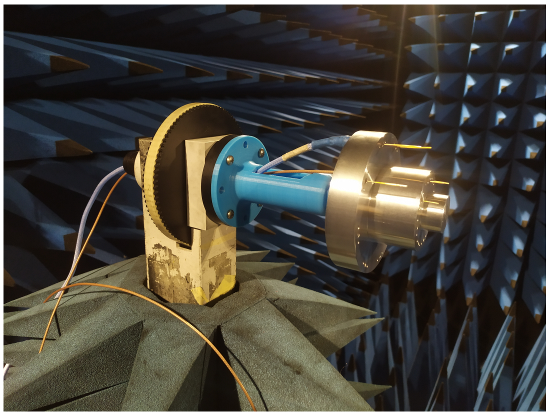

(b) Final prototype of the cake antenna placed in an anechoic chamber.

Figure 6.6

Chapter 7

Results and measurements

In this section, we will characterize the figure of merits (FOMs) of the RADAR circuit and antennas. From this characterization, we will then evaluate the performances of the radar with respect to the application and orientate future developments.

This section is divided into 4 parts. First the 3 part of the system developed in this work (The transmitter, the receiver and the antenna) are characterized. Then a link budget is performed and the maximum range of the system is deduced.

7.1 Characterization of the transmitter

The first characterization we will perform concerns the transmitter (TX). This part of the system amplifies a signal coming from a signal source to a high power. The main figures of merit of the TX is the gain, the maximum output power and harmonic distortion.

The 1 dB compression point (OP1dB) gives an idea of the maximum allowable power before reaching the non-linear region of the amplifiers. The harmonic distortion is the result of the amplifiers non-linearities. Non-ideal power is generated at the harmonics of the input signal. In an harmonic RADAR, this harmonic power can disrupt the system operations.

Indeed, the main argument of using an harmonic radar over a traditional radar to track very small targets is that the receiver is insensitive to the transmitted signal. Then, the reflections on non-target object does not mask the target signal. We can easily understand that if the emitted signal contains power at the received signal frequencies, this principle is disrupted.

7.1.1 S-parameters

S-parameters are a powerful tools to characterize the behavior of RF circuits. Indeed, quantities used for low frequency circuits such as voltage and current are difficult to measure when the wavelength becomes comparable with the circuit length. It is defined as a ratio between pseudo-power waves that propagate between ports.

The instrument used to measure these power ratios is called a Vector Network Analyzer (VNA). It uses couplers to measure the waves propagating in the forward and backward direction at the ports of the circuit. Then the coefficient between transmitted and reflected power at each and between ports can be obtained.

One of the main concept for the practical use of a VNA is the calibration. Without calibration, the results obtained from a VNA do not have a physical meaning. Indeed, the different non-idealities prevents from obtaining the real S-parameters.

The calibration is a procedure designed to estimate these non-idealities and remove their effect from the measurements. This calibration is defined between two reference planes (in the case of a two ports VNA). After correction, a calibrated VNA behaves as an ideal VNA up to these two reference planes and the measured S-parameters describes only the elements that are present between them.

In the case where the reference planes are not directly located at the DUT port, so called deembedding can be performed. Deembedding changes the locations of the reference planes by mathematically removing the effects of the components placed between the calibration reference plane and the wanted reference plane.

Setup

The instrument used is an Anritsu MS4644b VNA. The devices under test (DUT) are placed on the XM-board and XM-probes (coaxial-CPWG fixtures) are used to connect the DUTs to coaxial cables. The active elements are supplied by individual voltage regulators placed under the board as described in section 5.1.3. The VNA calibration was done using an Anritsu coaxial SOLT calibration kit.

In practice, 401 frequency points are measured between 10MHz and 15GHz and an IFBW[1] of 300 Hz is used.

Methodology

A frequency sweep is performed from 10MHz to 15GHz and the S-parameters are measured. The test setup and different reference planes are shown in figure 7.1. As the DUT ports are defined in coplanar waveguide and not in coaxial cable, fixture deembedding[2] must be performed to bring the reference planes to the DUT ports.

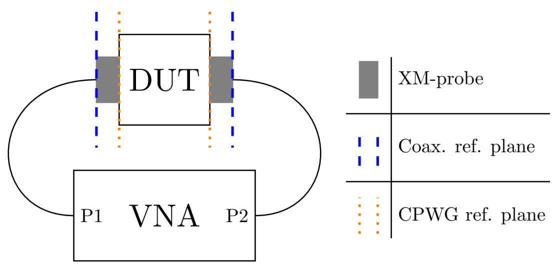

Figure 7.1: Setup for measuring the different XM blocks. The reference planes before and after deembedding of the XM-probe are shown in dashed and dotted line respectively.

At this end, the s-parameters of the XM-probe are required. We can perform network extraction to obtain them. The VNA contains an utility to easily obtain the S-parameters of a fixture from 2 one port calibrations at each pair of reference planes under the assumption that the fixture is symmetrical. The results from this procedure is shown in figure 7.2. We observe that the insertion loss (IL) of the probe is in fraction of dB and

[1]Intermediate frequency bandwidth = resolution bandwidth

[2]Deembedding is the mathematical equivalent of removing the fixture and allows to isolate the DUT scattering parameters from the test setup.

that the reflection coefficient is below -20dB over the whole bandwidth, meaning that these fixtures have good performances.

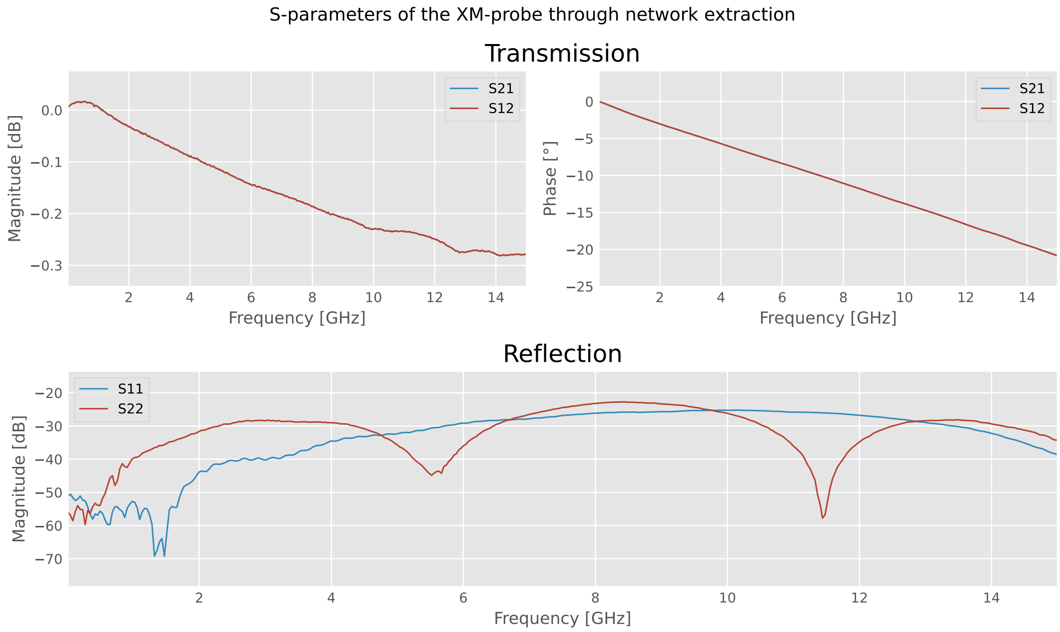

Figure 7.2: S-parameters of the XM-probe between 10MHz and 15GHz

The probes at each port are then deembedded from the measurements to obtain results closer to the real performances of the DUT. In the case were the output power of the DUT (measurement of the complete TX) is close to the maximum input power of the VNA (28 dBm), a coaxial attenuator is added to avoid compression and damage to the VNA. It is then deembedded from the measurements using s-parameter obtained from a direct measurement of the attenuator. Note that an external DC blocks are not required because all the active DUTs have integrated DC block (series capacitor) in the signal path.

Results

The complete TX circuit is depicted in figure 7.3. It contains 2 amplifiers (A114 & A5T5), a 3dB power divider, a low pass filter (LPF) and a frequency doubler (f x 2). These blocks are connected using jumpers as described in section 5.1.3 and XM-probes are used on the IN and TX ports. The output of the frequency doubler is loaded by a matched load to avoid reflections.

The most important blocks of the TX is the amplifiers. The s-parameters of the TX amplifiers are given in figure 7.4. The gains of the A114 and A5T5 around 2.95 GHz (Fundamental band) are 18.01dB and 13.18dB respectively. This bring the total amplification of the transmitter to 31.19dB. This amplification does not take into account the ILs of the passive elements. It is therefore an upper bound on the total amplification capabilities of the TX.

We can measure the S-parameters between the TX ports (see figure 7.3) to obtain the true amplification. For this measurement, we apply deembedding only on the IN fixture. This choice of reference planes is closer to the actual use as the input signal is

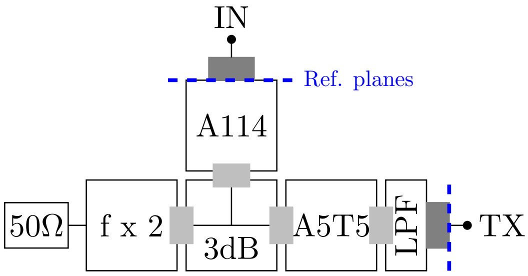

Figure 7.3: Isolated TX of the RADAR. The output of the frequency doubler (f x 2) is loaded to prevent reflection. The other ports are connected using XM-probes and adjacent blocks are connected using GSG jumpers. The reference plane are defined in CPWG (IN port) and coaxial waveguide (TX port).

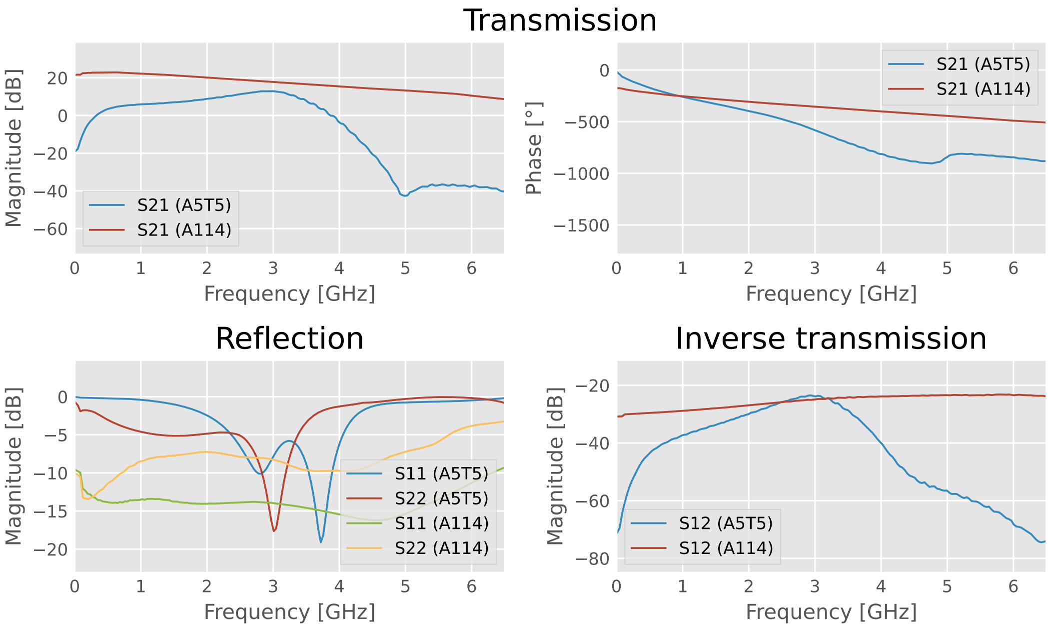

Figure 7.4: S-parameters of the 2 amplifiers of the TX. The fixture between CPWG and coaxial have been deembed. Port 1 is connected to the input and port 2 to the output.

typically generated on the same PCB as the rest of the RF circuit while the output port is connected to an antenna using a coaxial cable (i.e. need of a fixture to convert CPWG to coax). The total measured amplification at 2.95 GHz is 26.7 dB.

There is therefore a difference of 4.49 dB with the total active amplification of 31.19 dB. We can take a look at the S-parameters provided by Quantum X-microwave for the 3 dB splitter and LPF. The IL for these two elements is 3.86 dB and 0.65 dB respectively for a total of 4.51 dB which is close to the measured value.

Like the amplification in the fundamental band, we can focus on the amplification in the harmonic band (around 5.8GHz). Ideally, we do not want that the transmitter does not emit any power in this band. From the S-parameter, the amplification is around -85 dB.

To assess the consequence on the circuit, we can take an example of a simple signal source. The ROS-3800-119R+ from MiniCircuit is a wideband 1900 to 3700 MHz wideband

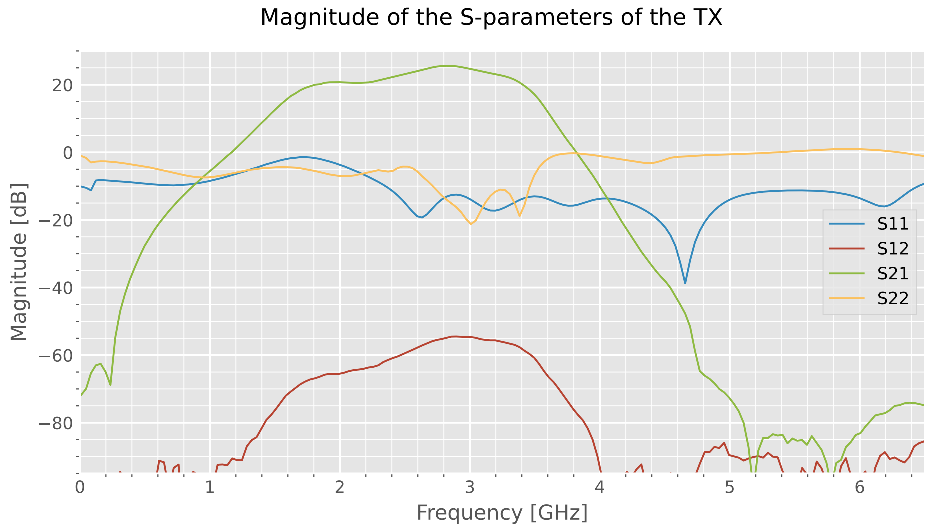

Figure 7.5: S-parameters of the TX. The reference plane at the IN and TX port are defined in CPWG and coax. respectively.

VCO. Around an output frequency of 2900M Hz, its output power is 6.23 dBm and the second harmonic is at -22.4 dBc [24]. The signal power around 5.8GHz is -16.17 dBm. When we apply it on the TX, this power is attenuated and becomes -101.17 dBm at the output.

7.1.2 Gain compression and output power

Amplifiers are non-linear device. Their characteristic depends on their operating conditions. One such example is the gain compression (i.e. the output power saturates when it reach a certain level). One of the main characteristic of a transmitter circuit is the maximum power it can output. Gain compression is therefore an important effect to characterize in the case of the TX.

Setup

The setup for gain compression is essentially the same as scattering parameters measurement (see figure 7.1). The main difference is the configuration of the VNA. Instead of varying the input signal frequency, it now vary its power by stepping the attenuator value. As we are measuring high power signal, the 10dB attenuator is added to all measurements to prevent the VNA from being damaged or VNA compression that could ruin the measurements. The attenuator is directly included in the calibration, therefore, it must not be deembedded[3].

However, the setup is slightly different for the power amplifier (A5T5). Indeed, the input power must be sufficient to put the amplifier in compression. As the maximum output power is insufficient, a preamplifier stage must be added. This modified setup is depicted in figure 7.6.

[3]This improve the measurements compared to deembedding as only the inaccuracies from one calibration are contributing to the measurement error.

The measurement frequency is chosen as 2.95 GHz to be inside the band. The number of points in the power sweep is set to 35.

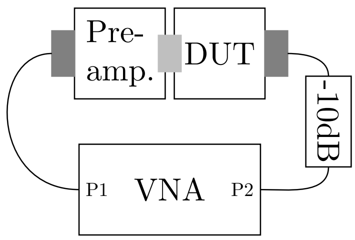

Figure 7.6: Setup used to measure the power characteristic of the A5T5. A preamp (A114) is used to ensure gain compression is reached and a 10 dB attenuator is added to prevent VNA damage and VNA compression. The pre-amp and DUT are connected using a GSG jumper.

Methodology

The range of power is configured based on the amplifier datasheet to ensure it reaches compression.

To move the reference planes to the DUT ports, the gain (insertion loss) of the probe is subtracted from the S21 value in dB[4]. In the case of the preamplifier, the gain values depending on the input signal power are used. The effect of the GSG jumper (lightgrey square) is neglected.

In practice, the A114 is used as a preamplifier. Therefore, the measurement of this amplifier is done before the A5T5 to be able to use the measured values for deembedding. Using the measured values instead of a constant gain should lead to better measurement as the compression of the pre-amplifier is compensated. As the power values are different between the measurement to ensure compression, they are interpolated for deembedding.

The 1dB compression point is then computed as the point where the gain falls 1dB below its level at P_{in} =-30 dBm (At this input power, the amplifier is supposed linear). To find the input power at which it occurs, a binary search with interpolation is used and convergence is verified visually on the plots.

Results

The results of this measurements are shown in figure 7.8. The gain (S21) and the output power are plotted for the 2 amplifiers and the complete TX.

Note that the IC of the A5T5 (ADL5324) incorporates a dynamically adjustable biasing [5]. This allows to dynamically change the current consumed by the amplifier (i.e. 62 mA for 3.3V and 133 mA for 5V). The trade-off concerns the P1dB and OIP3 of the amplifier and is shown in tab. 7.7.

As being able to dynamically change the power consumption of the A5T5 could be interesting in the context of an UAV, the gain compression for the 2 bias voltages was measured by simply changing the voltage regulator supplying the amplifier (using the one for the A2N4).

[4]The assumption is that the losses of passive components is not dependent on power

	3.3V	5V
OP1dB	23.6 dBm	27.8 dBm
OIP3	32.4 dBm	42 dBm

(a) @ 2630 MHz

	3.3V	5V
OP1dB	25 dBm	28.5 dBm
OIP3	29.3 dBm	36.6 dBm

(b) @ 3600 MHz

Figure 7.7: Typical P1dB and OIP3 of the ADL5324 for different bias voltage. The values are taken for the two bands closest to this work fundamental frequency band.

A table shown in figure 7.8 summarizes the different input and output power at the 1dB compression point. The A114 is the first block at the input of the TX. If we take a look at the IP1dB of the TX and A114, we see that the TX reach 1dB compression 3 dB lower than the A114. Therefore, the A114 in the TX circuit does not reach compression even when the whole TX is.

If we compare the OP1dB of the A5T5 and TX biased at 5V, we observe a difference of 0.15 dB. This is expected as only the A5T5 is in compression (see before) and the output power essentially depends on the amplifiers that have reached compression. The observed difference can be attributed to the ILs of the TX and probe. However, from the LPF specifications, the difference should be around 0.6 dB instead of 0.15 dB. When we do the same for a bias of 3V, we obtain a difference of 1.4 dB which is greater than expected. This could mean that the measurements are imprecise. Another explanation is that this behavior is caused by the bias voltage that is slightly too low (3V instead of 3.3V). This could lead to the unexpected behavior we observe.

More measurements using a dedicated LDO that provides the right voltage is therefore needed to better assess the amplifier behavior relating to the bias voltage.

Finally, we can compare the measurements with the values from the datasheet (see figure 7.7). The measured OP1dB is 27.5 and 26 dBm for 5V and 3V respectively. We see that these values are relatively close to the one in table 7.7.

We can conclude that the maximum power of the TX is around 27 dBm or 0.5 W.

7.1.3 Power of the harmonics of the transmitted signal

With the S-parameters, we have quantified the linear behavior of the TX. However, the amplifiers are non-linear devices. To reach a high power, the power amplifier (A5T5) must be operated near compression. In this operation region, the signal distortions become more important and less negligible.

In the context of this application, the most important distortion is the generation of the signal harmonics. Indeed, in a harmonic radar, the receiver is made sensitive specifically to the second harmonic. Quantifying the amount of power emitted by the TX in the harmonic band is therefore an important figure of merit.

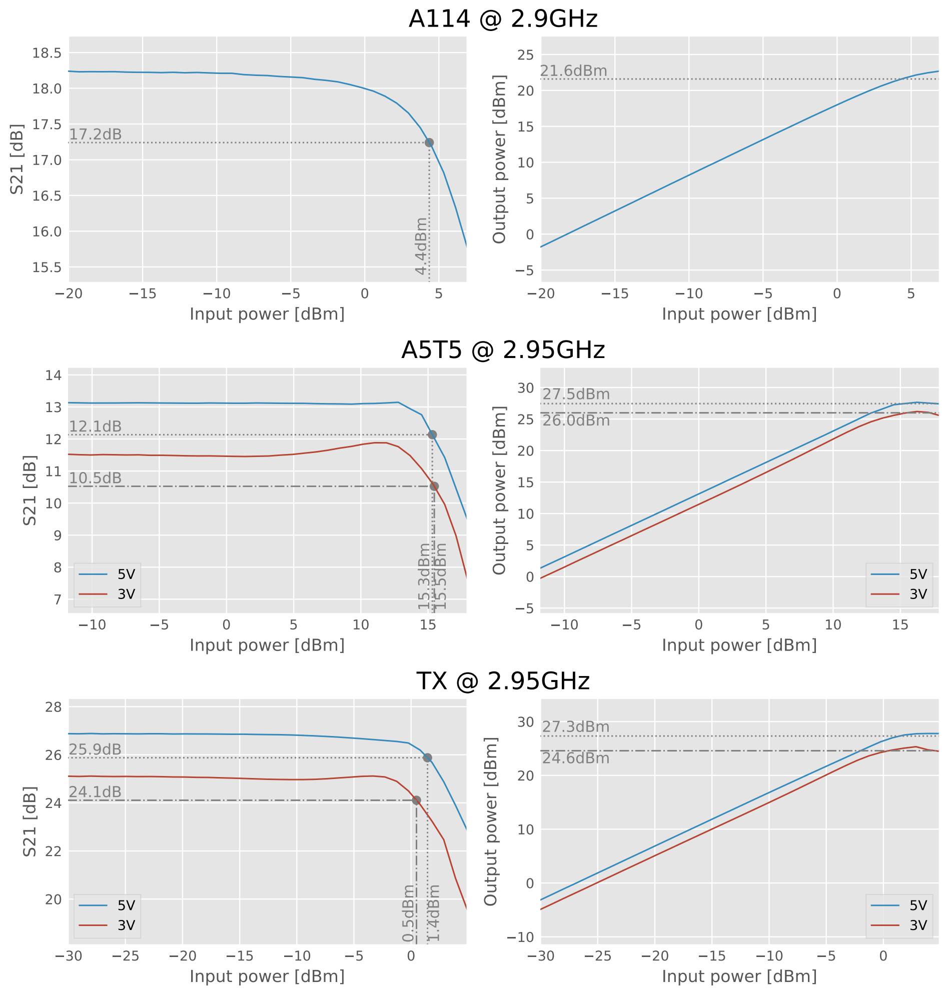

	IP1dB [dBm]	OP1dB [dBm]
A114@2.9GHz	4.352	21.592
A5T5(5V)@2.95GHz	15.320	27.455
A5T5(3V)@2.95GHz	15.465	25.989
TX(5V)@2.95GHz	1.438	27.314
TX(3V)@2.95GHz	0.473	24.581

Figure 7.8: Power sweep of the TX amplifier and complete TX circuit. The 1dB compression point is defined with respect to the gain at low power (-30 dBm).

Setup

For this measurement, we use a signal analyzer[5] (SA) and a signal generator[6] (SG). The test setup is depicted in figure 7.9. A signal in the fundamental band (i.e. 2.95 GHz) is applied on the IN port of the TX and the output is measured. A coaxial matched load is connected to the LO port to prevent reflection.

Coaxial cables are used to connect the instruments (SG and SA) to the circuit.

[5]Keysight N9042B 50 GHz Signal Analyzer

[6]Keysight N5183B MXG X-Series

To have a good resolution with reasonable measurement time, the span measured must be limited around the frequency of interest. We choose a resolution bandwidth of 10 Hz and a span of 5 kHz.

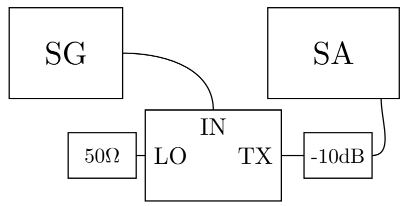

Figure 7.9: Setup used to measured the harmonic distortion of the TX. A signal generator (SA) is used to provide the input signal and a signal analyzer (SA) measures the output spectrum. A load is connected to the LO port to prevent reflections and a 10 dB attenuator is added in the signal path to protect the SA and avoid compression. The reference planes are defined as in the S-parameters measurements.

Methodology

The signal analyzer measures the spectrum at the TX port. Then, the power of the harmonic is computed from the spectrum as the integral of the spectrum (in the linear domain) over a small bandwidth around the harmonic frequency.

As the signal generator is not ideal and produce harmonic distortion, we evaluate its impact on the final measurement to ensure that the obtained FoMs mainly characterize the DUT and not the SG. From the signal generator technical specifications, we get a lower bound of the harmonic distortion. For an output power of 10 dBm and frequencies between 2 GHz and 5 GHz, the 2nd harmonic power stays below -70 dBc [13]. We can then suppose that for an output power of 1.5 dBm, the 2nd harmonic power is below -68.5 dBm. Using the amplification of the TX for the 2nd harmonic band (-85 dB), we get an increase of power of -153.5 dBm which is negligible. Therefore, we can suppose that the harmonic distortions measured are only caused by the TX non-linearities.

The cables linking the DUT and the SA/SG are lossy and an attenuator is placed before the SA input to protect it and prevent SA compression. Therefore, precaution must be taken when taking the measurements. First, the cable loss to the input of the DUT must be compensated to ensure that it is driven at the correct level. Using the transmission coefficient of the cable at 2.95 GHz (from s-parameters), the signal generator is set to 2 dBm instead of 1.5 dBm to compensate the 0.5 dB loss. Secondly, the cable loss and from the DUT to the input of the SA (evaluated from S-parameters measurements) and attenuator loss are removed from the measurements in post-processing.

Results

The spectrums at the fundamental and harmonic frequency (2.95GHz and 5.9 GHz) for 2 different TX configuration (With and without output LPF) are depicted in figure 7.10. The spectrum were evaluated for 2 input power to assess the effect of gain compression on harmonic distortion. The chosen power is 2 dBm and 0 dBm at the signal generator. Due to the cable losses, the true power applied on the TX is 1.52 dBm and -0.48 dBm. The two configuration are therefore above and below 1 dB compression (see section 7.1.2).

We see that the TX with the LPF has an harmonic distortion of around -83 dBc and -85 dBc for the low and high input power respectively. When we remove the LPF, this distortion raise up to -44.8 dBc and -43.977 dBc respectively. The improvement due to the LPF can be quantified as approximately 40 dB at the cost of a reduction of power (due to LPF IL).

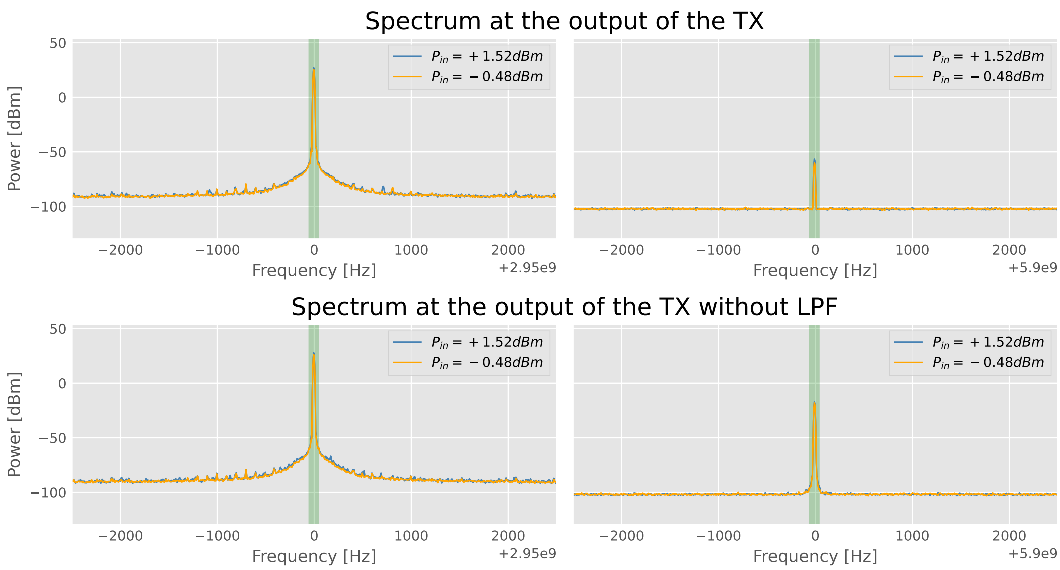

Integrated power (BW=100 Hz) with LPF

	P [dBm] @ 2.95 GHz	P [dBm] @ 5.9 GHz	Ratio [dBc]
$P_{in} = +1.52dBm$	30.294	-53.121	-83.415
$P_{in} = -0.48dBm$	28.613	-56.471	-85.084

Integrated power (BW=100 Hz) without LPF

	P [dBm] @ 2.95 GHz	P [dBm] @ 5.9 GHz	Ratio [dBc]
$P_{in} = +1.52dBm$	31.092	-13.750	-44.843
$P_{in} = -0.48dBm$	29.371	-14.606	-43.977

Maximum power [dBm]

	With LPF		Without LPF	
	@ 2.95GHz	@ 5.9GHz	@ 2.95GHz	@ 5.9GHz
$P_{in} = +1.52dBm$	27.022	-56.594	27.798	-17.262
$P_{in} = -0.48dBm$	25.332	-60.029	26.101	-18.104

Figure 7.10: Spectrum of the TX at the fundamental and harmonic frequency for 4 configuration. The bandwidth used for the integrated power method is highlighted in green.

From the spectrum measurements, we can also notice the presence of phase noise. This could be an interesting characteristic to know about a FMCW RADAR as it could lead to a reduction in performance [29]. In a harmonic radar, due to frequency conversion, the phase noise is increased by a factor of $\sqrt{n}$ (in the ideal case) with n being the harmonic used in the receiver (2 in this work). Therefore, the phase noise of the emitted signal must be known precisely and the effect of frequency conversion must be known.

However, the output signal phase noise mainly depends on the one of the input signal. As we do not use a dedicated signal source, it would not make sense to characterize this distortion at this stage.

7.1.4 LO power

The last measurement on the TX we will perform concerns the LO power. From figure 7.3, the input signal is amplified and fed to a frequency doubler.

In the complete circuit, this signal is then fed to the mixer. From its datasheet, the mixer reaches a minimal conversion loss of 6.26 dB for a LO power of 4 dBm [23].

Setup and methodology

The setup and methodology are essentially the same as the one used in harmonics measurements. The only difference is that we only look at the maximum power instead of the integrated power over a small bandwidth.

Results

The power spectrum as well as the maximum power of each curves is shown in figure 7.11. We obverse that when we use an input power of 1.52 dBm (TX at 1dB compression), the LO power only reaches 3.5 dBm and not 4 dBm. We then expect a mixer conversion loss lower than 6.26 dBm. Note that the amplifier between the input port and LO port (A114) is not in compression. This means that we can use a different power divider or a small attenuator in the IN->TX branch to drive the A114 at a higher power to reach the desired LO power.

From previous measurements, we can estimate the expected power of the LO. At 2.95GHz, the A114 has a gain of 18dB and, from its datasheet[21], the coupler has an insertion loss of 3.8dB. Using the conversion loss provided in the datasheet[22] of the frequency multiplier (12.1dB at an input power of 17 dBm), we obtain an expected LO power of 3.62 dBm which is quite close to the one measured.

We also measured the LO power for another drive power. We see that while the input power is reduced by 2 dB, the obtained LO power is reduced by around 2.1 dB. This additional loss is caused by the fact that we approach the minimum drive power of the multiplier (13 dB). Similarly, the multiplier is rated only for input power up to 17 dBm which correspond to an LO power of around 5 dBm. This value is sufficient for driving the mixer and the current multiplier does not have to be changed.

We also measures the unwanted fundamental component of the frequency double signal. The so-called fundamental isolation is then around 25.6 dBc. As the mixer that is used is wide band (2800-8000 MHz), this non-ideal fundamental signal create additional mixing products that can disrupt the receiver operations. If we want to improve this non-ideal isolation, we can simply add a HPF after the frequency doubler at the cost of an additional insertion loss.

7.2 Characterization of the receiver

The receiver is the second part of the RF circuit. Its main figure of merit are its gain/conversion loss, noise figure and isolation.

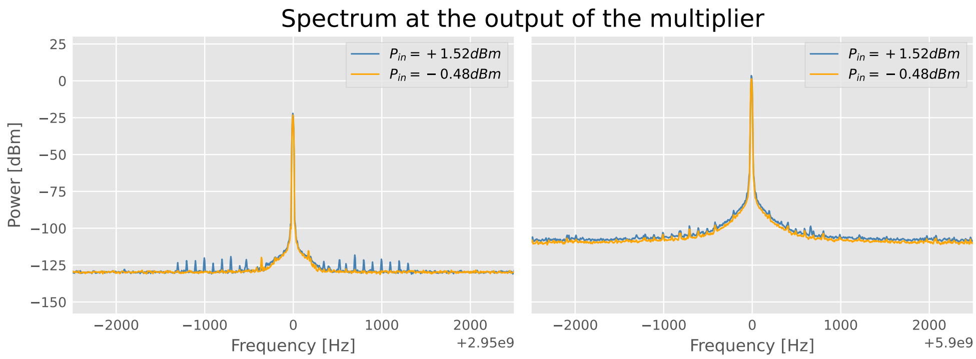

Output powers

	P_{out} [dBm] @ 2.95 GHz	P_{out} [dBm] @ 5.9 GHz
$P_{in} = +1.52dBm$	-22.091	3.531
$P_{in} = -0.48dBm$	-23.245	1.410

Figure 7.11: Power spectrums at the LO port of the TX around the fundamental (2.95 GHz) and harmonic frequency (5.9 GHz)

The gain is important to bring the amplitude of the signal inside the range allowed by the ADC.

The noise figure characterize the relation between the SNR of the input and output signals. As said before, the SNR threshold of the parameter estimation method used specify the SNR required to obtain correct performances. This allows to estimate the required input SNR from this specification.

Finally, the isolation describes how the LO signal leak to the RF and IF ports of the receiver. This leakage can have an important impact on the system. Power at the harmonic frequency can leak and be reemitted by the antenna. This leads to the same problem as the TX harmonic distortions. Power leaking from the LO port to the IF port can cause distortion as well as saturate the ADC.

7.2.1 S-parameters and conversion loss

S-parameters are also useful to characterize the behavior of the receiver. They can be defined even though frequency conversion is performed inside the DUT (such as for a mixer). However, to be able to measure them, the VNA must be equipped with two sources (in the case of a two port VNA) that can be independently set at different frequencies. The Anritsu MS4644b is only able to do this if an option is enabled (Multiple source control). As the one that was used in this work is not equipped with this option, it is unable to perform these measurements.

Nevertheless, measurements using a signal generator and spectrum analyzer were performed to get the receiver performance for a frequency. In the case of the amplifier, as they do not include frequency conversion, they can be directly measured using a simple VNA.

Setup

The setup used to perform S-parameters measurements is the same as the one used in section 7.1.1.

For the conversion loss measurements, two signal generator were used to produce the two input signal (LO and RF signals). The setup is shown in figure 7.12. The TX is used to drive the LO port. The conversion loss can then be given in term of TX input power.

Filters are added to the input and output of the filters to remove out of band noise and better discriminate the output signal.

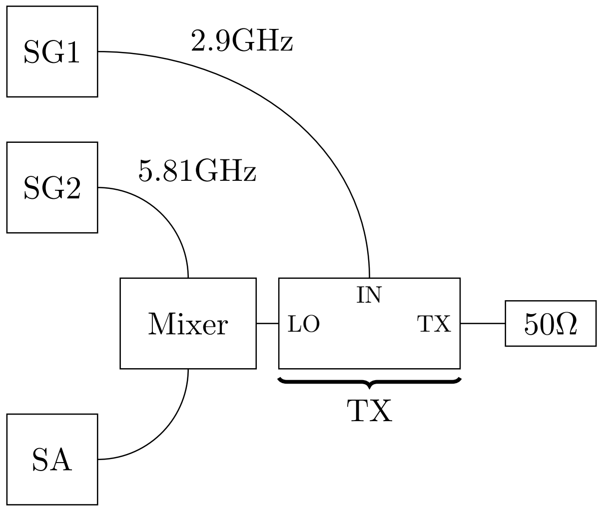

Figure 7.12: Setup used to measure the conversion loss of the mixer. The 2 input signals (RF and LO) are generated using two un-synchronized signal generator and the output is measured using a signal analyzer.

Methodology

First, the power supplied at the TX and RF are estimated by removing the cables and filters losses. For this purpose, the cables and the RX band pass filter insertion loss s-parameters were measured.

Then, the IF power is measured around the estimated IF frequency ($f_{IF} = f_{RF} - 2f_{LO}$). As for the other ports, the cable loss and filter loss are removed. In this case, as the IF frequency is low (5MHz and 10MHz), the s-parameter can not be measured by the Anritsu MS4644b VNA. Therefore, the insertion loss of the filter was taken from the datasheet and the cable insertion loss was taken as the lowest measured S21 from the VNA (10MHz).

Results

Multiple measurements were done to observe the dependance of the conversion loss on LO power and IF frequency. They are summarized in figure 7.13. We see that the mixer achieves a lower conversion loss than expected.

We can also see that the conversion loss decrease with the LO power as it comes near the optimal LO power of 4 dBm.

The S-parameters of the 2 amplifiers of the receiver chain are given in figure 7.14. Additionally, their values at 5.9 GHz is given in table 7.1.

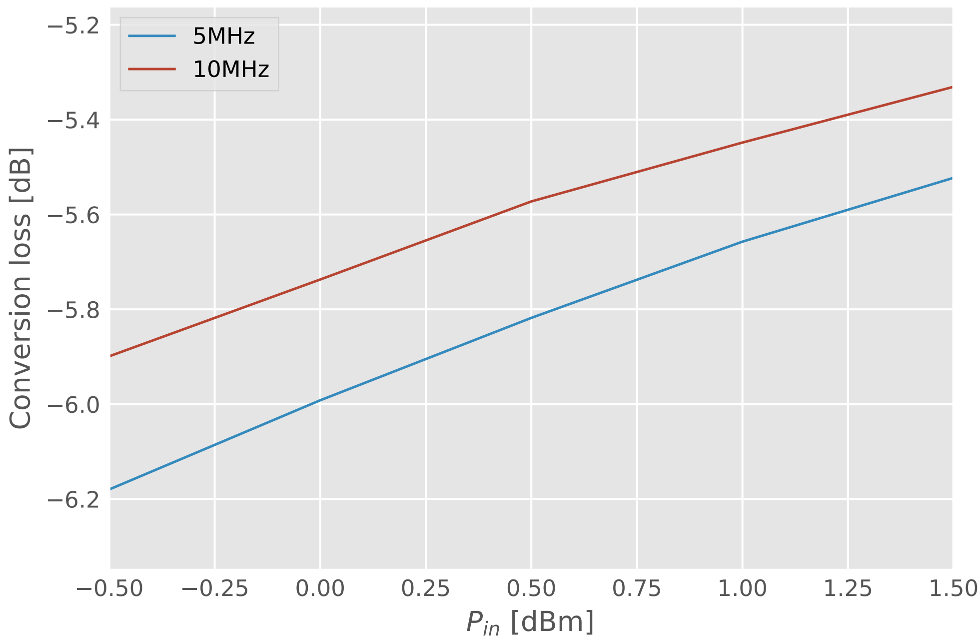

Figure 7.13: Conversion losses of the mixer for two IF frequencies. The power at the IN port of the TX was swept from -0.5 dBm to 1.5 dBm (corresponding to an LO power ranging approximately from 0.5 dBm to 3.5 dBm).

First, we will take a look at the D2B4. It is a wideband amplifier that has a moderate gain over a large bandwidth from 50 MHz to 6GHz. We see that the S-parameters correspond exactly to this description. The gain over the whole bandwidth is approximately 14 dB and a matching of -10 dB.

Now we take a look at the low noise amplifier (A2N4). We notice that, when compared to the S-parameters provided by the supplier, the gain saturates at low frequency. This is caused by gain compression. Indeed, the excitation power was set to 0 dBm and the saturated power of the A2N4 is approximately 20.5 (from the datasheet[20]).

First, we see that the gain at low frequencies is very high (up to 26 dB). It then falls down as the frequency increase. It reach the following point: 20 dB at 1 GHz, 10 dB at 4.5 GHz and 0 dB at 8.5 GHz.

Another important characteristic is the unidirectionality of the amplifiers. It is especially important for amplifiers that are on the RF side of the receiver. A good unidirectionality prevent the LO-RF leakage from reaching the antenna and being reemitted. Similarly, the reflection coefficient of second port indicates the amount of LO-RF leakage that is reflected back to the mixer.

	S_{21} [dB]	$S_{12}[dB]$	S_{11} [dB]	S_{22} [dB]
A2N4	7.18	-16.55	-10.84	-12.1
D2B3	12.57	-18.38	-11.33	-17.6

Table 7.1: S-parameters of the RX amplifier at 5.9GHz.

Figure 7.14: S-parameters of the two TX amplifiers. We see that the A2N4 reach compression for low frequencies (Compared to the s-parameters provided by the supplier). Port 1 correspond to the input of the amplifiers and port 2 to their output.

7.2.2 Noise figure

The noise figure of a circuit describes the relation between the input SNR and output SNR. Multiple techniques can be used to measure this figure of merit. The one used in this work is the Y-factor method (see figure7.15). This method consists in measuring the output power for 2 temperatures of input noise. From these 2 measurements, the noise figure is estimated by computing the value of input temperature for which the output temperature is zero. Additionally, the gain of the DUT is deduced from the slope of the line. As seen on the graph, the y-factor is based on the assumption that the DUT behaves linearly with respect to the input noise power. The noise figure of an amplifier in gain compression can therefore not be performed using this method.

Setup

For this measurement, we use a SA[7] and a noise source[8]. The noise source and SA are connected through USB such that the noise figure utility can control the state of the noise source. The DUT input is then connected to the noise source and its output to the SA.

Additionally, a calibration of the noise source is needed. The cables and connector used during this calibration should be similar to the one used in during the measurements. At this end, the cable connecting the noise source and SA (cal.) is composed of the 2 cables at each end of the DUT (meas.) with an additional female-female SMA adapter.

The setup is depicted in figure 7.16. The measurement are performed for 2 different frequency range. The first one is a low frequency band starting at 500MHz (lowest frequency of the noise source) to characterize the behaviors of the amplifiers in IF. The second one us centered around 5.9 GHz to measure the behavior of the amplifier in RF. In both cases, the number of frequency points measured is 11 and The measurement spans

[7]Keysight N9042B 50 GHz Signal Analyzer

[8]Keysight U1833D USB Smart Noise Source500 MHz to 60 GHz

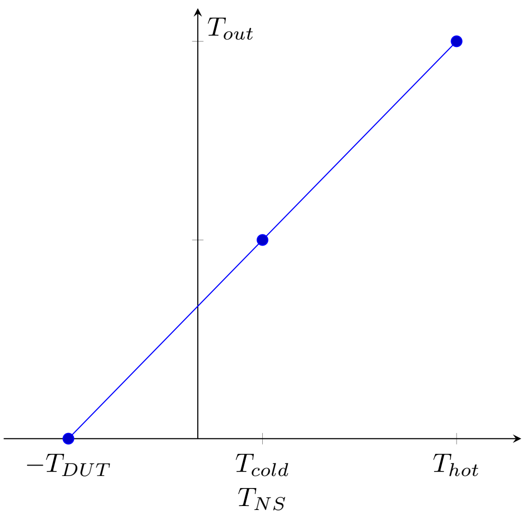

Figure 7.15: Illustration of the y factor method. The noise temperature of the DUT (T_{DUT}) is deduced from two measurement of the output noise power (T_{out}) at different input noise temperature (T_{hot} and T_{cold}). The slope of the line also estimate the gain of the DUT.

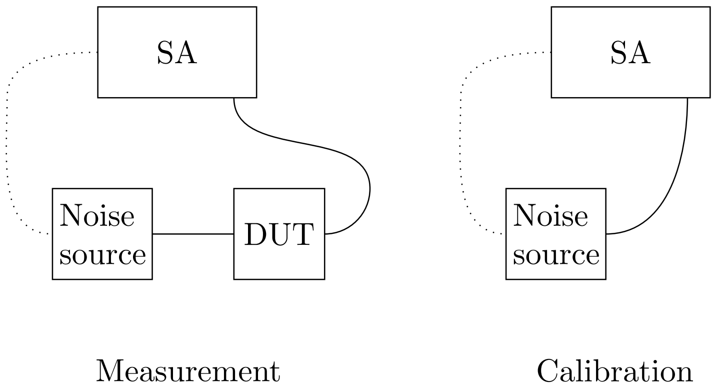

Figure 7.16: Setup used to measure the noise figure of the RX amplifiers using the Y-factor method.

are 100MHz and 300MHz and the RBWs[9] are 300kHz and 4MHz respectively. 300KHz and 4 MHz.

Methodology

First a calibration of the noise source is performed and effects of the cables are removed. However, an adapter was used during calibration and XM-probes are used to connect the CPWG DUT to the coaxial cables. This means that their are not accounted for. Ideally, the probes should be removed from the measurement while the adapter should be added. Therefore, as their attenuation is in the order of fraction of dB (0.1 dB) and that their effects on the measurements are opposite, we will neglect the insertion losses of the

[9]The resolution bandwidth is the bandwidth over which the power is measured at each frequency point.

adapter and probes.

An average of 10 sweep is also performed to attenuate the noise randomness.

Results

The noise figures and gains of the two RX amplifiers are shown in figure 7.17. The means of the two figures of merit in the two evaluated bandwidth are shown in the table below.

We see that the low noise amplifier (A2N4) has a lower NF in the two frequency bands. However, its gain falls drastically at the high frequencies.

The second amplifier (D2B4) has more constant characteristics. Its NF and gain is around 3.5 dB and 14 dB respectively.

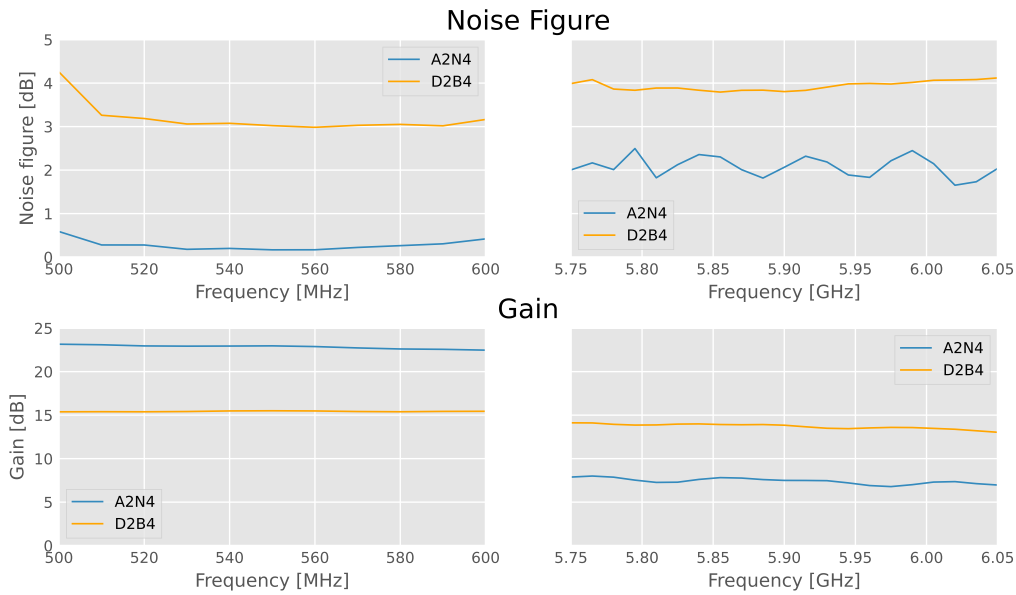

	A2N4		D2B4	
	@ 550 MHz	@ 5.95 GHz	@ 550 MHz	@ 5.95 GHz
mean NF [dB]	0.28	2.08	3.19	3.94
mean Gain [dB]	22.84	7.42	15.43	13.71

Figure 7.17: Results of the Y-factor method on the two RX amplifiers. It is measured inside 2 frequency bands that correspond to the LO and RF side of the mixer.

Knowing these characteristic, we can evaluate the performance of multiple configuration of the receiver. Indeed, we can deduce the noise factor (noise figure in linear domain) of a chain of devices from their NF and gain. For a chain of n devices, we write $F_i = 10^{NF_i/10}$ and G_i, the noise factor and gain of the ith device with i=1,...,n (1 is the closest to the input and n is closest to the output). The noise factor of the whole chain F is then given by eq. 7.1 with the gain expressed in the linear domain.

$$F = F_1 + \frac{F_2 - 1}{G_1} + \frac{F_3 - 1}{G_1 G_2} + \cdots + \frac{F_n - 1}{G_1 G_2 \cdots G_{n-1}} \tag{7.1}$$

Therefore, to estimate the NF of the RX, we need to know the characteristics of all the elements. In the case of a passive device, the NF is equal to the device insertion loss if its physical temperature is equal to the reference temperature.

The mixer NF can be measured with the Y-factor configured for frequency conversion DUT. The LO is then supplied with a signal generator and the NF is measured with the noise source at the RF port and the SA at the IF port. Unfortunately, the results obtained from these measurements were completely incompatible with previous measurements. Indeed, the resulting conversion loss and NF were both approximately 3 dB better than the expected values. Multiple configuration were used with RF filtering and pre-amplifier to obtain better measurements. Therefore, we will consider the mixer as a passive circuit and use a NF equal to the conversion loss.

We will consider multiple configurations: the intended configuration, the modified configuration, the actual configuration and the upgraded configuration. These configuration are shown in figure 7.18 and the resulting NF and gain is shown in table 7.2.

From the NF formula (see eq. 7.1), the NF has a lower bound equal to the NF of the first block. In this case, this lower bound is equal to 1.85 dB (IL of the band pass filter). We also see that the gain of a block reduces the impact of the NF of all subsequent blocks.

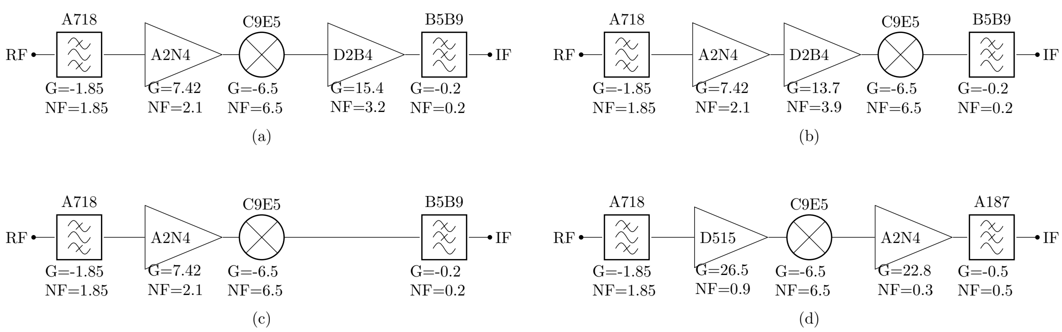

Figure 7.18: Different configuration of the receiver considered. From (a) to (d): intended, modified, actual, upgraded. The gain and noise figure are given in dB.

	Gain [dB]	Noise figure [dB]
Intended (a)	14.27	6.81
Modified (b)	12.57	4.67
Actual (c)	-1.13	5.44
Upgraded (d)	40.45	2.78

Table 7.2: NF and gain of the receiver chain for 4 different configurations.

In the first configuration, the gain of the LNA (A2N4) is relatively low. This lead to a poor receiver gain and noise figure.

To improve the receiver performance while keeping the same components, we move the IF amplifier (D2B4) before the mixer such that the impact of the mixer NF is reduced.

We see that the NF is improved by 2.14 dB at the cost of a reduction of gain of 1.7 dB. However, as the gain is still high, we can add more amplifiers to improve the gain while having a limited increase of NF.

Unfortunately, in the current prototype, we can not use the D2B4 amplifier as it uses the same voltage regulator as the A5T5 (power amplifier) and only one is available. Then, the actual configuration of the prototype is shown as (c). We see that, as we have removed an amplifier, the noise figure is slightly better. This is expected as the noise figure of the D2B4 is quite high and the gain of the previous blocks is low (around -0.9 dB). Furthermore, in the configuration (a), the reduction in NF thanks to the gain of the D2B4 is only applied on the LPF which has an already low noise figure.

Finally, we will choose a better LNA to improve drastically the NF. We select a LNA that has a gain of 26.5 dB and a NF of 0.9 dB at 6 GHz. Then, we use the A2N4 at the IF side as it has good performances at low frequencies. We also select another LPF that as a cutoff frequency that is more suited to the application. We see that both the gain and noise figure is drastically increased. This configuration is therefore far better than all the other thanks to the new LNA.

We can also consider placing the LNA before the BPF. This would then reduce the NF of the BPF which is the main NF source of the last configuration (1.85 out of 2.78 dB). However, this operation should be done with care. Indeed, in a RADAR, there is some crosstalk between the 2 antennas. This crosstalk at the fundamental frequency can overload the LNA. Later in this work, we will estimate the power received through crosstalk at around 0 dBm. If the gain of the LNA at the fundamental frequency is too high, it will reach compression and prevent the operation of the whole receiver chain.

7.2.3 Mixer isolation

The isolation between the ports of the mixer is not perfect. There is leakage between all the ports of the mixer. In our application, some of

Some power coming from the LO is leaked through the RF port. This power is then reemitted by the antenna or reflected back to the mixer. In both cases, this power can produce a signal that is similar to a strong target that is close to the radar. It can then mask other true targets or limit the maximum possible amplification of the receiver. Similarly, the LO-IF and RF-IF leakage can overload the IF chain if it is strong enough.

Setup

The setup used for the measurements of mixer isolation is depicted in figure 7.19. The LO signal is provided through the TX by a signal generator. The power that is leaked to the IF and RF ports is then measured in succession.

To improve the quality of the measurements, a load should be connected to the port that is not currently being tested. Indeed, this would prevent reflections from the leakage through the other port. In this case, as we do not have a load available for this purpose, the resulting values of isolation should end up being worse than expected.

Another possible measurement setup for mixer isolation is achieved by using a VNA to serves as SG and SA. The isolation will then correspond to the transmission coefficient (S21 and S12).

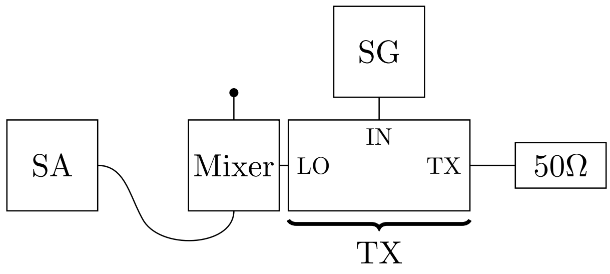

Figure 7.19

Methodology

Similar as other power spectrum measurements, the cable loss is removed based on S-parameters measurements. The LO power is also estimated and the ratio between this power and the maximum leakage power is computed. This gives us the isolation in dBc.

Results

The result of the isolation measurements is given in table 7.3. We see that the values are indeed worse than the typical values from the datasheet[23]. As said before, this can be caused by the reflection of the unloaded port. However, other factors can worsen the measurements. First, the LO power (3.26 dBm) is not the same as the one used in the datasheet (4 dBm) Secondly, this difference in value can be simply explained by device to device variations.

	Isolation (typical) [dBc]
LO-IF	30.03 (33.73)
LO-RF	40.32 (42.78)

Table 7.3: Isolation of the mixer at 5.9 GHz for a LO power of 3.26 dBm. The typical value from the datasheet[23] is also given.

7.3 Antenna

The last part of the radar is the antenna. The main figure of merit of this part is its impedance matching, gain and radiation pattern.

Antennas are not usually perfectly matched at 50Ω. A matching circuit must then be added to obtain the best performance from the antenna. An measurement allows to know the impedance with the goal of designing the matching circuit.

The gain plays a direct role in the link budget. It depends on the shape of the antenna. In direct relation, the radiation pattern gives the gain for multiple directions. These two characteristics must be known to correctly establish the limit in the system in term of range (gain) and tracking capabilities (Width of the main beam).

7.3.1 Impedance and S-parameters

The impedance can be easily measured using a VNA. However, this characteristic depends on the surroundings of the antenna. Therefore, one should match the antenna using the impedance measured in an environment that is similar to the application. As such a test environment is hard to replicate at this stage, we will only characterize the self-impedance of the antenna. To achieve this, we place the antenna in an anechoic chamber such as its surrounding is comprised only of the antenna itself[10].

Another characteristic that can be measured in the same way is the crosstalk between the RX and TX antenna (i.e. the transmission coefficient, S21). This is important to estimate the direct effects of the transmitter on the receiver.

The test setup is depicted in figure 7.20. The antenna is placed in the quiet zone of the anechoic chamber and connected to the VNA using coaxial cables. Note that the reference planes are not at the antenna ports but at the end of short cables for easier access. Their effect will then be mathematically removed using their s-parameters that were measured independently.

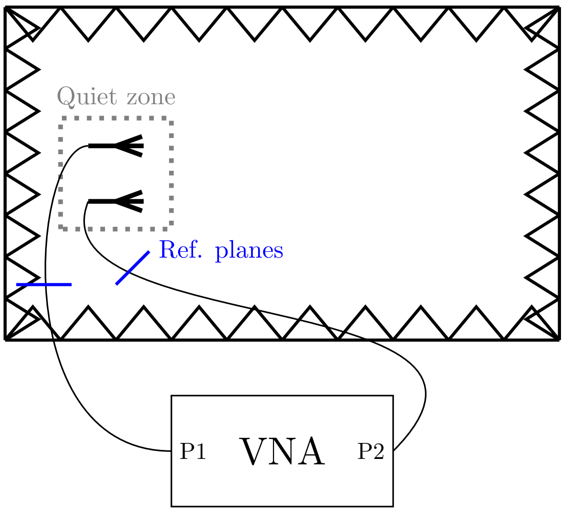

Figure 7.20: Setup for the antenna impedance measurements. The ports of the VNA (P1,P2) are connected to the fundamental and harmonic ports of the antenna respectively

The measured S-parameters are shown in figure 7.21. These measurements were also compared to the S-parameters obtained in CST and seem to match reasonably. We observe that the antenna is not well matched in the fundamental frequency band (around 2.95 GHZ) but well matched in the harmonic band (around 5.9 GHz). A matching circuit is therefore needed to obtain the best performances.

The picture also shows the transmission coefficient between the two antennas. We will now take a look at these coefficient in the two band of interest of our application.

At the fundamental frequency band, the crosstalk between the antennas can overload the receiver. As an example, we consider an emitted power of 27 dBm, the power received

[10] An anechoic chamber only offers an approximation of this environment.

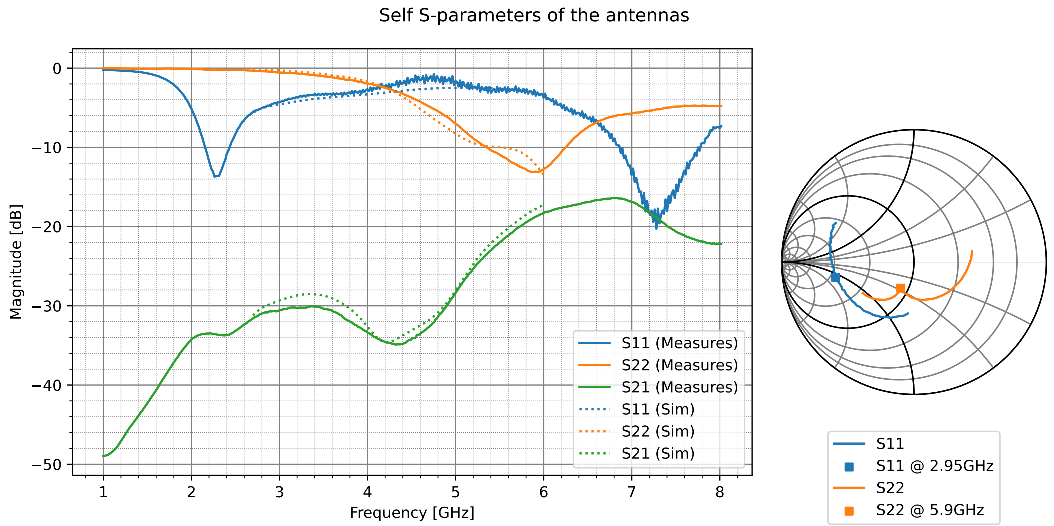

Figure 7.21: Measured scattering parameters of the antennas with the reference planes brought back to the antenna ports . The port 1 correspond to the fundamental port of the antenna (2.9 GHz band) and the port 2 to the harmonic port (5.8 GHz band). These parameters are compared to results of simulation done in CST software between 2.7-6GHz.

by the harmonic antenna is then -3 dBm. In this application, the power of the useful received signal is very small. For a quick order of magnitude, we can consider only the free space path loss. For a target at 3 meters, the path losses at the fundamental and harmonic frequency are around 50 dB and 53 dB respectively. This means that the total path attenuation is around -103 dB. From this, we have to add the conversion losses of the tag and conductor/dielectric losses of all the elements to obtain the real received power. Still, this outlines the need for enough amplification at the receiver.

If the first stage of the receiver is a LNA with an OP1dB of 15dBm, it can have a maximum gain of 18 dB before compression. While one could use amplifiers with greater OP1dB, this solution raises 3 problems. First, the ADC at the end of the reception chain has a maximum input amplitude range, meaning that a too high input signal will be distorted or will damage the ADC. Then, a high power signal will cause enormous losses in each amplifiers, meaning an dramatically increased power consumption. Finally, the amplifiers will have to be bulkier and be equipped with heat dissipation, dramatically increasing the weight of the receiver. To be able to have a greater amplification, the design must include filters that will attenuate the fundamental frequency while minimizing ILs at the harmonic frequency. Band limited amplifiers could also be used, practically working as filters if their reflection coefficient is high enough in the fundamental frequency.

In the harmonic frequency band, the crosstalk between the antennas leads to a false target being detected. Ideally, the transmitted signal does not contain power at the harmonic frequency. However, due to non-linearities in the signal source and transmitter, this is not the case in practice. Considering an harmonic power of -60 dBm such as was measured during the characterization of the TX, the power received by the harmonic antenna is around -80 dBm. This power level should not overload the receiver but leads to the detection of a strong non-existent target placed at a very low distance from the RADAR.

7.3.2 Radiation pattern

Setup

The test setup is given in figure 7.22.

The reference antenna is a Rohde&Schwarz HL025. Its largest dimension is 274 mm. The Fraunhofer distance is then 2.9m at 5.8GHz and 1.45m at 2.9GHz. Due to the limited size of the anechoic chamber, the antenna are placed 3m apart. We see that for 5.8GHz, the Fraunhofer distance is comparable to the distance between the antennas. Therefore, the condition for far-field is barely fulfilled. We can then say that we are not in near-field but not truly in far-field.

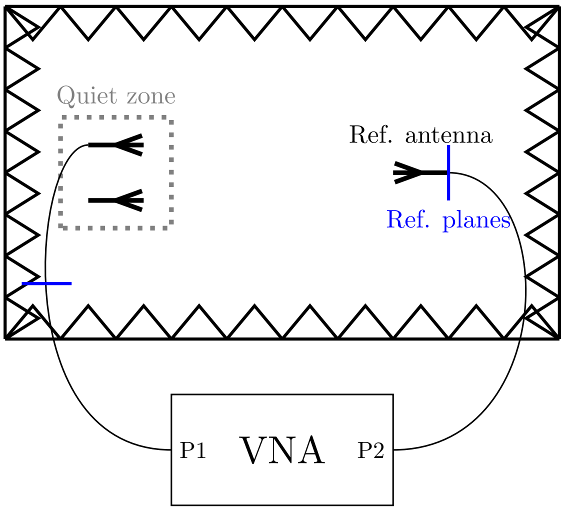

Figure 7.22

Methodology

The measurements we will perform are based on Friis path loss equation. As a remainder, this equation is given in equation 7.2.

$$P_{RX} = P_{TX} G_{TX} G_{RX} \left(\frac{\lambda}{4\pi d} \right)^2 \tag{7.2}$$

Using this equation, we can deduce the gain of an antenna knowing the ratio between the emitted and received power as well, the gain of the other antenna and the distance between the antennas. This equation is applicable only in far-field. Therefore, we must make sure that the antennas are placed in the Fraunhofer region of one another. The limit of this region is given by equation 4.28.

Multiple well-known methods of measurement of the antenna gain based on the Friis formula exist: the two-antenna (reciprocal) method, the three antenna method (gain transfer) and absolute gain measurement.

The two antenna method uses two identical antennas under test (AUTs). Under the assumption that the gain of both antenna is the same, we can compute the gain by taking the square root of the complete system gain ($G_{TX} G_{RX}$) in equation 7.2.

The three antenna method uses a reference and unknown antenna in addition with the AUT. Its principle is as follows: we measure the received power of the reference and AUT using the unknown antenna. Then, by comparing these two measurements (Ratio), we obtain the gain difference between the two measured antenna. Knowing the gain of the reference antenna, we can then obtain the gain of the AUT. This comparative method allows to easily compensate the path loss, gain of the measurement antenna and various test setup non-idealities (reflection, cable losses, etc.) without having to measure them.

The last method, the absolute gain measurement is the most precise method as it is not based on assumptions (e.g. the gain of a reference antenna, the identical gain of the two AUTs). That is why it is used in calibration lab. to characterize reference antennas. It consists in a absolute power measurement in a controlled environment and then extracting the gain from the Friis formula. However, this method requires extremely careful with the methodology and take into account all possible losses and inaccuracy that are bot dependent on the test setup (e.g. cable loss, signal source inaccuracy, inaccuracy).

In this work, as the antenna is not well matched at one port, we will obtain a gain and radiation pattern that are not representative to the antenna when matching circuits are added. Therefore, we will use a simpler measurement method that only require the AUT and a reference antenna. From Friis equation, we notice that if we know the ratio between emitted and received power as well as the gain of the reference antenna, we can estimate the gain of the antenna.

We can then use a VNA which has its reference planes placed at the antennas port to measure the S-parameters. The calibration of the VNA allows to easily remove the cable losses ass well as source and receiver non-idealities. The transmission coefficients (S21 and S12) will represent the ratio between emitted and received power. Therefore, the gain of the AUT can be obtained from these coefficients by subtracting the gain of the reference antenna and the path loss.

In practice, a calibration is performed at the reference planes that are shown in figure 7.22. The cable between the reference plane and the AUT (left) is deembed such that the pair of reference plane is at the ports of both antennas.

The antenna is then rotated using a positioner and the S21 measured to obtain the radiation in all the desired directions.

Finally, the gain of the AUT is obtained by subtracting the path loss (at 3 meters) and the gain based on the reference antennas specifications.

Results

We will now discuss the results from the gain measurements. The radiation pattern and maximum realized gain for the measurements and simulations are shown in figure 7.23. To better match the prototype, the simulation was performed with a model that had only 3 monopoles at each frequencies and using lossy materials instead of perfect electric conductors (PEC). The radiation pattern is shown for 2 planes: the azimuthal plane and the elevation plane. As said in section 3.3, we focus on the azimuthal plane in this work.

First, we take a look at the general shape of the radiation pattern in the two planes. We notice that the radiation at the back of the antenna in the azimuthal plane is lower than expected. This can be explained by the fact that the elevation during the measurement could have been slightly off by some degree. Indeed, from the graph in the elevation plane, we see that the gain rapidly change around -180°. Therefore, for a small change in elevation during the measurement, we observe a large difference in value. We see that a few degree are sufficient to go from a gain of -20 dB to -15 dB which is the difference seen in the azimuthal plane. In any cases, a lower back radiation is in fact better. This difference is therefore not important.

Otherwise, the shape of the main lobe in the azimuthal plane is similar between the measurements and the simulation.

In the elevation plane, the shape of the radiation patterns have roughly the same primary and secondary lobes especially for the harmonic antenna (on the right in the figure).

When we take a look at the values of the gain, we see that the measured one are 1 dB or 2 dB (at 2.9 GHz and 5.8 GHz respectively) below what was expected.

First, at 2.9GHz, we see that, even though the points for which the angle is 0 in both plane is geometrically the same, the gain is not the same for each value (3.13 and 2.16 for the azimuthal and elevation plane respectively). For 5.8 GHz and the simulation, this gain equivalence holds. This indicates that the measurement of the elevation plane at 2.9 GHz may be invalid.

Still, for the three other measurements, we see that a difference of 0.9 dB and 1.6 dB remains. These difference could come from multiple source: inaccuracy in the test setup, incorrect gains of the reference antenna and tolerance of the prototype dimensions (i.e. of the monopole length). First, the test setup inaccuracies can come from the inaccuracy in distance and polarization matching between the AUT and reference antenna as well as possible reflections from the antenna support.

Secondly, the accuracy of the reference gain of antenna directly translate in a variation of measured gain. As the reference gain was visually extracted of a graph from the technical specification of the antenna, it could be quite imprecise. Similarly, if the AUT is not properly aligned with the boresight of the reference antenna, a reduction in measured gain is expected.

Finally, the antenna support can cause additional reflection that can interfere with the radiation pattern. However, as it is made of PLA and is non-metallic, we can suppose that the interferences should not be as significant as the observed difference.

To be conservative in the link budget, we take the measured values of realized gain as they are lower than expected.

7.4 Maximum distance of detection

In this section, we will compute a quick estimation of the maximum detection range of the current prototype. At this end, we will first perform a measurement of the tag conversion efficiency to obtain the last remaining unknown of the link budget.

7.4.1 Tag conversion efficiency

This measurement is based on the methodology explicited in section 4.1.3. We place the tag at a fixed distance in the far field of the antenna. Then, we get multiple values of

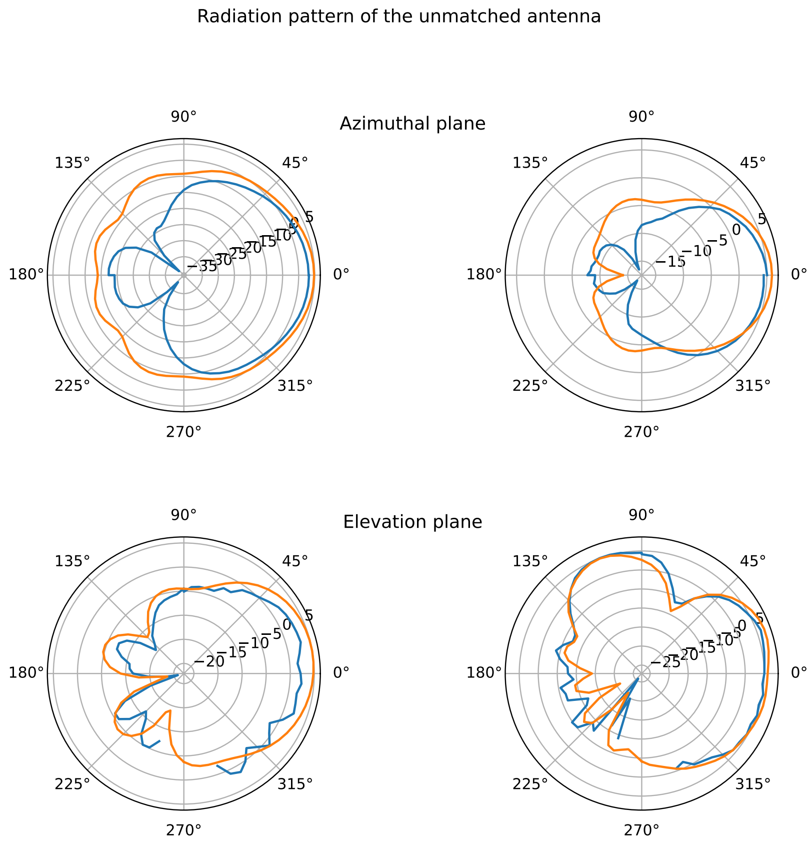

	Max realized gain [dB]				Angle of maximum [°]	
	Azimuth		Elevation		Azimuth	Elevation
	Meas	Sim	Meas	Sim	Meas	Meas
2.9 GHz	3.225	4.818	3.038	4.964	360.00	15.00
5.8 GHz	5.047	5.925	6.116	7.055	0.00	20.00

Figure 7.23: Measurements of the radiation pattern of the antennas in the azimuthal and elevation planes. The fundamental antenna (2.9 GHz) is shown on the left while the harmonic antenna (5.8 GHz) is on the right.

received power for different emitted power. Finally, using the equation, we obtain the tag conversion efficiency.

Setup

The setup used for this measurement is shown in figure 7.24. The cake antenna is placed in an anechoic chamber with its main lobe directly facing the tag.

As we will see in the methodology, we also need to perform a calibration measurement. For this, we simply remove the tag from the anechoic chamber.

The signal is produced by a

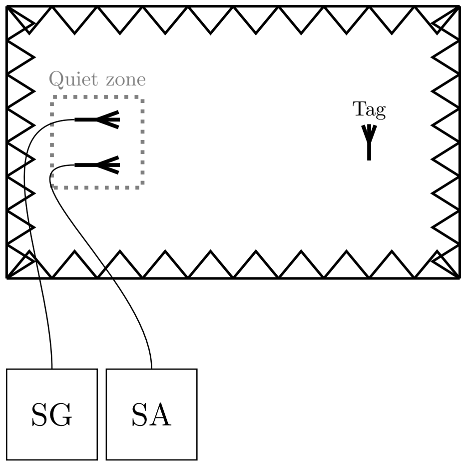

Figure 7.24: Setup for the measurement of the tag efficiency. The signal generator (SG) is connected to the fundamental port and the signal analyzer to the harmonic port.

Methodology

To apply the procedure explained in section 4.1.3. We need to measure the received power depending on the emitted power. To achieve this, we measure the power spectrum around the expected harmonic frequency for multiple SG power values. The received power is then deduced from the maximum of the power spectrum.

As we have seen that some of the received power is coming from the transmitter instead of the tag. Therefore, we first perform a measurement without the tag at every transmitted power value. Then we linearly subtract the resulting powers from the measurements.

Finally, we compensate for the losses of the long cables of the anechoic chamber using their measured S-parameters. For the transmitted power, the cable loss is embedded into the power setting of the signal generator. For the received power, the cable loss is deembed from the SA measurement.

Once the emitted and received power are obtained, we apply equation 4.17. We obtain the conversion loss for the given values of transmitted power. Finally, we apply equation 4.23 on the emitted power to obtain the equivalent conversion loss for a fixed emitted power of 27 dBm (Saturated power of the transmitter).

Results

The resulting tag conversion efficiency (tag CE, $\eta(d)$) is shown in figure 7.25. A smoothing spline was found[11] to extrapolate the measurement.

7.4.2 Operational range

To end this chapter, we obtain the distances for which the condition given in 4.26 is met.

[11] using the scipy python library

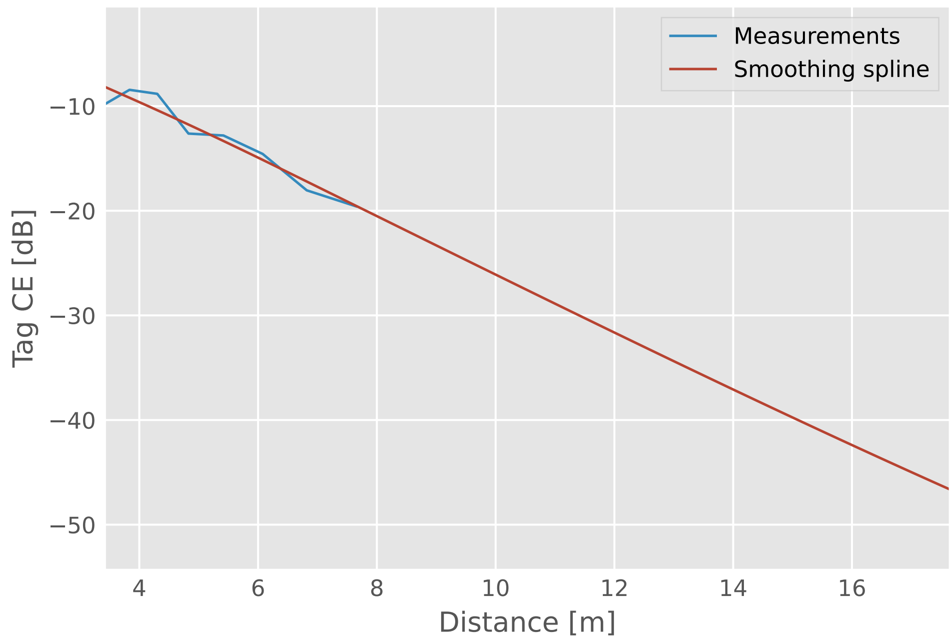

Figure 7.25: Conversion efficiency of the tag depending on the distance between the tag and the RADAR. A smoothing spline found using the generalized cross-validation (GCV) criterion.

We consider a minimum SNR of -10 dB based on the values obtained in 4.1. A higher value of SNR threshold was used to take into account performance degradation due to additional non-idealities (e.g. phase noise). This value correspond to the minimum SNR required at the end of the receiver such that the parameter estimation method is operational.

However, in the link budget, the minimum SNR correspond to the SNR at the output of the receiving antenna. Therefore, we must take into account the NF of the receiver. The minimum SNR is then given by equation 7.3.

$$SNR_{in,min} = SNR_{out,min} + NF \tag{7.3}$$

The noise power at the receiving antenna can be obtained from the system bandwidth and the antenna temperature. In this work, we will simply assume an antenna noise temperature (T_A) is equal to 290K and a system bandwidth of 200MHz. The minimum received power is the following equation.

$$P_{noise} = kT_AB = -121dBm \tag{7.4}$$

$$\Rightarrow P_{RX,min} = P_{noise} + SNR_{in,min} = -131dBm + NF \tag{7.5}$$

Finally, we can obtain the K factor (from equation 4.26) by using the values in table 7.26a. They correspond to the characteristics of the current prototype.

We can also estimate the improvement we can hope by improving the matching of the antennas and by using a better receiver chain configuration. These changes translate

Symbol	Value
P_{TX}	27 [dBm]
P_{noise}	-121 [dBm]
$SNR_{out,min}$	-10 [dB]
NF	7 [dB]
G	6.12 [dBi]
f_f	2.95 [GHz]
d_{max}	8 [m]

(a) Table containing the values used to compute the maximum operational range (d_{max}).

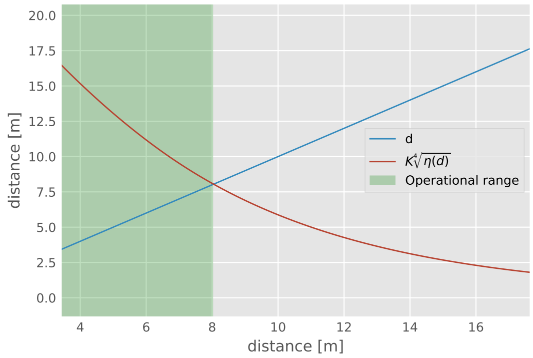

(b) Plot of the operational condition (see eq. 4.26.) of the RADAR.

Figure 7.26: Operational range results for the current prototype.

into a greater total gain (G) and a smaller receiver noise figure (NF). Note that the conversion efficiency of the tag in function of distance is also impacted. Indeed, a higher gain at the fundamental antenna results in a greater input power of the tag ($\bar{P}_{RX}$). As the CE decrease with this power (decrease for a longer distance in figure 7.25), the results obtained using the previously computed CE are conservative.

The new results are given in figure 7.27. We observe an increase of 1.45 m which correspond to an improvement of 18% of the RADAR range. The maximum range is then 9.45 m.

Symbol	Value
P_{TX}	27 [dBm]
P_{noise}	-121 [dBm]
$SNR_{out,min}$	-10 [dB]
NF	2.78 [dB]
G	12.25 [dBi]
f_f	2.95 [GHz]
d_{max}	9.46 [m]

(a) Table containing the values used to compute the maximum operational range (d_{max}).

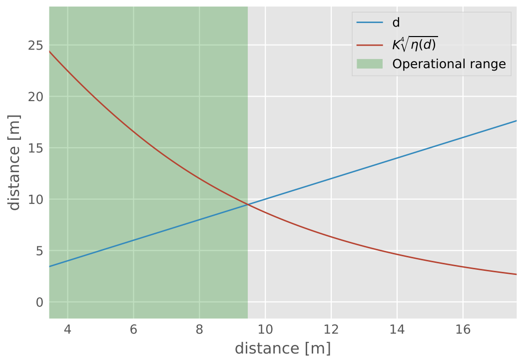

(b) Plot of the operational condition (see eq. 4.26.) of the RADAR.

Figure 7.27: Expected operational range results for the improved prototype.

The obtained values are quite low as expected (due to harmonic conversion losses). Nevertheless, it could be sufficient in our application if the hornet behavior is not modified by the proximity of the UAV.

Chapter 8

Conclusion

In this work, we have designed a prototype of harmonic RADAR with a maximum range of 8m.

We have first discussed the strength of this technology compared to other tracking alternative. Then, we have selected a specific implementation by choosing the drone position relative to the target. Next, we have developed the link budget and RADAR equation to determine the design priorities in term of prototype characteristics. For the RF circuit, we designed the transmitter for a high output power and the receiver for a low noise figure. For the antenna, the sum of the two gains in dB was maximized while the dimensions were kept small to reduce the manufacturing complexity.

Finally, we characterized the complete system and obtained its performances. We have seen that its performances can be easily improved by improving the impedance matching of the antenna or using a LNA with a higher gain.

The maximum range of the prototype is small (8m). Nevertheless, this short range can still be sufficient to test different tracking concepts such as angle scanning with the switched antenna array and true delay line. One could also try to track a tagged drone in the vicinity of the RADAR to determine the needed resolution of the parameters estimator.

However, for the real application, this range is certainly insufficient. We then need to increase it. We have seen that we can lengthen the range by 20% only adding matching filters for the antennas and changing the LNA. To further increase the range, we have to act on the emitted power, antenna gains or improve the tag conversion efficiency as all other quantities are fixed (path loss) or require high efforts to improve (receiver NF, minimum SNR of the parameter estimator).

Bibliography

[1] Theagenis J. Abatzoglou. “Fast Maximum Likelihood Joint Estimation of Frequency and Frequency Rate”. In: *IEEE Transactions on Aerospace and Electronic Systems* AES-22.6 (1986), pp. 708–715. DOI: 10.1109/TAES.1986.310805.

[2] Morgane Barbet-Massin, Jean-Michel Salles, and Franck Courchamp. “The economic cost of control of the invasive yellow-legged Asian hornet”. In: *NeoBiota* 55 (2020), pp. 11–25.

[3] Morgane Barbet-Massin et al. “Climate change increases the risk of invasion by the Yellow-legged hornet”. In: *Biological Conservation* 157 (2013), pp. 4–10.

[4] Boualem Boashash. “Estimating and interpreting the instantaneous frequency of a signal. II. Algorithms and applications”. In: *Proceedings of the IEEE* 80.4 (2002), pp. 540–568.

[5] Analog Devices. *ADL5324*. https://www.analog.com/media/en/technical-documentation/data-sheets/ADL5324.pdf. Version Rev. B. [Online; accessed 4-January-2026].

[6] Petar M Djuric and Steven M Kay. “Parameter estimation of chirp signals”. In: *IEEE Transactions on Acoustics, Speech, and Signal Processing* 38.12 (1990), pp. 2118–2126.

[7] EASIN. *European Alien Species Information Network - Species Explorer - Dynamic Maps*. https://easin.jrc.ec.europa.eu/spexplorer/dynmap/. accessed 05-04-2025.

[8] Ettore Fedele et al. “Invasive alien species impact on ecosystem services”. In: *Publications Office of the European Union: Luxembourg* (2019).

[9] Richard M. J. Hassall et al. “Predicting the spatio-temporal dynamics of biological invasions: Have rapid responses in Europe limited the spread of the yellow-legged hornet (Vespa velutina nigrithorax)?” In: *Journal of Applied Ecology* 62.1 (2025), pp. 106–118. DOI: https://doi.org/10.1111/1365-2664.14829. URL: https://besjournals.onlinelibrary.wiley.com/doi/abs/10.1111/1365-2664.14829.

[10] Cayetano Herrera et al. “Automated detection of the yellow-legged hornet (Vespa velutina) using an optical sensor with machine learning”. In: *Pest Management Science* 79.3 (2023), pp. 1225–1233.

[11] Intuite. *LOCNEST*. https://www.intuite.fr/en_GB. [Online; accessed 4-January-2026].

[12] Sumit Karki et al. “Sequentially shifted beamforming from a conformed conical array”. In: *2017 European Radar Conference (EURAD)*. IEEE. 2017, pp. 367–369.

[13] Keysight. *N5183B X-series Signal Generators*. https://www.keysight.com/zz/en/assets/7018-04096/data-sheets/5991-3131.pdf. [Online; accessed 4-January-2026].

[14] Bong-Seok Kim et al. "FMCW radar estimation algorithm with high resolution and low complexity based on reduced search area". In: *Sensors* 22.3 (2022), p. 1202.

[15] SEUNGWON KIM et al. "A Tracking Method for the Invasive Asian Hornet: A Brief Review and Experiments". In: *IEEE Access* 7 (2019), pp. 176998–177008.

[16] Niyonzima Laetitia and Craeye Christophe. "Smart Hat Antenna For Wifi Applications". In: *2022 International Conference on Electromagnetics in Advanced Applications (ICEAA)*. IEEE. 2022, pp. 178–181.

[17] Simone Lioy et al. "Tracking the invasive hornet Vespa velutina in complex environments by means of a harmonic radar". In: *Scientific reports* 11.1 (2021), p. 12143.

[18] Simone Lioy et al. "Viability of thermal imaging in detecting nests of the invasive hornet Vespa velutina". In: *Insect Science* 28.1 (2021), pp. 271–277.

[19] Riccardo Maggiora et al. "An innovative harmonic radar to track flying insects: The case of Vespa velutina". In: *Scientific reports* 9.1 (2019), p. 11964.

[20] Minicircuits. *CMA-545+*. https://www.minicircuits.com/pdfs/CMA-545+.pdf. Version Rev. E. [Online; accessed 4-January-2026].

[21] Minicircuits. *GP2X+*. https://www.minicircuits.com/pdfs/GP2X+.pdf. Version Rev. F. [Online; accessed 4-January-2026].

[22] Minicircuits. *KSX2-14+*. https://www.minicircuits.com/pdfs/KSX2-14+.pdf. Version Rev. C. [Online; accessed 4-January-2026].

[23] Minicircuits. *MCA1-85+*. https://www.minicircuits.com/pdfs/MCA1-85L+.pdf. Version Rev. D. [Online; accessed 4-January-2026].

[24] Minicircuits. *ROS-3800-119R+*. https://www.minicircuits.com/pdfs/ROS-3800-119R+.pdf. Version Rev. OR. [Online; accessed 4-January-2026].

[25] Jeonghyeon Pak et al. "Unmanned Aerial Vehicle-based Autonomous Tracking System for Invasive Flying Insects". In: *Computers and Electronics in Agriculture* 227 (2024), p. 109616.

[26] Belal Al-Qudsi et al. "Zoom FFT for precise spectrum calculation in FMCW radar using FPGA". In: *Proceedings of the 2013 9th Conference on Ph. D. Research in Microelectronics and Electronics (PRIME)*. IEEE. 2013, pp. 337–340.

[27] Fabrice Requier et al. "Economic costs of the invasive Yellow-legged hornet on honey bees". In: *Science of the Total Environment* 898 (2023), p. 165576.

[28] Supratim Saha and Steven M Kay. "Maximum likelihood parameter estimation of superimposed chirps using Monte Carlo importance sampling". In: *IEEE Transactions on Signal Processing* 50.2 (2002), pp. 224–230.

[29] Kashif Siddiq et al. "Phase Noise in FMCW Radar Systems". In: *IEEE Transactions on Aerospace and Electronic Systems* 55.1 (2019), pp. 70–81. DOI: 10.1109/TAES.2018.2847999.

[30] Michael Thomas Smith, Michael Livingstone, and Richard Comont. "A method for low-cost, low-impact insect tracking using retroreflective tags". In: *Methods in Ecology and Evolution* 12.11 (2021), pp. 2184–2195.

[31] Greg Storz and Anastasia Lavrenko. "Compact Low-cost FMCW Harmonic Radar for Short Range Insect Tracking". In: *2020 IEEE International Radar Conference (RADAR)*. IEEE. 2020, pp. 642–647.

[32] Thomas Walter et al. "A new innovative real-time tracking method for flying insects applicable under natural conditions". In: *BMC zoology* 6.1 (2021), p. 35.

[33] Chengzhi Wang et al. "A Review of Five Existing Hornet-Tracking Methods". In: *Insects* 15.8 (2024), p. 601.

[34] Quantic X-Microwave. *Overview*. `https://quanticxmw.com/company-overview/`. [Online; accessed 23-February-2025].

[35] Pei-Hao Ye. "Tracking Asian hornets with low-power harmonic radars : applicative constraints and tag design". MA thesis. Ecole polytechnique de Louvain, Université catholique de Louvain, 2024. URL: `http://hdl.handle.net/2078.1/thesis:48918`.

Appendices

Appendix A

Sweep of the large antenna dimensions

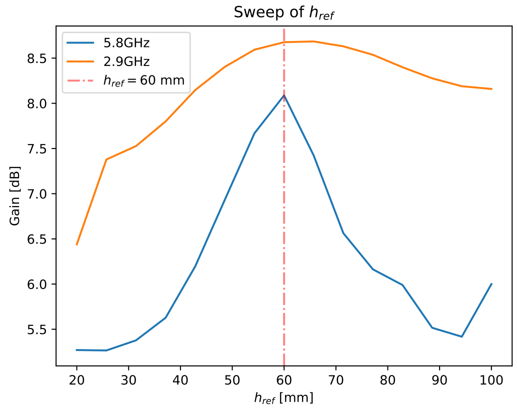

Figure A.1: Sweep of h_{ref}

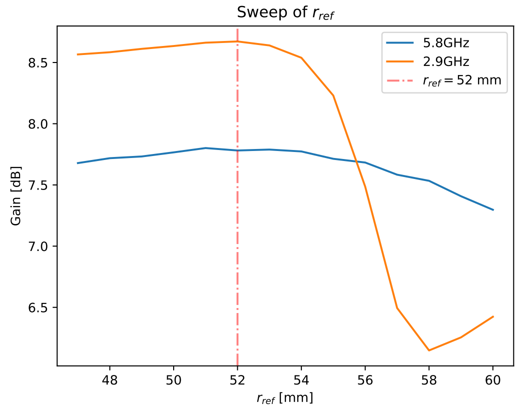

Figure A.2: Sweep of r_{ref}

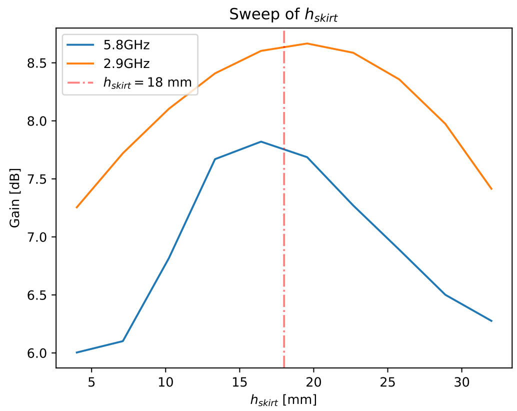

Figure A.3: Sweep of h_{skirt}

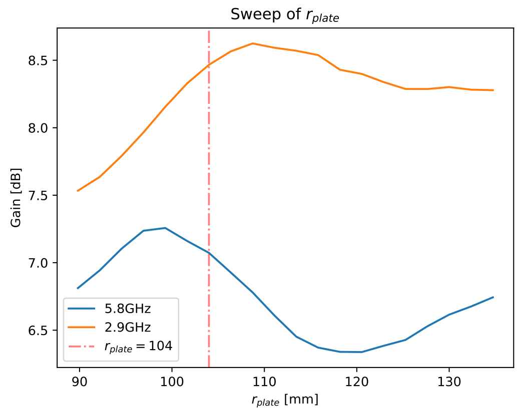

Figure A.4: Sweep of r_{plate}

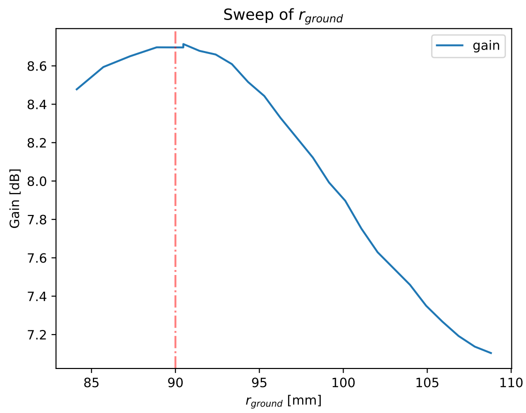

Figure A.5: Sweep of r_{ground}

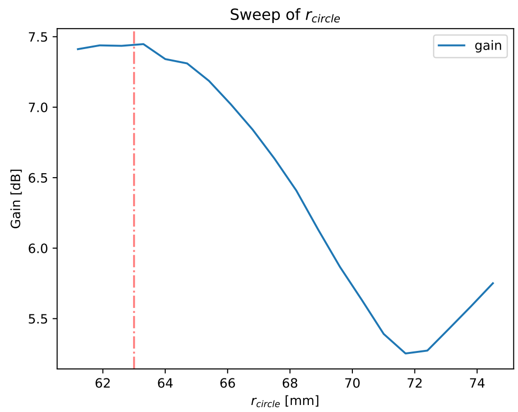

Figure A.6: Sweep of r_{circle}

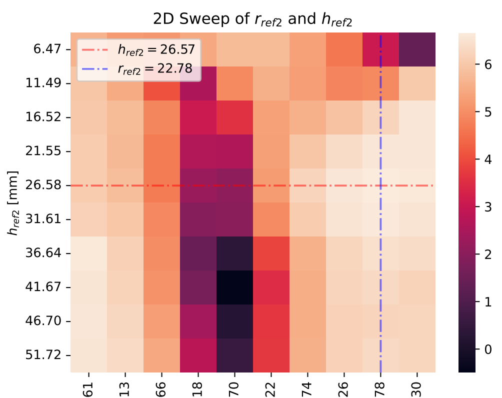

Appendix B

Technical drawing of the 2 version of the cake antenna

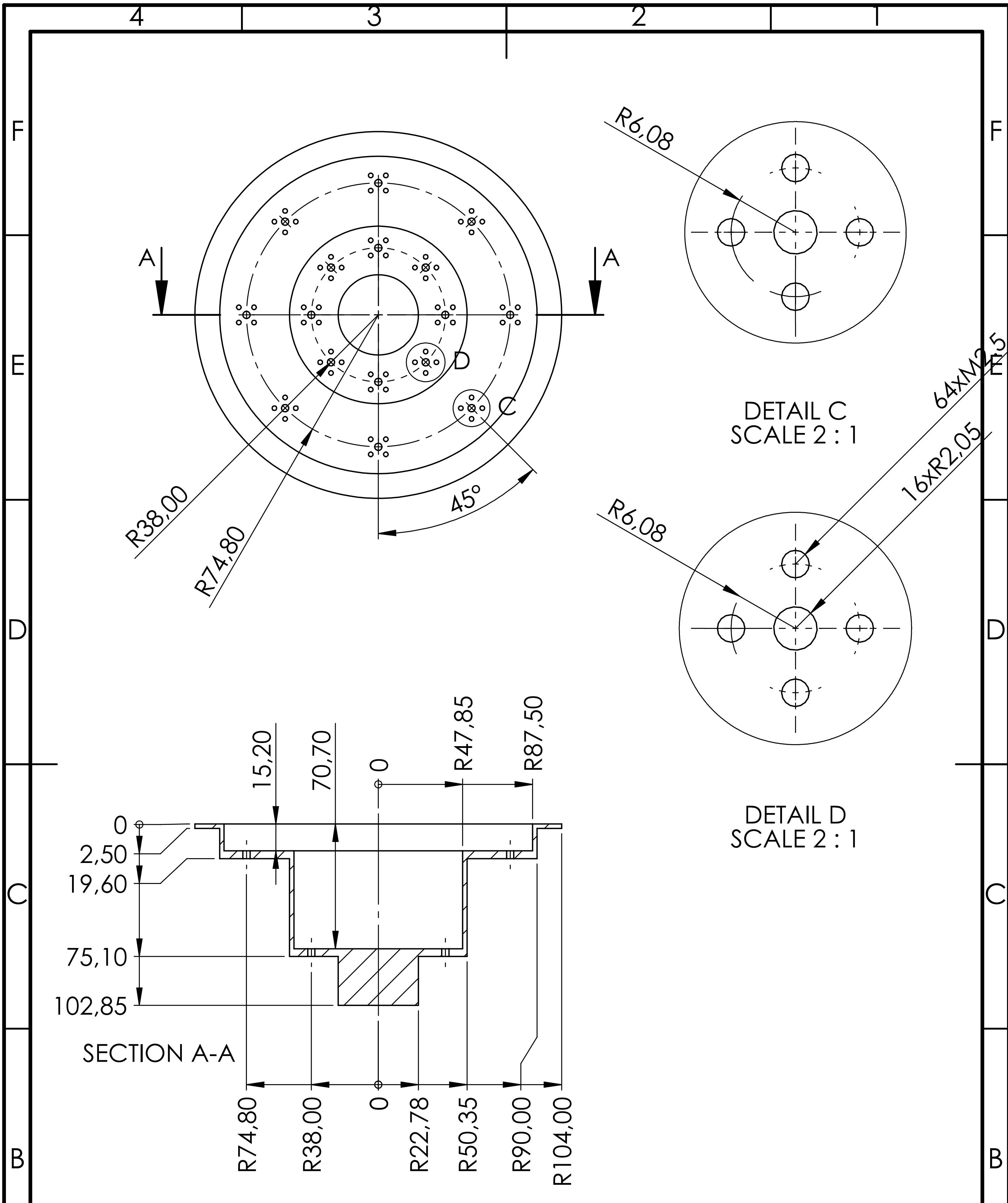

SAUF INDICATION CONTRAIRE: LES COTES SONT EN MILLIMETRES ETAT DE SURFACE: TOLERANCES: LINEAIRES: ANGULAIRES:	FINITION:	CASSER LES ANGLES VIFS	NE PAS CHANGER L'ECHELLE / REVISION

	NOM	SIGNATURE	DATE
AUTEUR	Hugo Damme		25-03-25
VERIF.			
APPR.			
FAB.			
QUAL.			

TITRE:

Cake antenna

MATERIAU: Aluminium

No. DE PLAN: CakeAntennaV1

A4

MASSE:

ECHELLE:1:3

FEUILLE 1 SUR 1

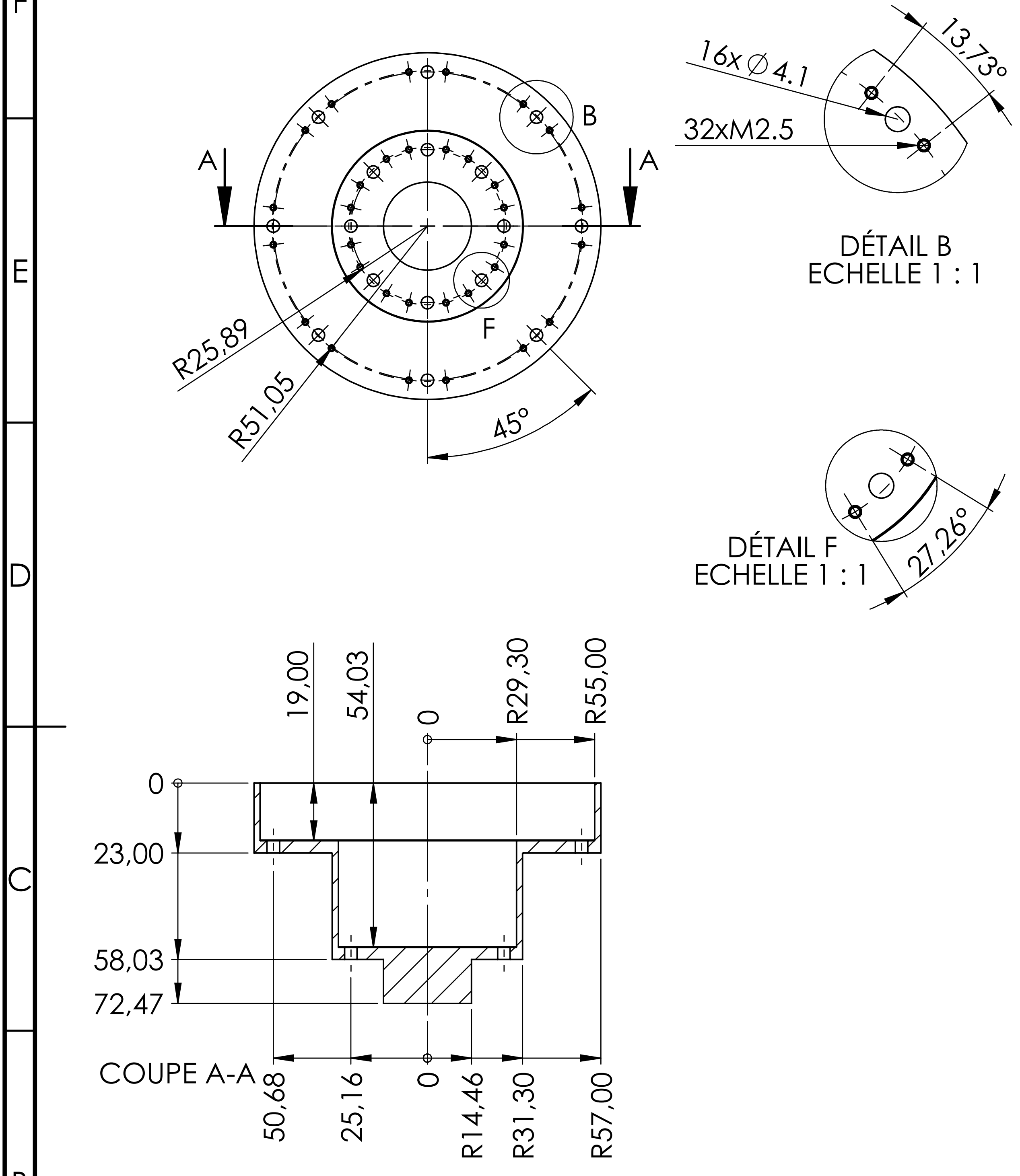

SAUF INDICATION CONTRAIRE: LES COTES SONT EN MILLIMETRES ETAT DE SURFACE: TOLERANCES: LINEAIRES: ANGULAIRES:	FINITION:	CASSER LES ANGLES VIFS	NE PAS CHANGER L'ECHELLE	REVISION

	NOM	SIGNATURE	DATE
AUTEUR	Hugo Damme		25-03-25
VERIF.			
APPR.			
FAB.			
QUAL.			

TITRE:

Cake antenna

MATERIAU: Aluminium

No. DE PLAN: CakeAntennaV2

A4

MASSE:

ECHELLE:1:2

FEUILLE 1 SUR 1

UNIVERSITÉ CATHOLIQUE DE LOUVAIN
École polytechnique de Louvain
Rue Archimède, 1 bte L6.11.01, 1348 Louvain-la-Neuve, Belgique | **www.uclouvain.be/epl**